Control of Cell-Material Interactions in 2D and 3D Systems

Submitted in partial fulfillment of the requirements for

the degree of

Doctor in Philosophy

in

Mechanical Engineering

Stephen A. Coyle

B.S., Applied Mathematics, Claflin University
M.S., Mechanical Engineering, Carnegie Mellon University

Carnegie Mellon University
Pittsburgh, PA

April 2022

To my parents,
Daniel and Ingrid Coyle,
and sisters,
Michelle and Emily Coyle

Acknowledgements

It would be an understatement to say that the completion of a PhD takes a great deal of time and energy . While difficult at times, I would not trade these last several years at Carnegie Mellon for anything. I have grown a lot since starting my time here. My experiences have helped me become a better academic, researcher, friend, and overall human being. This is especially so due to my advisors and the friends I have met along the way.

First and foremost, would like to thank my co-advisors and thesis committee members Dr. Jimmy Hsia, Dr. Philip LeDuc, and Dr. David Quinn. I have said this in the past many times, and I would like to say here officially, I lucked out in having you all as advisors. I would like to thank you all for being very approachable and so encouraging. After every meeting I always felt I was receiving the proper guidance to tackle every new challenge that came up throughout my research. For this and much more, I am grateful.

I would like to thank the members of Dr. Hsia's lab: Dr. Changjin Huang, Dr. Lakshmi Ramasubramanian, Dr. Arif Abdulla, Mike Grigola, and Gubeum Kwon. In particular, I am grateful my thesis committee member, Changjin, who helped me so much when I first joined the lab in 2016. You were a great mentor, and I am thankful for the knowledge you shared with me. You are one of the many reasons I have made it this far as a researcher. I would also like to thank members of the LeDuc lab: Dr. Kyle Justus, Dr. Ardon Shorr, Dr. Adam Wood, Dr. Rudy Torres, Dr. Justin Bobo, Dr. Dan Clymer, Dr. Wei Chen, Dr. Jonelle Yu, Dr. Li Wan, Dr. Jennifer Bone, Dr. Utku

Sonmez, Akash Garg, Andres Garcia, Ernest Kabuye, Susana Beltran, Andres Rosales, Nolen Frey, Mark DeAngelis and Nolen Keys, for their support.

I would like to the thank Dr. Carmel Majidi and Dr. Philip Won. Dr. Majidi, it was a pleasure to write our minireview on soft robotics in my first year at Carnegie Mellon. Furthermore, the time working with your post doc Philip has been terrific. I could not have asked for someone better to collaborate with.

My parents, Ingrid and Dan Coyle, have always encouraged and supported me in all of my aspirations. They taught me to have an inquisitive mind and the value of a good education. This is in part why I wanted to pursue a PhD. I would like to thank my grandparents for teaching many of the principles I live by today. I appreciate my siblings, Emily and Michelle Coyle, for being so much fun and giving me such a happy childhood. Also, I would like to thank Robert Henderson, for his help for me and my family in getting scholarships to fully pay for undergraduate education. I thank the rest of my family for their love and support. I would not be who I am or where I am today without my family.

Abstract

Animals exploit the deformability of soft structures to move efficiently in complex natural environments. These soft structures are inherently compliant and enable large strains in

components not typically found in robotics. Such capabilities have inspired robotic engineers to incorporate soft technologies into their designs. One goal in soft robotics is to endow robots with new, bioinspired features that permit morphologically adaptive interactions with unpredictable environments. There are three key elements of bioinspired soft robots from a mechanics vantage point, namely, materials selection, actuation, and design. Soft materials are necessary for safe interaction and overall actuation of bio-inspired soft robots. The intrinsic properties of materials in soft robots allow for an "embodied intelligence" that can potentially reduce the mechanical and algorithmic complexity in ways not possible with rigid-bodied robots. Finally, soft robotics can be combined with tissue engineering and synthetic biology to create biohybrid systems with unique sensing, dynamic response, and mobility. Bioinspired soft robots have the ability to also expedite the evolution of co-robots that can safely interact with humans. This thesis revolves around understanding of the structure-property relations in 2D and 3D soft components that aid in the design objectives of biohybrid systems.

The propensity of cells to align in particular directions is relevant to a number of areas, including tissue engineering and biohybrid soft robotics. Cell alignment is modulated through various extracellular conditions including surface topographies, mechanical cues from cell-matrix interactions, and cell-cell interactions. Understanding of these conditions provides guidance for desirable cellular structure constructions. In chapter 2, we examine the roles of surface topographies and cell-cell interactions in inducing cell alignment. We employed wavy surface topographies at the nanometer scale as a model extracellular environment for cell culture. The results show that, within a certain range of wavelengths and amplitudes of the surface topographies, cell alignment is dependent on cell confluency. This dependence on both topology

and confluency suggests interplay between cell-cell and cell-matrix interactions in inducing cell alignment. Images of sparsely distributed and confluent cells also demonstrated clear differences in the structures of their focal adhesion complexes. To understand this effect, we introduced anti-N-cadherin to cell culture to inhibit cell-cell interactions. The results show that, when anti-N-cadherin was applied, cells on wavy surfaces required greater confluency to achieve the same alignment compared to that in the absence of anti-N-cadherin. The understanding of the cell alignment mechanisms will be important in numerous potential applications such as scaffold design, tissue repair, and development of biohybrid robotic systems.

Muscle cell-based biohybrid actuators have generated much interest for the future of soft robotics for their mimicry of living muscle performances. Unfortunately, current biohybrid actuators move without having much control over their actuation behavior. Integration of microelectrodes into the backbone of these systems may enable modulated control over these actuators with specific activation patterns. In chapter 3, we address biocompatibility challenges in incorporating eutectic gallium-indium (EGaIn) microelectrodes into biocompatible constructs for cell stimulation. Although EGaIn has advantageous conductive and rheological properties as a microelectrode, studies show that the material is cytotoxic when in direct contact with cells and currently there are few methods for the material to viably interface with the cell culture. The goal of this chapter is to improve EGaIn biocompatibility by embedding the liquid metal into biocompatible elastomers. Such advancements in EGaIn biocompatibility will allow for applications that improve the controllability of bio-hybrid robots and expedite the evolution of soft robots that can safely interact with humans and natural complex environments.

One of the most critical challenges in the fabrication of thick, 3D tissue is vascularization. Without vascularization, engineered tissue lacks oxygen and access to nutrients, which prompts cells to undergo cell death through apoptosis. In vivo, vasculogenesis and healthy maintenance of the structure and morphology of each blood vessel is mediated via competing mechanical, chemical, and physiological factors. In chapter 4, we propose a novel vascular wall model of endothelial cells cultured onto smooth muscle cells utilizing cell sheet stacking techniques for modular control of tissue thickness, cell orientation, and mechanical stimuli. Modular control of these variables is a convenient method to isolate how each stimulus promotes self-organization of the endothelial-vascular smooth muscle cell co-culture. Such advancements in understanding endothelial-vascular smooth muscle cell co-culture will inform the mechanics that stimulate well organized vascularization in engineered tissue.

Table of Contents

List of Tables

List of Figures

List of Abbreviations

PDMS	Polydimethylsiloxane
LMEE	Liquid Metal Embedded Elastomers
EGaIn	Eutectic Gallium-Indium
ECM	Extra Cellular Matrix
LM	Liquid Metal
PU NF	Polyurethane Nanofibers
NIPAAm	N-isopropylacrylamide
PIPAAm	Poly(N-isopropylacrylamide)
PIPAAm-co-AM	Poly(N-isopropylacrylamide)-co-acrylamide
VSMC	Vascular Smooth Muscle Cells
FN	Fibronectin

Chapter 1 : Introduction

Bio-inspired soft robots have the potential to match or even exceed the extraordinary versatility and multifunctionality of natural organisms. To achieve this, the design of bio-inspired robots requires tight integration of sensing, passive mechanics, active movement, and control. These abilities can be accomplished through clever integration of soft, rigid, and biological materials into structures that exhibit global compliance and deformability. Progress depends not only on the development of new multifunctional materials, but also advancements in 3D manufacturing, robust materials interfacing, and novel systems-level design. The focus of this thesis is the structure-property relations of soft components that aid in the design objectives of biohybrid systems.

While soft robotic advances have been making great strides over the past decade, an area of increasing attention is in soft bio-inspired robotics, which present new opportunities to produce engineered components, devices, and machines that can bridge the gap between conventional robots and natural organisms [1, 2, 3]. These new tools could enable seamless interactions between human and robots, and between robots and the natural world.

Many challenges exist in developing soft bio-inspired robots, including materials, design, and system integration. Although some of the engineering principles guiding the development of soft bio-inspired robots are known, new issues can emerge. To produce versatile functionalities of such robots, two objectives should be achieved: i) replacing modular systems (separate hardware for motor, controller, sensors, etc.) with fully integrated materials architectures that merges these functionalities; and ii) replacing hard and piecewise rigid mechanisms with soft matter (e.g., elastomer, gels, fluids, biomatter) that is in physical contact with other objects.

Conventional approaches to address these challenges are not applicable due to soft materials' unique mechanical properties. In contrast to hard bodied robots, soft robots are composed of easily deformable matter such as gels, elastomers, and biological materials that have similar elastic and rheological properties to soft matter found in nature [4, 5]. Thus, soft matter engineers require new algorithms to leverage the unique mechanics of these soft components for commercial applications. In this chapter, we provide a brief review of ongoing efforts to address these challenges in the emerging domain of bio-inspired soft robotics. We begin with an overview of materials typically used to engineer soft robots followed by a discussion of the various approaches for actuation. Next, we review several systems-level implementations.

Bio-Inspired Material Selection

To adapt the mechanical versatility and multifunctionality intrinsic to natural organisms, elastic and viscoelastic properties are essential considerations for the material selection of soft components. A number of issues involving the selection of soft materials for soft systems have been raised in other reviews as well [6, 7]. In this section, useful criteria for materials selection are introduced such as storage and loss modulus as well as work energy density.

Soft components typically used in soft robots include silicone elastomers, urethanes, hydrogels, and nanofibers [8]. Elastomers are especially popular since they allow for the utilization of a broad range of desired elastic and viscoelastic properties within the materials architecture of soft robotic devices. Also, these compliant materials also are advantageous when considering the safety of interaction with biological organisms and the overall actuation of soft robots.

Many useful traits of soft robots are due to the low stiffness of the materials used to construct them. Conventionally, robotic materials (e.g., metals or hard plastics) have an elastic modulus of 10^9 - 10^{12} Pa (N/m^2), whereas most materials in natural organisms (e.g., Cartilage, skin, or muscle tissue) have a moduli of 10^2 - 10^9 Pa [4]. Soft robots can accommodate this elastic property mismatch through mechano-compatibility, by primarily being composed of materials with elastic moduli within the range of biological materials. Typical materials in natural organisms and soft robots tend to deform elastically when a force is applied. Greater compliance allows for a load to be distributed over a larger area, which increases contact time and lowers maximum impact stresses. For instance, due to the conformal nature of soft robots, they can carry or manipulate soft or fragile payloads without causing damage. Popular silicone elastomers that meet the desired compliance matching traits for soft robotic devices include Sylgard 184 and 527 from Dow Chemicals as well as Smooth-Sil 950 and EcoFlex 00-30 from Smooth-On [9]. Soft matter engineering utilizes such materials to minimize interfacial stress concentrators between the user and the soft robotic device.
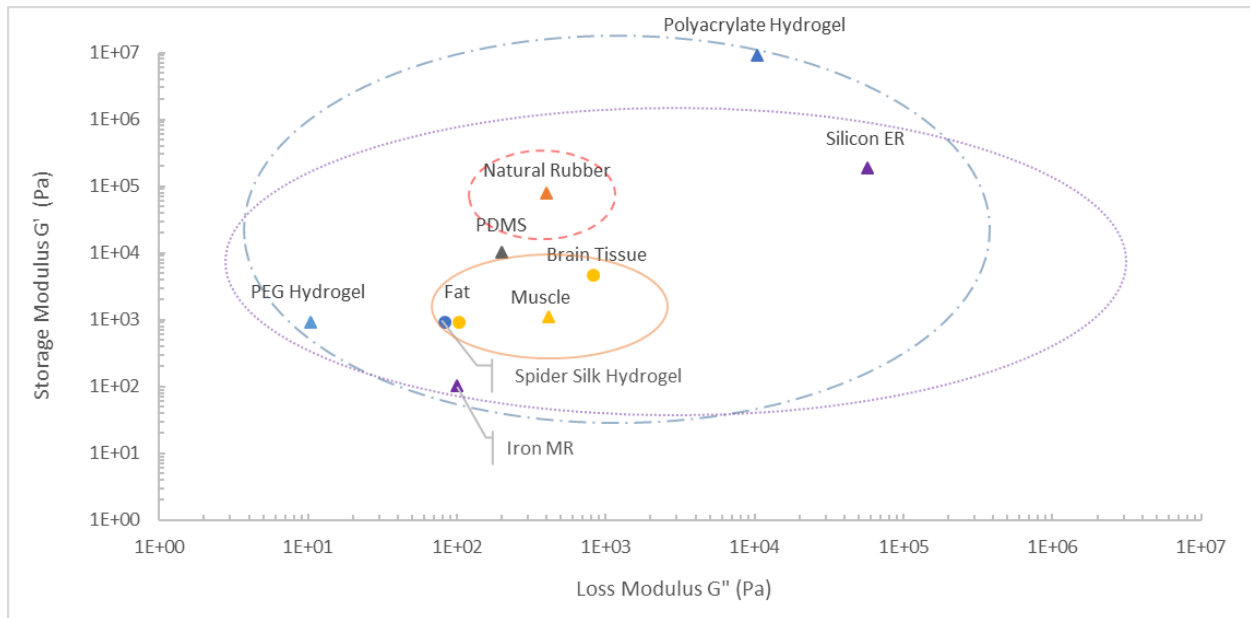
Figure 1.1 Approximation of Storage Modulus vs Loss Modulus of various organic and inorganic materials. Hydrogels: _.._ *; Biological Tissue:* ___ *; Natural Rubber:* ___*; Electrorheological (ER) And Magnetorheological (MR) Fluid Based Polymers:* .... *; Materials that have been used in soft robots: Triangle*

It is important to note that many "soft" materials found in both biology and soft robotics are viscoelastic. The time-dependent viscoelastic properties in biological and soft robotic materials can best be described in terms of their storage and loss moduli, which represent the elastic portion and the viscous portion, respectively (Figure 1.1). Purely elastic materials (e.g., steel, wood, bone) do not dissipate energy when a load is applied and therefore exhibit virtually no loss modulus (which scales with the ratio of loss modulus to storage modulus). In contrast, viscoelastic materials (e.g., muscle, fat, polydimethylsiloxane (PDMS), polyethylene glycol (PEG) Hydrogels, etc.), exhibit both viscous and elastic properties. The inclusion of viscoelastic materials allows for the potential of soft robotic components to dissipate energy and maintain stable motion during dynamical loading. Figure 1 shows the approximate ranges of storage and loss moduli of several classes of materials, including man-made and natural materials. Figure 1 depicts

which materials are good candidates for various applications for achieving compatibility between different materials in a hybrid system.

When selecting materials for a novel soft robot design, it is important to identify optimal viscoelastic material features. Common viscoelastic materials that exhibit elastic hysteresis in soft robotics are urethanes and polyacrylates [10]. Soft polyacrylates like 3M VHB tape are especially popular for dielectric elastomer films, due to their ability to achieve large strains and high electrical field when stretched [11]. Less viscous elastomers like silicone are popular for applications that involve high cycle loading or require high elastic resilience [12]. Another important property of soft, stretchable materials is fracture toughness. Typically, elastic strain limit is sensitive to any features that cause inhomogeneous deformation (e.g., notches, cracks, and other stress concentrators) [13]. Materials that exhibit high fracture toughness include ultra-tough double network hydrogels that utilize ionically and covalently crosslinked networks to dramatically increase their fracture energies [14]. Integration of these material characteristics aid in the desired actuation capabilities of the robot.

An increasingly important metric that allows for comparison of actuators and materials that meet your design objective is the work energy density. Work energy density, relates the compliance of materials with energy density, by representing the upper bound of elastic energy stored by elastic deformation which are the two pillars of actuated soft system. Work energy density gives an approximation of volume needed of a given actuator technology to accomplish a given amount of work. The higher the energy density of the actuator the less volume needed to meet your design objective. Figure 1.2 highlights the tradeoffs between stiffness with the energy density of materials and actuators. Of these actuators the materials used can vastly its

change work energy density. Usually, stiffer materials have higher energy densities, but are less compliant. Silicone based DEAs have a Young's modulus of 0.1-1.0 MPa and a typical work energy density of 10 KJ·m^{-3} [7]. While Acrylic VHB based DEAs have a Young's modulus of 1.0-3.0 MPa and a typical work energy density of 150 KJ·m^{-3} [7]. For biohybrid actuators, with such a difference in performance characteristics, the most appropriate material be considered for a given mechanical task or design objective.
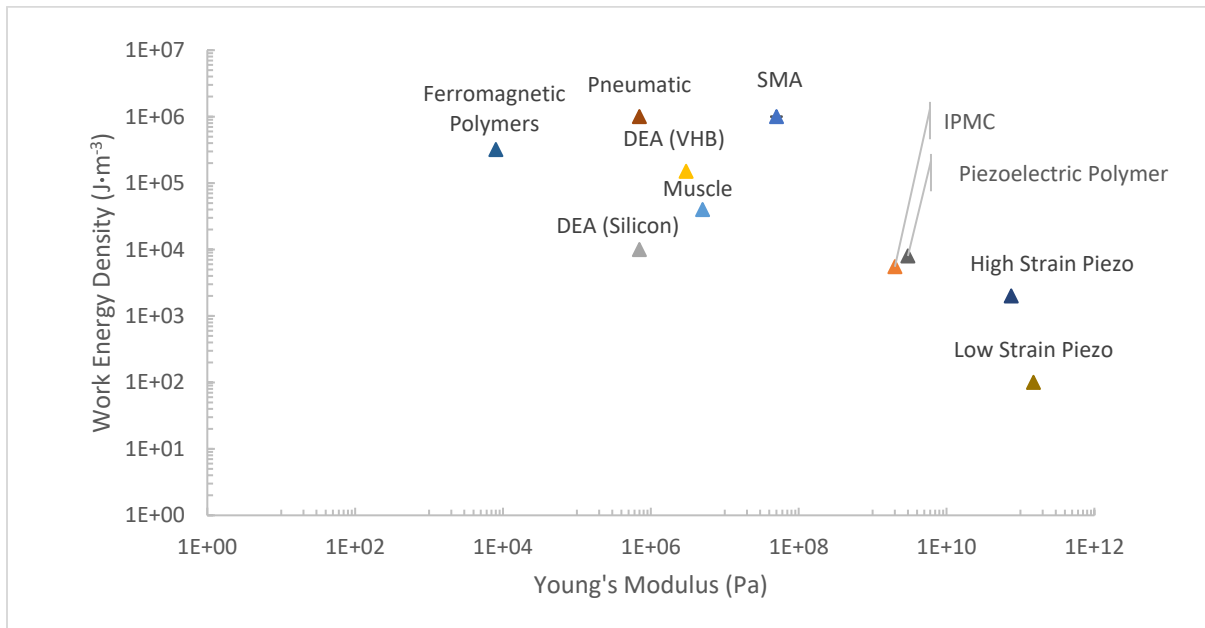
Figure 1.2 Work Energy Density vs Young's Modulus of established soft robotic actuator technologies [7, 15, 16]. Abbreviations: SMA- shape memory alloy, IPMC- ionic polymer-metal composite, DEA- dielectric elastomer

Bio-Inspired Actuation

Conventional robots and soft robots use different mechanisms to achieve actuation. Conventional robots usually have motorized or cable-driven joints that can undergo rotational or translational motions, allowing for finite degrees of freedom for each rigid component. Soft robots have distributed deformations over their soft components allowing for theoretically infinite degrees of freedom [4]. Thus, where rigid robots utilize a motor for every joint, soft

robotic actuation is integrated throughout the entirety of the structure. There are several different control methods for soft robotic actuation that utilize these material properties. This includes pneumatics [17, 18, 19], electrical actuation [20, 21], and chemical stimulation [22, 23]. Generally, the actuation of conventional robots is more precise, but soft robotic actuation is more flexible. In this section, we will cover key working principles of soft robotic actuation.

Variable Stiffness

Much like in nature, soft robotic technologies have an intrinsic coupling between stiffness and contraction [24]. For example, muscles exhibit variations in stiffness between their passive (low stiffness) and active (high stiffness) states [25]. Likewise, soft robots utilize similar techniques to apply forces and modulate their load capacity. For example, particle jamming is a technology that allows for variable stiffness of soft robots. Such robotic manipulators can conform to a wide range of 3D shapes and then lock their shape to support a large payload [26]. The onset of rigidity allows for a variable compliance transmission that is useful for gripping [27], bending [26], and locomotion [28].
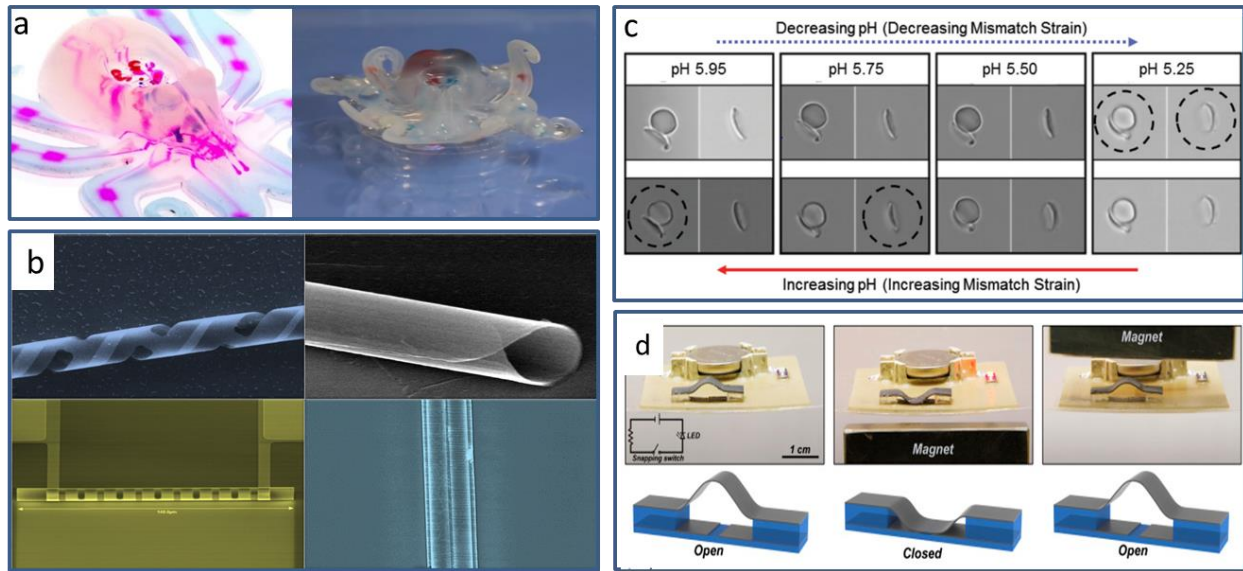
Figure 1.3 Soft matter actuation approaches. (a) A pneumatically actuated entirely soft, autonomous robot, inspired by the continuum nature of the octopus, called the 'Octobot' [23], (b) Hierarchical 3D curvilinear structures induced by mismatch straining [29, 30], (c) A pH-responsive colloidal particle that rapidly changes shape between two bi-stable geometries [22], (d) A pre-buckled ferroelastomer strip serves as a circuit breaker by exploiting snap-through mechanics in response to a magnetic field [31].

Mismatch Strain

Strain-mismatch is a central principle in the operation of unimorph actuators [32]. Reviews exist

of popular actuation technologies exploiting mismatch strain-induced deformation include

dielectric elastomers (DEA's) [10], ionic polymer metal composites (IPMCs) [33], and biohybrid

actuators [34, 35, 36]. Mismatch strain-induced deformation refer to the (usually) 3D change of

shape in heterogeneous materials that is caused by differential straining in different layers of a

component. Such shape changes maybe induced in hard materials such as metals or semi-

conducting thin films [37, 38] , or in soft materials such as PDMS [39], or in hard-soft hybrid

systems [40]. Strain induced actuation technologies are highly scalable. Semiconductor micro-

and nanotubes have been formed by strain-induced self-rolling of membranes for

microelectromechanical systems (Figure 1.3b) [38, 41, 30, 29]. At the mesoscale, Motala et al

used optical lithography to produce regions of different stiffness's in a PDMS/SU8 sheets which,

when submerged in a solvent, underwent a variety of complex programmable folding designs due to differential swelling [39]. DEA's under Maxwell stress are capable both small and large strains [42, 43]. Such mismatch strain-induced deformations often lead to 3D curvilinear shape changes, forming, e.g., cylindrical tubes, spherical cups, or wavy edges [39, 44]. Sometimes the shape changes are time-dependent, especially if the deformation is induced by chemical processes or governed by diffusion [39, 45]. Highly nonlinear processes such as instabilities (to be discussed in more detail below) may also occurs in mismatch strain-induced deformation [40]. All these deformation modes can be utilized to generate actuation in soft biohybrid robots.

One of the most unique methods of mismatch strain is via biohybrid actuation. When a monolayer of muscle cells is cultured on a thin film and then the cells contract, it facilitates bending with in the biohybrid actuator. The curvature of this bending can be modeled using the Stoney Equation, which models the monolayer of cells as a coating which accommodates misfit strain so that the thin film is under stress. To maximize bending of cells on a thin film, cells must be well aligned. **In chapter 2**, we investigate cell-cell and cell-matrix interactions that facilitates cell alignment. Results of our study, show that smaller patterns on thin films can achieve cell alignment after the right confluency. This is useful in biohybrid robotics, where micro-scale mechanics are important considerations in promoting actuation via aligned muscle cells.

Elastic Instabilities

One challenge for soft robotics is that their actuations are often relatively slow. For fast reconfigurable architectures, soft robotics researchers exploit elastic instabilities. Instabilities in elastic systems cause buckling [46], wrinkling [45], and snap-through behaviors [47]. Such reconfigurable architectures can be ideal for an appropriate response to an external stimulus and

there are many ways to release elastic instabilities (e.g., chemically, thermally, magnetically, physically, etc.). One more specific example is based on how the venus fly trap is capable of rapid actuation by the release of elastic instabilities by chemical processes [48]. Inspired by this, Epstein et al. fabricated mechanically, pH-responsive colloidal particles capable of rapid actuation between configurations (Figure 1.3c) [22]. The bi-stability of the colloidal particles was derived from the colloids' spherical curvature that exhibited a snap through motion. Also, Ramachandran et al. developed a pre-buckled ferroelastomer beam that underwent buckling instabilities in response to an external magnetic field (Figure 1.3d) [31]. The snap-through mechanics were used to transition between open and closed-circuit configurations. Additional applications of elastic instabilities include programmable origami structures [49] and manipulating fluid flow [50]. Snap-through behaviors in bi-stable or multi-stable structures (i.e., the "jumping" of the structures from one equilibrium configuration to another), are often essential to achieve rapid change of shapes. The switch between stable to unstable configurations offers a lower power, rapid response to desired design objectives.

Bio-Inspired Design

While conventional robots rely on separate modular systems for sensing, actuation, and control, soft robots have the potential to integrate these features into their material architecture. Progress partly depends on new smart materials that allow for an "embodied intelligence". Smart materials couple optimal mechanical properties with desired features, such as programmable stiffness properties, simplified control, proprioceptive sensing, or contact modeling [51, 52]. For example, due to their high rigidity, traditional electrical connectors and electrodes are difficult to incorporate into soft structures, so new ways to be both mechanically and electrically coupled

are necessary. A promising solution is the inclusion of the liquid metals (e.g., Mercury, Galinstan, EGaIn and liquid silver), to create soft stretchable circuits that remain mechanically intact and electrically functional under extreme elastic deformations [53, 54, 55]. Such approaches represent practical methods for the inclusion of flexible sensors, interconnects, transistors, and conductors in soft robots [56, 57, 55]. For example, in biohybrid robotics electrodes for local stimulation of cells tend to be stiff which inhibits overall actuation. **In chapter 3**, we investigate the biocompatibility of EGaIn with in liquid metal embedded elastomers (LMEE) for its potential application for biohybrid actuators and medical devices.

Soft robotic actuation is not reliant on discrete joints but instead uses stiffness modulation of soft components (e.g., elastomer, gels, fluids, and biomatter) [2]. Inclusion of such non-rigid materials allows soft robots with continuous systems to exhibit theoretically infinite degrees of freedom. Computer-aided designs (CAD) and virtual models are typically used to assist in the design and actuation behavior of soft robots, but due to nonlinear deformation characteristics of soft components, large deformations are computationally expensive to simulate in real time [58, 59, 60]. Therefore, efficient solution techniques continue to be developed for useful coupling of modeling and control of soft robotic systems. One solution which offers useful, accurate control of robots is to couple continuum mechanics with path planning algorithms to allow for modeling reductions [23, 61, 62]. There is currently no general model to couple continuum mechanics with path planning, so soft robotic engineers often seek inspirations from nature to help inform control mechanisms in their design. In this section, we will elaborate more on bioinspired and biomimetic designs inspired by a range of biological systems.

Bio-Inspired Robotic Implementations

There are many important issues in functional design of a robotic system, such as sensing, actuation, memory, and control. Additionally, design engineers of robotic systems often need to consider more detailed specifications such as the robots' dynamic responses, morphological compatibility, and system-level integration. For soft robotic systems, engineers can take inspirations from nature and integrate many of their design principles into a holistic system.

Bio-Hybrid Systems

Engineers exploit features found in nature, not only by mimicking them, but also by interfacing with biological materials [35]. Bio-hybrid robots couple biocompatible synthetic materials with contractile muscle tissues (e.g., smooth, skeletal, and cardiac muscle cells) [63]. With the proper conditions, muscle cells can convert chemical energy into mechanical deformation, locomotion, and control of soft materials with many degrees of freedom [34]. Furthermore, bio-hybrid robots can functionally adapt to their environment, are capable of self-repair and self-assembly, and have developed very sophisticated actuation mechanisms to perform tasks at the micro- and meso- scale, which cannot be artificially replicated with currently available technologies [34, 36, 35]. These advantageous properties have inspired the development of biological machines such as muscular micro-walkers [44, 64, 65], micro-swimmers [66, 67, 68, 69], micro-grippers [44, 70], and even self-folding origami structures [71].

As discussed, bio-hybrid robotic actuation principle revolves around the principle of strain mismatch, similar to the operating principle of thin film actuators. In place of engineered materials such as metal or semi-conducting thin films, contracting cells on the surface of a soft robotic component act as a membrane straining layer [72]. Actuation behavior is determined by the biomaterial composition of the robot. In Figure 1.4b, Nawroth et al. developed an artificial

jellyfish that uses a thin layer of cardiac muscle cells to generate the mechanical deformation of a jelly fish [66]. The bending direction of the cell thin-film monolayer was generated by exploiting the ability for cells to self-organize along one direction. Coupling a mono layer of anisotropic cardiomyocytes with an elastomer caused the biohybrid robot to exhibit jellyfish-like kinematics and locomotion (Figure 1.4a). Notably, the artificial jellyfish is only capable of downward contraction as it swims and is therefore limited by the drag of its rebound stroke. Upward contraction against the drag would require an additional layer that can act antagonistically to the muscular thin film. A notable improvement of the design of the bio-hybrid robot comes from a tissue-engineered ray (Figure 1.4b). Unlike the jellyfish that is composed of two layers (PDMS and rat cardiomyocytes), Park et al. improved the design of an artificial sting ray that had four total layers. The artificial sting ray contains a skeleton structure that stores elastic energy during the down stroke of the muscle layer and releases that energy against drag during the subsequent muscle relaxation phase [73]. Phototactically stimulated contraction of serpentine rat cardiomyocytes patterns leads to coordinated swimming of the robot that emulates sting ray locomotion [73]. Such bio-hybrid robot design improvements allow for a dynamic level of control that had not been achieved before, as was demonstrated by the soft robot navigating through an obstacle course (Figure 1.4b). Furthermore, recent advances in biohybrid robotics have utilized muscle cells polarized with in a 3D-matrix to facilitate cell actuation [74]. Thicker muscle cell cultures allow for greater contractile forces which allow for larger biohybrid systems to be actuated. **In chapter 4**, we investigate a method to stack monolayers of cells on top of each other in order create biohybrid thickness for potential applications in modeling *in vivo* conditions and biohybrid actuators.
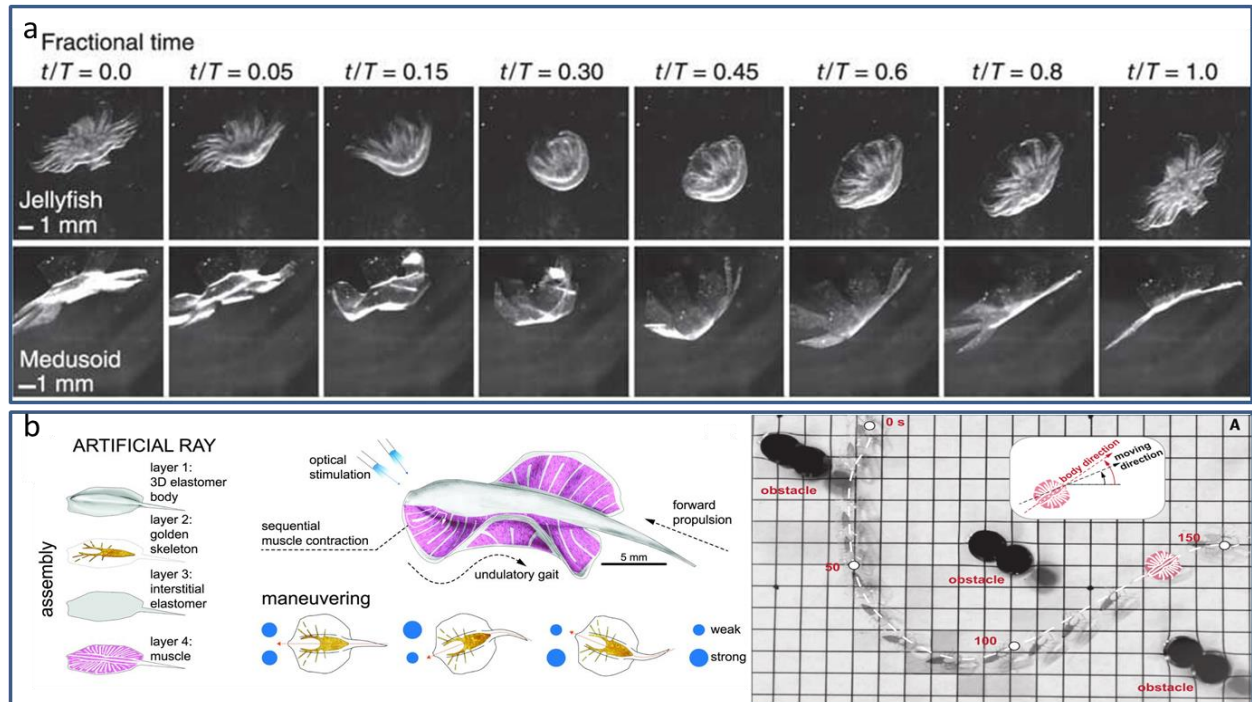
Figure 1.4 Biohybrid muscle cell based actuators (a) Time lapse of stroke cycle in jellyfish (top) and an artificial jellyfish (bottom) [66], (b) (left) A biohybrid assembly components that mimics the actuation behavior of a sting ray, (b) (right) Soft artificial ray navigates through an obstacle course [69].

Chapter 2 : Cell Alignment Modulated by Surface Nano-topography – Roles of Cell-Matrix and Cell-Cell Interactions

Introduction

Work in tissue engineering is frequently aimed at controlling the alignment of cells in 2D or 3D cultures *in vitro* to recapitulate microstructures of native tissues *in vivo*. Cell alignment plays a critical role in numerous biological functions from the formation of skeletal muscular tissue during embryonic development to maintaining vascular health as an adult. Therefore, effective methods to replicate biological functions in tissue engineering necessitates cell alignment. The clinical impact of cell alignment in tissue engineering has been articulated in a diversity of physiological systems from skin to heart to bone tissue [75, 76, 3]. At the intersection of cell alignment in tissue engineering is cell-substrate interactions, cell-cell interactions, and biological factors which are critical considerations for the design of engineered biomaterials designed to interface and integrate with tissues For example, Sawa *et al* has treated dilated cardiomyopathy in more than 40 patients by transplanting tissue engineered myoblast sheets [77]. In their study, interactions between cells and temperature-responsive substrates allowed for the controlled release and transplant of a monolayers of cells directly onto failed myocardium. Cell-cell junctions maintained the myoblast sheet integrity, and the biological factors between the transplanted myoblast sheets and cardiomyocytes facilitated fibrosis, angiogenesis, and local recruitment of stem cells. The transplanted engineered myoblast sheets improved cardiac function sufficiently to discontinue patient need of using left ventricular assist systems.

Cell-substrate interactions facilitate cell alignment through focal adhesion the binding processes between cell transmembrane molecules and the substrate. Cell adhesion can be

enhanced by extracellular matrix (ECM) absorption on the substrate surface resulting in cell-matrix adhesions. In this study, we focus on cell-matrix adhesion on fibronectin. One technique that can be used to modulate cell alignment on substrates is the introduction of anisotropy. Anisotropy has been used in various ways to induce cell alignment such as in topographical arrangement of geometric patterns, in stiffness gradients on scaffolds, and in the alignment of ECM networks surrounding cells. These techniques can be utilized in fabricating scaffolds on which cells grow into morphologies more closely resembling conditions *in vivo* [78, 79, 80, 81, 82, 83, 84, 85, 86, 87] . Our work is focused on anisotropic geometric patterns and its impact on cell responses. In particular, we investigate the effects of surface waviness on alignment of elongated cells.

The synthesis of tissues in these and related fields requires a fundamental understanding of the roles of ECM and mechanotransduction, which are essential in the formation and functionalities of engineered tissues. Such understanding requires comprehensive studies of how cells interact with ECM either as individual cells or collectively as cell constructs/micro-tissues [84].

The effects of anisotropic geometric patterns on cell-ECM surface interactions have been investigated by controlling the surfaces to which cells adhered. For example, mouse skeletal muscle cells (C2C12 cells), when seeded on sinusoidal surfaces with wavelengths ranging from sub-micrometer to micrometer scale, aligned along the direction of the wavy patterns [85, 88]. In a previous study, Grigola *et al* found that depending on the parameters of the sinusoidal wave (wavelength, amplitude, curvature, etc.), cells exhibited alignment either individually or after reaching a level of confluency [89]. The study found that both cell-ECM interaction and cell-cell

interaction have a role in cell alignment in 2D culture *in vitro* [89]. Furthermore, an alignment sensitivity parameter was proposed to characterize sinusoidal wavy topographies that led to cell-matrix interactions [89].

Cell alignment to topographical surface features is facilitated by mechanotransduction. Mechanotransduction is the process by which mechanical stimuli activate biochemical reactions and cellular responses, leading to gene expression, protein synthesis, and phenotypic change [90]. Mechanosensors and signal transduction are integral mechanisms of mechanotransduction that influence cell morphology and are affected by cell-matrix interactions [91, 92, 93, 94]. Mechanotransduction mechanisms for cell-matrix interactions and cell-cell interactions are similar but distinct [95]. The strengths of cell-matrix interaction and cell-cell interaction may be correlated, either positively or negatively. Following the work of Grigola *et al* [89], the objective of the current study is to gain a more in-depth understanding of the roles of cell-matrix and cell-cell interactions when sensing the geometric patterns of ECM surfaces.

To examine cell alignment in response to surface topography and cell-cell interactions, we developed controlled surface topographies on biocompatible polydimethylsiloxane (PDMS). We cultured cells on these nano-topographies to understand the effects of topography on cell alignment. We also introduced polyclonal anti-N-cadherin to inhibit cell-cell interactions to understand the impact of cell-matrix interactions on cell alignment (Figure 2.1). The effect of anti-N-cadherin was analyzed by comparing individual cell morphology and cell motility on patterned scaffolds with or without the anti-body. A sensitivity parameter was then implemented to understand the changes in cell response on controlled scaffolds. Furthermore,

time lapse imaging allowed us to compare the impact of time and confluency during cell alignment.
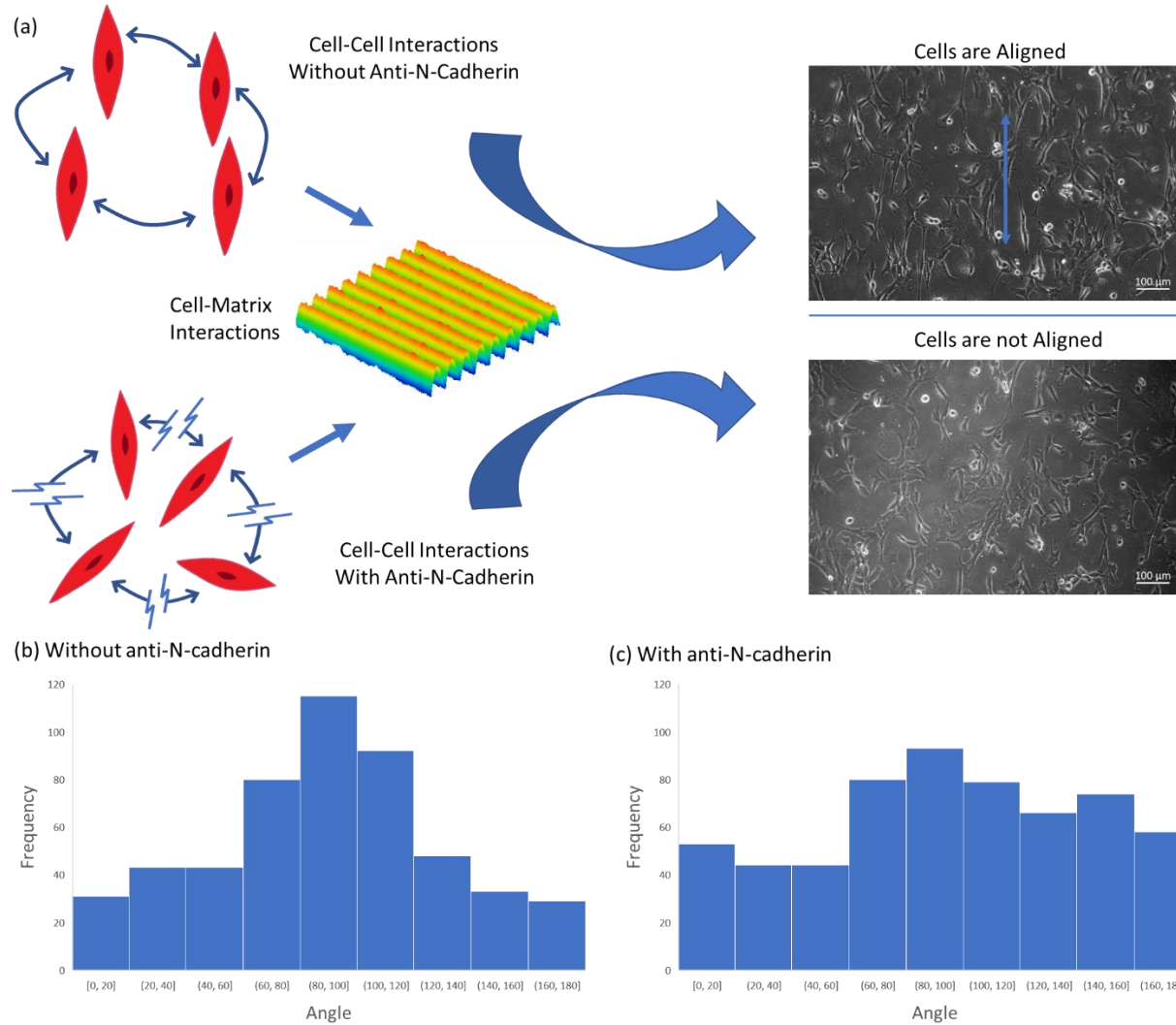
Figure 2.1 As cells are cultured onto patterned scaffolds, cell morphology is affected by both cell-matrix and cell-cell interactions. Anti-N-cadherin impacts cell-cell interactions giving rise to differences in cells' sensitivities to wavy surface topographies. (a) Illustration of different cell responses to surface patterns with and without anti-N-cadherin. (b) A histogram of the cell alignment measurements when cultured on a wavy surface without anti-N-cadherin. (c) A histogram of the cell alignment measurements when cultured on a wavy surface with anti-N-cadherin.

Materials and Methods

Sinusoidal Topography Substrates

A regular standing-sinusoidal wave pattern across the entire area for the cell culture was created (Figure 2.2). While PDMS wrinkling and soft lithography can be used to fabricate sinusoidal wave patterns [96, 97, 98] in this work, surface topographies on PDMS (Sylgard 184, Dow Corning) were fabricated through casting using commercially available holographic diffraction gratings. Holographic diffraction gratings (Edmund Optics #43-775, #54-509, #40-267) were used as templates for molding PDMS. PDMS was mixed at a 10:1 ratio, degassed, then a small drop was sandwiched between an oxygen plasma cleaned glass coverslip and the template with a weight on top, degassed again, cured at 60° overnight for plastic templates or 37° overnight for glass templates, then the coverslip and template were gently separated leaving a thin PDMS layer on the coverslip; PDMS samples made from glass templates were further cured at 60° and flat PDMS samples were produced in a similar manner by using the reverse side of the plastic templates. Sinusoidal wavelengths and amplitudes were measured by atomic force microscopy to be: $\lambda=2$ µm with d~170 nm, $\lambda=1$ µm with d~130 nm, and $\lambda=0.56$ µm with d~150 nm. Substrates were sterilized with 70% ethanol for 30 min, exposed to UV germicidal light for 1 hour in a biosafety cabinet, then incubated with 10 µg/ml fibronectin (Corning 356008) in PBS for 1 hour at 37°. Following this, the fibronectin solution was removed, substrates were washed with PBS, and complete growth media was added in preparation for cell seeding. The PDMS molding sometimes results in reduced amplitude of the grating due to the fragility of the grating. The change in amplitude, however, allows for the scaffolds with differing aspect ratios to be used with cell culture [88].

Atomic Force Microscopy and Scanning Electron Microscope

The topology of the cell scaffold was characterized by atomic force microscopy using an Asylum Research MFP-3D Infinity system. Standard Tapping AFM tips used for surface characterization had a full cone angel of 40° and tip radius of < 8 nm. The AFM cantilever had a force constant of 40 N/m and resonance frequency of 325kHz (NanoAndMore USA). The scan area was 100 μm^2 with 256 x 256 points. SEM images were acquired using a Quanta 600 Environmental Scanning Electron Microscope with EDX and OIM.

Time Lapse Imaging

C2C12 cells (American Type Culture Collection - ATCC) were seeded on the patterned side of the PDMS scaffolds at 10,000 cells/cm^2. Cells were cultured in Dulbecco's Modified Eagle Medium (DMEM, ThermoFisher 11995065), supplemented with 10% Fetal Bovine Serum (ATCC 30-2020) and 1% Penicillin (ATCC 30-2300). Cells in the presence of anti-N-cadherin (Thermofisher PA5-29570) were cultured at a concentration of 5 μg/ml. After one hour, cells were treated either with or without the presence of anti-N-cadherin antibodies for 48 to 72 hours while being cultured in the Zeiss Large Incubation Chamber XL-S1. Cell media was replaced every 24 hours. Time lapse images were compared between cell cultures using images captured with a 10x objective on a Zeiss AxioObserver Z1 Phase Contrast Microscope. Time lapse intervals were every 15 minutes. Cell migration was tracked using the ImageJ plugin MTrackJ [99].

We characterized the alignment of cells during timelapse imaging using custom-written software in python and ImageJ (see Supplementary Information). In each frame or image taken an alignment score was assigned based on cell alignment. The alignment score was derived based on the angle individual cells in an image which were determined ImageJ. The ImageJ plug-in PHANTAST was also used to compare cell confluency of an image to its cell alignment score since

confluency impacts cell alignment [100]. Calculating both the confluency of cells and an alignment score for each image or frame from a timelapse video allowed us to directly compare the correlation between the two. All experiments of cells with or without the antibody on samples with either the wavelengths 0.56 μm, 0.83 μm, 1 μm and 2 μm were replicated at least 3 times.

Immunostaining

C2C12 mouse myoblast cells were cultured at 37°C with 5% CO_2 in DMEM (Gibco 11995065) supplemented with 10% FBS (GE HyClone SV30160.03HI). Cells were trypsinized, counted with a hemocytometer, then seeded onto substrates in complete growth media at densities of 4,000 cells/cm^2 and 32,000 cells/cm^2 for low- and high-density conditions, respectively. Cells were allowed to attach and grow on the substrates for 18-20 hours and were subsequently fixed in warm 4% formaldehyde for 15 minutes, permeabilized in 0.2% Triton X-100 for 10 minutes, blocked in 1% bovine serum albumin (BSA) for 1 hour, incubated with primary antibodies diluted in 1% BSA for 1 hour (anti-vinculin, clone hVIN-1, Sigma-Aldrich V9131, 1:200), incubated with secondary antibodies diluted in 1% BSA (Thermo Fisher A11031, 1:400) and phalloidin (abcam ab176753, 1:400) for 1 hour, stained with 1 μM DAPI (abcam ab228549) for 5 minutes, and mounted for microscopy (ProLong Gold Antifade mountant, Thermo Fisher P10144, or 90% glycerol). Between each treatment in staining, cells were washed thrice with PBS with 5 minutes between each wash.

Immunostaining Imaging and Data Analysis

Fluorescence microscopy was performed with either Nikon Ti-U (Nikon Plan Fluor 40x/0.75 objective, Nikon Intensilight C-HGFI light source, pco.panda 4.2 sCMOS camera, NIS-Elements D software, 162.5 nm/pixel, 2044x2048 pixels, and 0.11 mm^2 image size, for large-scale cell

alignment imaging, Figure 2.3) or a Zeiss Axio Observer Z1 (EC Plan-Neofluar 100x/1.3 oil objective, HXP 120C light source, AxioCam MRm CCD camera, Zen 2 software, 64.5 nm/pixel and 1388x1040 pixel image size, for high-resolution focal adhesion imaging, Figure 2.4) inverted epifluorescence microscope setups. Fields of view were randomly chosen throughout the samples.

Immunostaining data was analyzed using custom-written Python programs. Briefly, the local orientation of actin at each pixel was determined from phalloidin images using the gradient structure tensor weighted by a Gaussian with 5 pixel (813 nm) standard deviation; pixels with coherence (difference of eigenvalues divided by the sum of eigenvalues) less than 0.4 were discarded. Nuclei in each field of view were counted from DAPI images by binarizing the image, taking a distance transform on the binarized image, and employing a watershed algorithm on the distance transform. The nematic order parameter for a field of view was calculated similar to Gupta et al as $S=<\cos [2(\theta- \pi/2)]>$, where θ is the local angle of actin at each pixel from groove direction and the average was weighted by the fluorescence intensity at each pixel [27].

Atomic Force Microscopy (AFM) and Scanning Electron Microscope (SEM)

Before cell culture, the topography of bare cell scaffolds was characterized by AFM using an Asylum Research MFP-3D Infinity system under both dry and aqueous conditions. Characterization of topography of surfaces used in timelapse imaging were in a dry environment using an Asylum Research MFP-3D Infinity system. Standard Tapping AFM tips used for surface characterization had a full cone angle of 40° and tip radius of < 8 nm. The AFM cantilever had a force constant of 40 N/m and resonance frequency of 325kHz (NanoAndMore USA HQ:NSC15/Al BS). The scan area was 100 µm^2 with 256 x 256 points. To ensure the quality of surface patterns

upon coating ECM, surfaces are characterized by AFM both before and after coating of fibronectin in buffer solution (Figure 2.2b, c). The probe used had a force constant of 0.350 N/m and a resonance frequency of 65 kHz (Bruker DNP-S10). Measurements of the surface height of wavy topographies with wavelength 0.56 μm, 1 μm, 2 μm was repeated for 3 regions for 6 different samples. Detailed images and data of the characterization of the wavy surface topography are given in the Supplementary Materials. The AFM and SEM images of wavy surface with wavelengths 0.56 μm, 1 μm, and 2 μm are shown in Figure 2.2. SEM images were acquired using a Quanta 600 Environmental Scanning Electron Microscope with energy-dispersive X-ray and Orientation Imaging Microscopy.

Alignment Sensitivity Parameter of Scaffolds

A non-dimensional parameter Φ, referred to as the alignment sensitivity parameter by Grigola *et al* [89], was used to characterize the geometric features of the wavy patterns:

$$\Phi = \sqrt{\frac{\lambda d}{L^2}}/(1 + \frac{k^{-1}}{L})$$

where λ is the wavelength, *d* is the amplitude, and *κ* is the effective curvature of the sinusoidal surface, and *L* is the size of typical cells when as they spread [89]. The alignment sensitivity parameter correlates with the likelihood of cell alignment on a given smooth, curved sinusoidal topography. The effective curvature, *κ*, is proportional to the curvature for sinusoidal patterns, which is d/λ^2. For a fixed *d*, as the *λ* becomes larger, the effective curvature term in the denominator begins to dominate. This captures the fact that the surface appears effectively flat to an individual cell as the effective curvature value approaches 0 either by decreasing d or increasing *λ*. A cell length dimension for C2C12 cells of *L* = 60 μm was chosen to

nondimensionalize the data related to the alignment sensitivity parameter. Grigola *et al* showed

that the cell alignment behavior is relatively insensitive to the selection of *L* [89].

Statistical Analysis

The data in this study are expressed as mean and error bars that represent ± standard deviation.

In order to evaluate statistically significant differences in cell alignment with or without anti-N-

cadherin, an F-test was used to determine significant variance between groups and defined as P

values less than 0.05.

Results
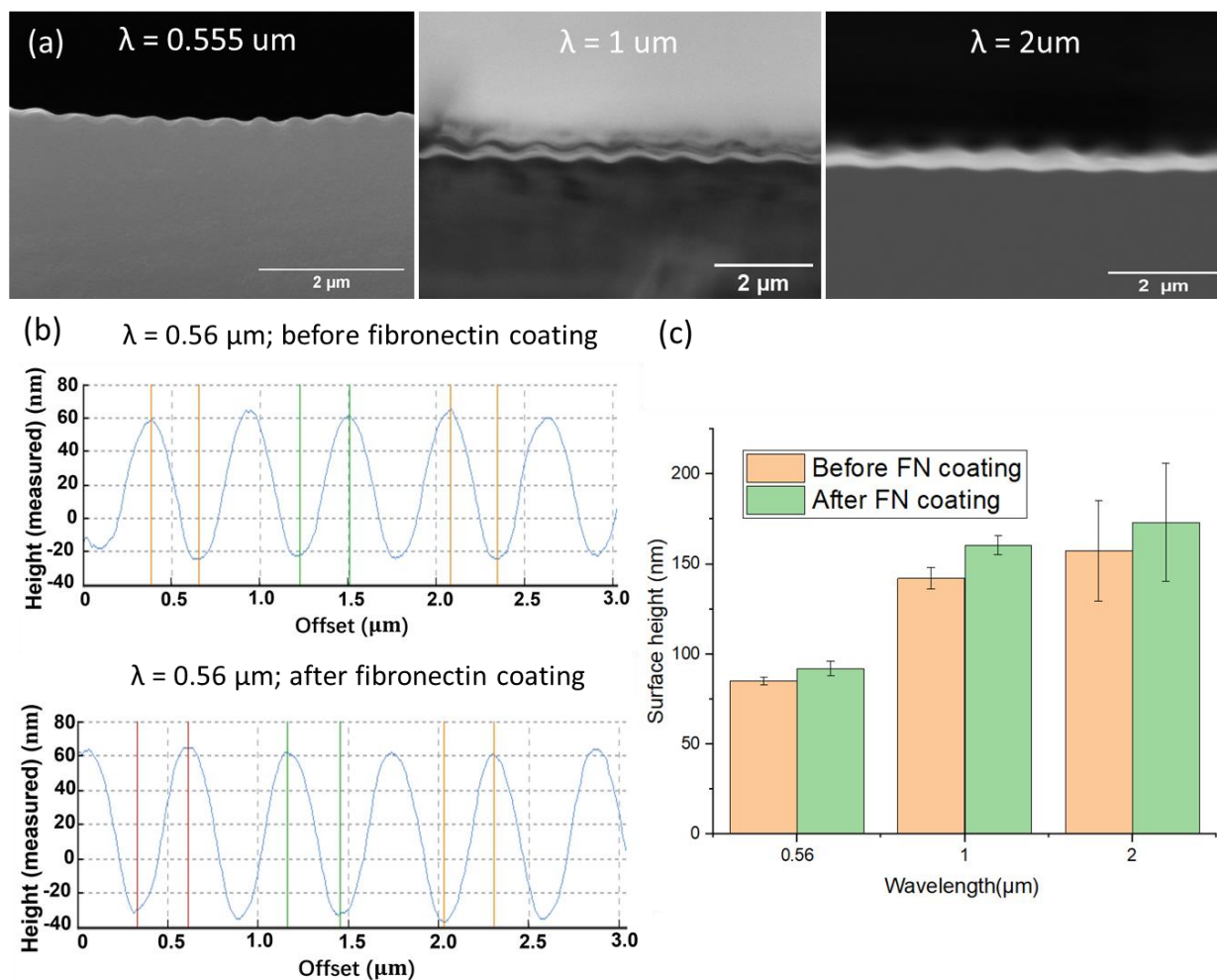
Figure 2.2 SEM images (a) of the cross section of each surface pattern on PDMS before fibronectin coating. The surface is facing upward in each SEM image. AFM images of surface profile (b) and bar chart (c) of patterned side of PDMS scaffolds. The surface profile and bar chart compares AFM data before and after fibronectin coating. The sinusoidal periodic patterns can be described by their wavelength λ, and surface height d. Error bars represent standard deviations of measured surface height of n = 18 for each profile.

Cell Alignment and Cell Density

Cells were seeded at low and high densities, allowed to grow for 18-20 hours, then immunostaining was performed to visualize vinculin- a cell-substrate and cell-cell adhesion protein, and actin (Figure 2.3a, b). We quantified the local orientation of actin at each pixel in an image as a proxy for the global cell alignment and correlated this with the observed cell density

by counting the number of cell nuclei. On flat PDMS substrates, no preferential alignment was observed. On sinusoidal topographies, at low densities, we observed slight bias in alignment along the direction of the grooves in all the wavelengths tested, with 2 μm wavelength providing the strongest bias (Figure 2.3a, c). At high densities, the alignment along the groove direction was significantly enhanced in all wavelengths (Figure 2.3b, d, e). This result was consistent with previous work [89], both in that cell alignment was enhanced on the longest wavelength substrate and at higher cell densities.
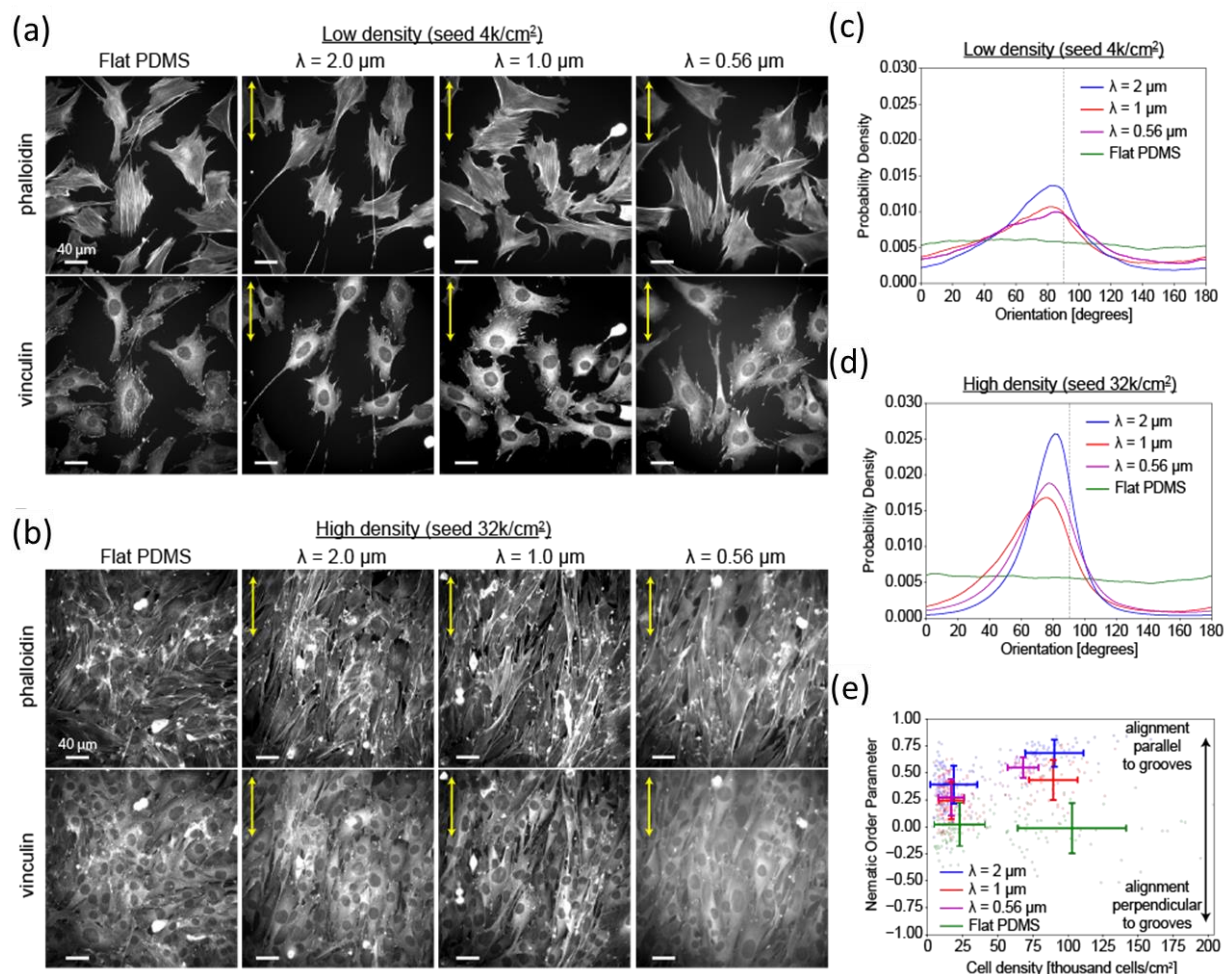
Figure 2.3 Cells exhibit large-scale alignment along the direction of the sinusoidal topography. (a) Cells seeded at low density on flat PDMS and sinusoidal topographies of 2 µm, 1 µm, and 0.56 µm (left to right), stained for actin (top) and vinculin (bottom). Groove direction is vertical and indicated by the yellow arrows. (b) Similar as (a) except for cells seeded at high density. (c) Probability density of actin orientation for flat PDMS (green) and sinusoidal topographies with wavelength 2 µm (blue), 1 µm (red), and 0.56 µm (magenta) for cells seeded at low density. Black dashed line indicates vertical direction. Data is merged from 2 independent experiments and 94 fields of view per condition. (d) Same as panel (C) except for cells seeded at high density. Data is from one experiment and 50 fields of view per condition. (e) Scatterplot showing the nematic order parameter versus the cell density for each field of view. Solid lines indicate the mean and standard deviation for each condition. Scale bars: 40 µm.

On sinusoidal topographies and at low cell densities, we observed two distinct types of cell-substrate adhesions (Figure 3.4a). The first type was aligned along the direction of the grooves, which had a lateral spacing consistent with the wavelength of the grooves and were

27

larger for 2 μm wavelength grooves and correspondingly smaller for 1 μm and 0.56 μm wavelengths grooves. These adhesions were prevalent on lamellipodia-like protrusions. The second type was angled with respect to the groove direction, either diagonally or orthogonally, and for 2 μm wavelength grooves were often discontinuous while cells on 1 μm and 0.56 μm wavelength grooves were able to form large, continuous focal adhesions. These larger, thicker focal adhesions were usually associated with actin stress fibers. As the cell density increased and cells aligned along the direction of grooves, these large, angled focal adhesion complexes were no longer visible on any sinusoidal substrate. The only cell-substrate adhesions that remained were largely oriented parallel to the grooves (Figure 2.4b). Cells seeded onto flat PDMS substrates could form large focal adhesion complexes in any direction, even at higher cell densities.

Quantifying Cell Alignment

Cells were cultured on sinusoidal patterned surfaces . The alignment sensitivity parameter, Φ, was used to characterize the likelihood of cell alignment on a smooth sinusoidal topography for a given wavelength and amplitude. Grigola *et al.* found that when $0.01 < \Phi < 0.1$, cells exhibited greater alignment on sinusoidal surfaces as confluency increased and when $\Phi > 0.1$, cells exhibited strong polarization regardless of cell confluency. We utilized anti-N-cadherin to perturbed cell-cell interactions on topographies where confluency promotes alignment. At the same confluency, cells cultured in the presence of anti-N-cadherin exhibited lower alignment on surfaces with where $0.01 < \Phi < 0.1$ (Figure 2.5a). On surfaces where $\Phi > 0.1$, there was little difference in cell alignment between cells in the presence of anti-N-cadherin verses without (Figure 2.5b).
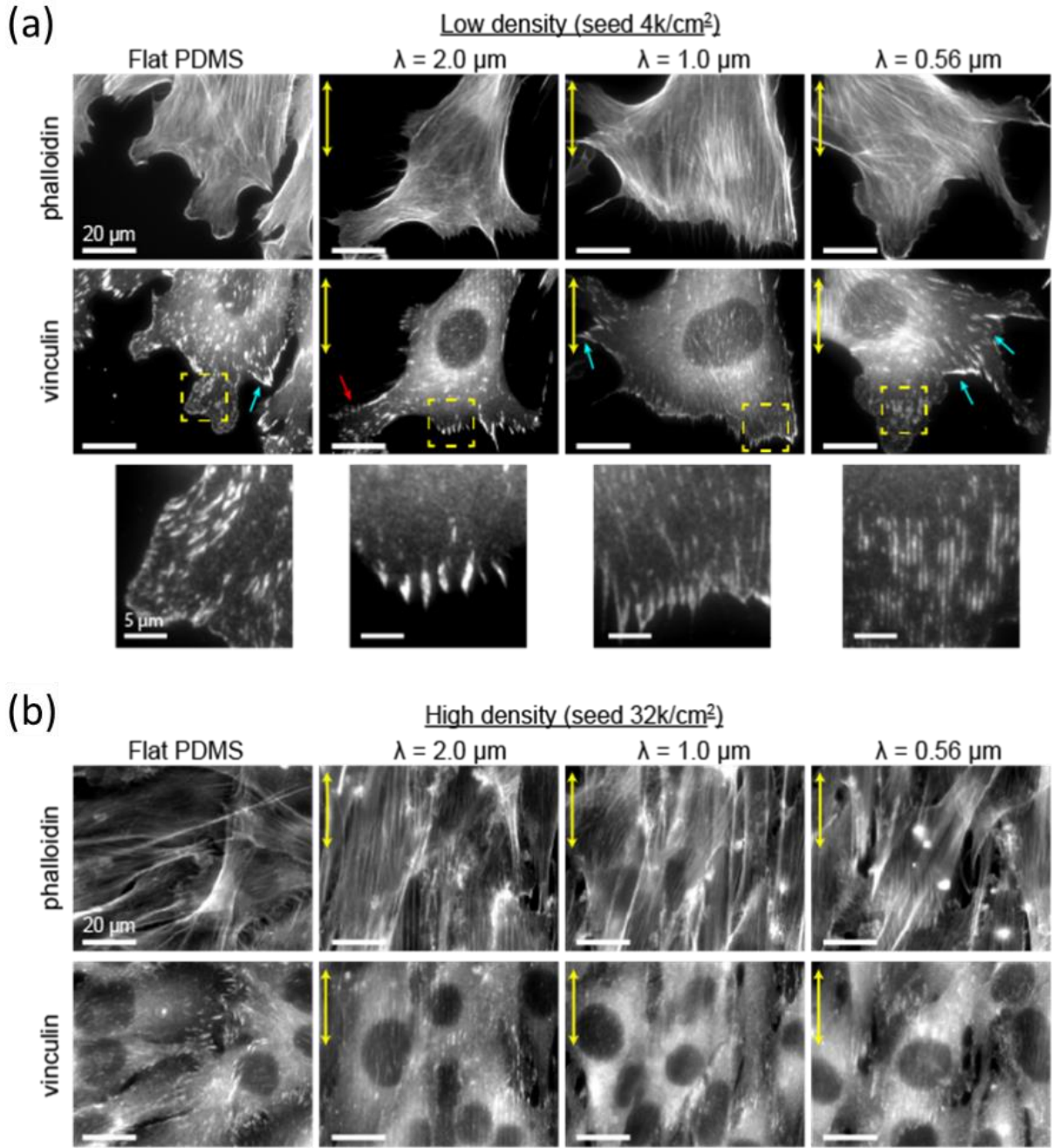
Figure 2.4 Focal adhesion morphology on sinusoidal topographies. (a) Cells seeded at low density on flat PDMS and sinusoidal wavelengths of 2 µm, 1 µm, and 0.56 µm (left to right), stained for actin (top) and vinculin (middle). The groove direction is vertical and indicated by the yellow arrows. Zoomed inset areas are shown in yellow boxes. Cyan arrows indicate focal adhesions which form at an angle to the grooves, while red arrow indicates adhesion which is oriented at an angle relative to the groove but is discontinuous. (b) Similar as (a) except for cells seeded at high density. Scale bars: 20 µm, or 5 µm (insets).

Quantifying Cell Motility

Time lapse imaging of cells on scaffolds has been used in fields varying from gene expression analysis to 3D tissue formation [101]. For our work, time lapse videos were captured of cells cultured on various surface topographies for tracking motility and overall culture organization. In figure 6, C2C12 cells were cultured on flat (Figure 2.6a, c, e) and patterned (Figure 2.6b, d, f) surfaces for characterization. In each time lapse video, 10 cells were tracked to measure their position (Figure 2.6a, b) and instantaneous angle (Figure 2.6c, d). The centroid of each cell was manually tracked to determine the position of cells over 72 hours. To better quantify these results, the motility of cells was tracked by N number of points where pi = (x_i, y_i) is the position of a cell. The instantaneous angle is the most recent displacement vector from the previous N point to the current N point of the tracked cell. The instantaneous angle is defined by α = arctan $[(y_{i+1} - y_i)/(x_{i+1} - x_i)]$.
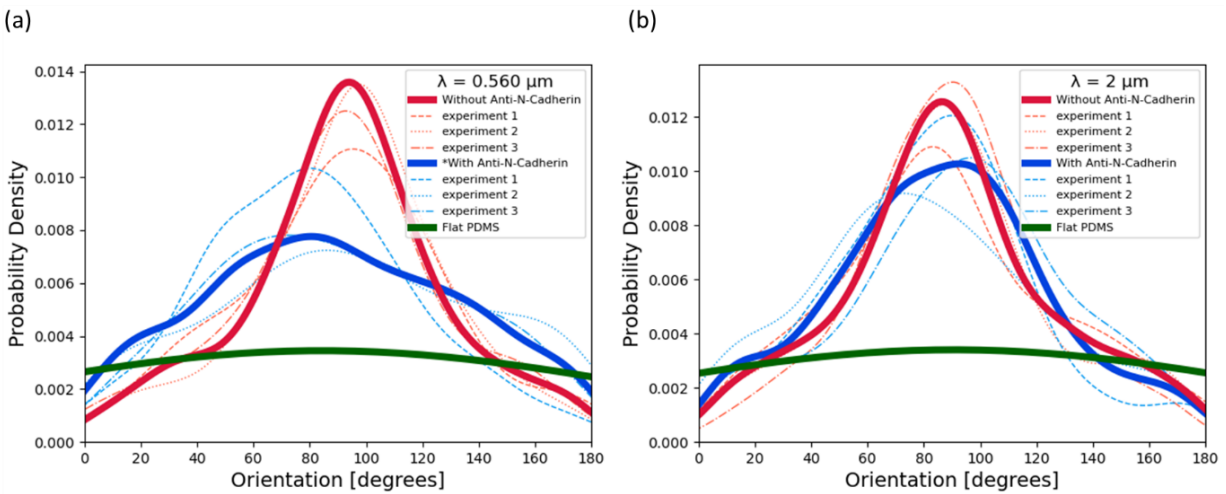
*Figure 2.5 Probability density function of cell orientation when cultured on micro patterned PDMS with λ = 0.56 μm (a) and λ = 2 μm (b). At each wavelength cells orientation was compared when cell culture was with (blue) or without anti-N-cadherin (red). Solid lines are combined probability density functions of dashed lines from individual experiments. Cell orientation was compared when confluency reached 41±6% (n=3). Green line is probability density function of flat PDMS. Flat PDMS data was used for both λ = 0.56 μm and λ = 2 μm. When λ = 2 μm, Φ > 0.01. When λ = 0.56 μm, 0.001 < Φ < 0.01. *P < 0.05 versus normal C2C12 cell culture on the same wavelength.*
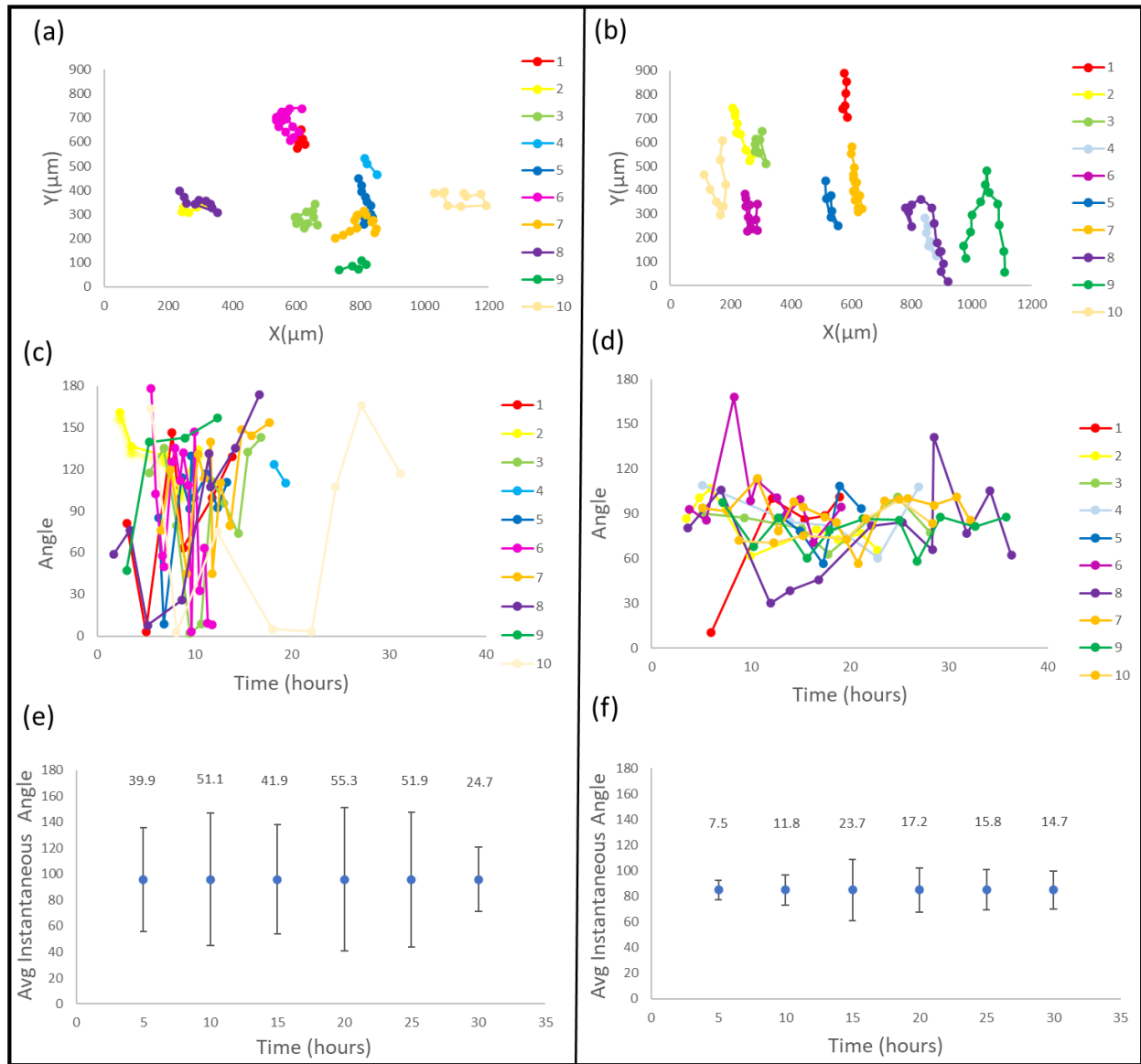
Figure 2.6 The position (a, b), angle (c, d), and instantaneous angle change (e, f) were tracked for ten randomly selected cells cultured on a flat (a, c, e) vs patterned surface (λ=2 μm, d=450nm, φ = 0.0138) (b, d, f). Cell motility was tracked from the beginning to end of their cell cycle. The displacement vector is the instantaneous angle of cells between cell positions in each frame. Cell movements to the right is 0° and to the left is 180°. Movement up or down is 90°. The error bars (e, f) represent the standard deviation of the instantaneous angle.

To compare models of high verses low cell alignment, cell responses on flat (Figure 6a, c, e) or patterned surface with $\Phi > 0.01$ (Figure 2.6b, d, f) were compared. Tracking motility of cells cultured on a flat surface exhibited no preferential orientation for movement, and the instantaneous angle measured as the cells migrate is nearly random, giving rise to a broad scattering of migration direction (Figure 2.6a, c, e). On the other hand, on the patterned surface with $\Phi > 0.01$, cells migrate along the direction of the microgroove channels, leading to a strongly preferred direction of migration, as demonstrated in Figure 6b, d, f.
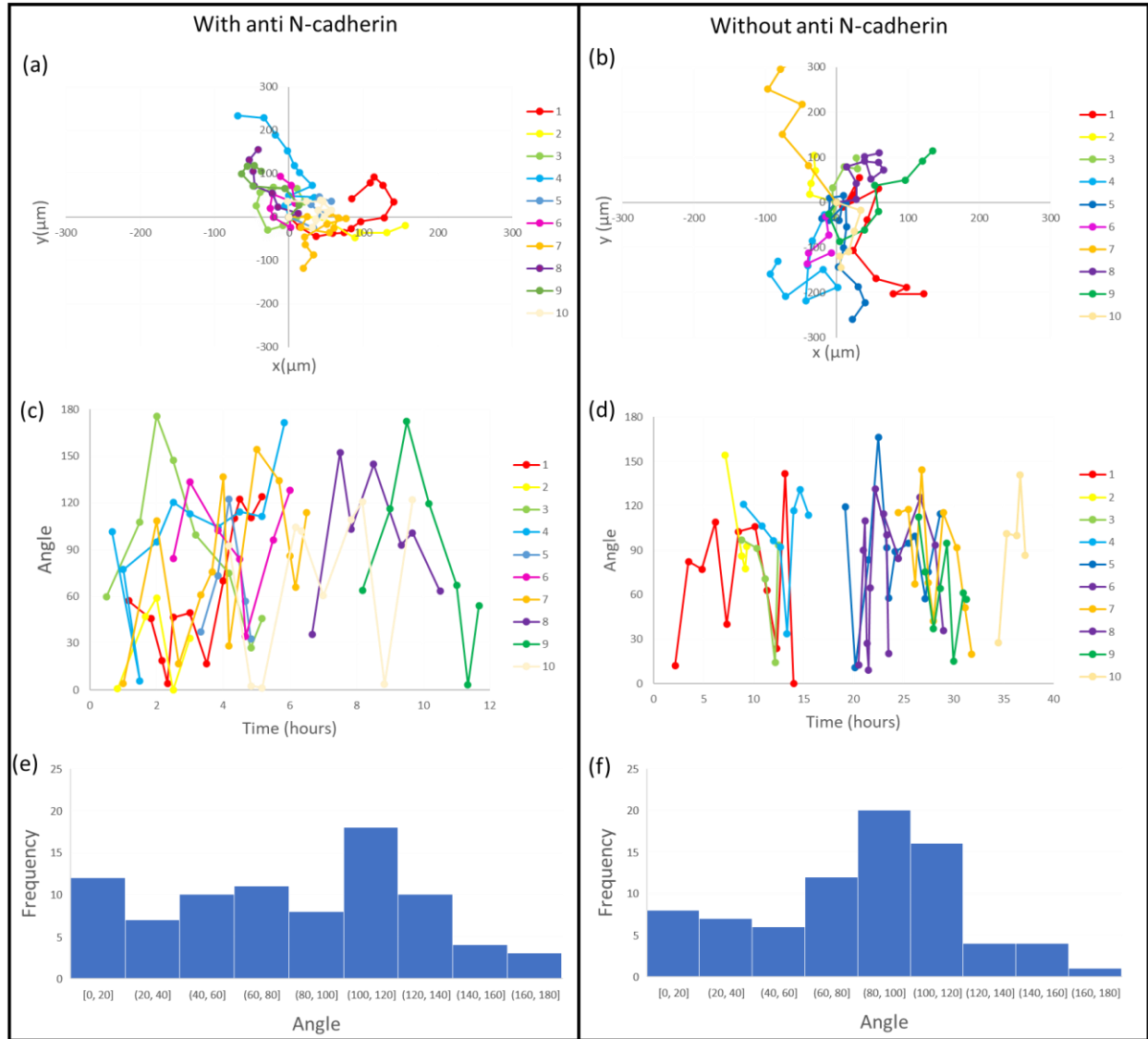
Figure 2.7 Cells were cultured on the same surface in the presence (a, c, e) and absence (b, d, f) of anti-N-cadherin on a scaffold with a sinusoidal wavy topography (λ=0.83 μm, d=77 nm, and Φ=0.004). The cell position (a, b), instantaneous angle (c, d), and a histogram of all instantaneous angles (e, f) were compared between cells cultured with and without anti-N-cadherin. Cells in the presence of anti-N-cadherin were less polarized and exhibited a lower degree of alignment than cells cultured without anti-N-cadherin.

To investigate the role of cell-cell interactions in cell responses to patterned surfaces, cells were cultured on the same surface in the presence (Figure 2.7a) or absence (Figure 2.7b) of anti-N-cadherin. By tracking the cell positions throughout its cell-cycle, cells cultured without anti-N-cadherin exhibited greater preferential movement along the microgroove channels. A histogram

33

of the instantaneous angle between cell positions was more uniformly distributed for cells cultured with anti-N-cadherin than without the antibody (Figure 2.7e, f).

Role of Cell-Matrix Interaction in Cell-Alignment

Cell responses to patterned surface features are modulated by cell-matrix interactions and mechanotransduction via scaffold geometries. Mechanical cues from scaffold geometries influence overall cell culture organization via cell-surface receptors which initiate intracellular responses related to cell motility and morphology [102]. Scaffold surface geometries with a Φ greater than 0.01 induce individual cell alignment via cell-surface receptors [81, 89]. Cells cultured with or without anti-N-cadherin on surfaces with a Φ greater than 0.01 exhibited no difference in cell alignment behavior throughout cell proliferation (Figure 2.8a). On the other hand, cells interfacing with scaffolds with a value of Φ less than 0.001 would not align regardless of cell confluency, similar to cell responses on a flat surface [89]. It is likely that, below the Φ threshold of 0.001, cell-surface receptors would not sense the patterned surface and responded to surface topography because the surface is essentially flat [89].

Role of Cell-Cell Interaction in Cell-Alignment

When Φ is between 0.001 and 0.01, the necessity for cell confluency to achieve cell alignment suggests that cell-cell interactions enhance sensitivity of cell-matrix interactions, which could be through a variety of molecular mechanisms [103]. Isolating the role of intracellular and intercellular responses can inform cell alignment's dependence on cell-cell and cell-matrix interactions. To examine phenotypic responses to cell-cell and cell-matrix interactions, anti-N-cadherin was utilized to examine the role of cell-cell interactions in cell culture related to surface topography. The selected anti-body inhibits cell-cell junctions by specifically binding to several

locations on the extracellular domain of the protein [103, 104, 105]. Inhibiting the adhesion molecule has an important role in the biochemical pathways of intercellular responses by mediating calcium-dependent homophilic cell-cell interactions [103]. When Φ was between 0.001 and 0.01 and cells were in the presence of anti-N-cadherin, cells required a greater percentage of confluency in order to align with the microgroove channels (Figure 2.8b).

Discussion

In addition to our focus on surface topography, it is important to note the role of fibronectin as ECM in facilitating mechanotransduction via focal adhesions. C2C12 myoblasts grown on fibronectin show greater cell alignment than on laminin or gelatin and greater collective directional migratory behavior than gelatin *in vitro* [106]. This is likely because fibronectin is recognized by many different cell-surface receptors of the transmembrane integrin family [107, 108]. Many of these focal adhesion binding sites in fibronectin are RGD peptide specific [109]. One study by Vaz *et al* found that inhibiting RGD-binding integrins with GRGDS peptide resulted in complete detachment of C2C12 cells from fibronectin-coated glass coverslips [106]. Fibronectin and RGD-binding integrins in C2C12 cells, such as $\alpha5\beta1$, $\alpha v\beta1$, and $\alpha v\beta3$, constitute a primary pathway for intracellular force transmission [106, 108, 109].

The mechanisms suggest that the observed anisotropy in cell morphology and collective migratory behavior may originate from the prestress residing in intracellular stress fibers oriented preferentially along the long axis of the cells [110]. Observed differences in actin fiber and focal adhesion alignment between cells cultured on patterned verse flat PDMS helped illuminate the role of cell-matrix adhesion and cell alignment (Figure 2.3, 2.4). Actin fiber alignment is relevant because cell motility is initiated by actin-dependent lamellipodia along the

cells leading edge, followed by the cell body being pushed forward through intracellular contraction forces [111, 112]. The dependence of cell alignment to matrix topography suggests cell sensitivity to cell alignment is, in part, dependent on physical phenomena. While cell-matrix adhesions helps elucidate the role of mechanotransduction and cell alignment in 2D, studies have shown that cells in a 3D matrix interact with distinct behaviors to that of adhesions formed in a 2D matrix [113].

There are many pathways of cell signaling that are activated by various cadherin-mediated cell-cell contacts. These cadherins are crucial in mediating homophilic cell-cell adhesions and facilitating cell proliferation, fusion, and maturation. While much about cell signaling is unknown, recent studies suggest downstream signals from cadherin-mediated contacts are both cadherin-specific and cell-context-specific [114]. Well studied cadherins of C2C12 cells such as M-cadherin, R-cadherin, E-cadherin, and N-cadherin have cell-context-specific roles during proliferation and differentiation *in vitro*. Increased expression of R-cadherin results in myogenesis inhibition and myoblast transformation [115]. In addition, the expression of R-cadherin is accompanied by a delocalization at the membrane junction of the endogenous expression of N-cadherin and M-cadherin [115]. A study by Ozawa found expressing E-cadherin cytoplasmic domain ectopically in C2C12 myoblasts inhibits cell-cell fusion and elicits delocalization of M-cadherin and N-cadherin [116]. All of these cadherin-mediated contacts activate the Rho family of GTPases, which play a critical role in cytoskeleton-dependent cell functions, such as cell morphology [117]. Although knocking out or inhibiting a specific cadherin cell-cell contacts is not sufficient to abrogate its specific function, several downstream signals mediating by cell morphology and proliferation are still perturbed. This study focused on the

inhibition of N-cadherin since it affects RhoA activation, which is believed to regulate cytoskeleton morphology and cell motility distally from the cell surface [118, 119].

In addition to our study that suggests cell-cell communication promotes cell alignment, other studies have shown cell-cell communication regulates myogenesis in C2C12 cells [120]. While the focus of this study is of cell alignment in 2D, the transition from 2D to 3D cell alignment offers another dimension of complexity more comparable to *in vivo* conditions. Isolating the role of cell-cell verses cell-matrix interactions is more complex as there are differences in adhesion protein expression of two- versus three-dimensional cultures *in vitro* [121].

Insights of cell-cell interactions in this study are particularly relevant in informing future scaffold designs in the fields of tissue engineering, regenerative medicine, and cell-based soft robotics. We found that cell-cell interactions promote alignment on smaller wavy patterns, that individual cells do not align on. Perturbing cell-cell attachment of confluent cultures on smaller wavy patterns inhibits cell alignment, meaning that smaller patterns on scaffolds can achieve cell alignment at the right confluency. This can be useful in fields such as biohybrid robotics, where micro-scale mechanics are important considerations in promoting actuation via aligned muscle cells [3, 122].

(a) λ = 2 μm; Amplitude = 400 nm

(b) λ = 555 nm; Amplitude = 165 nm
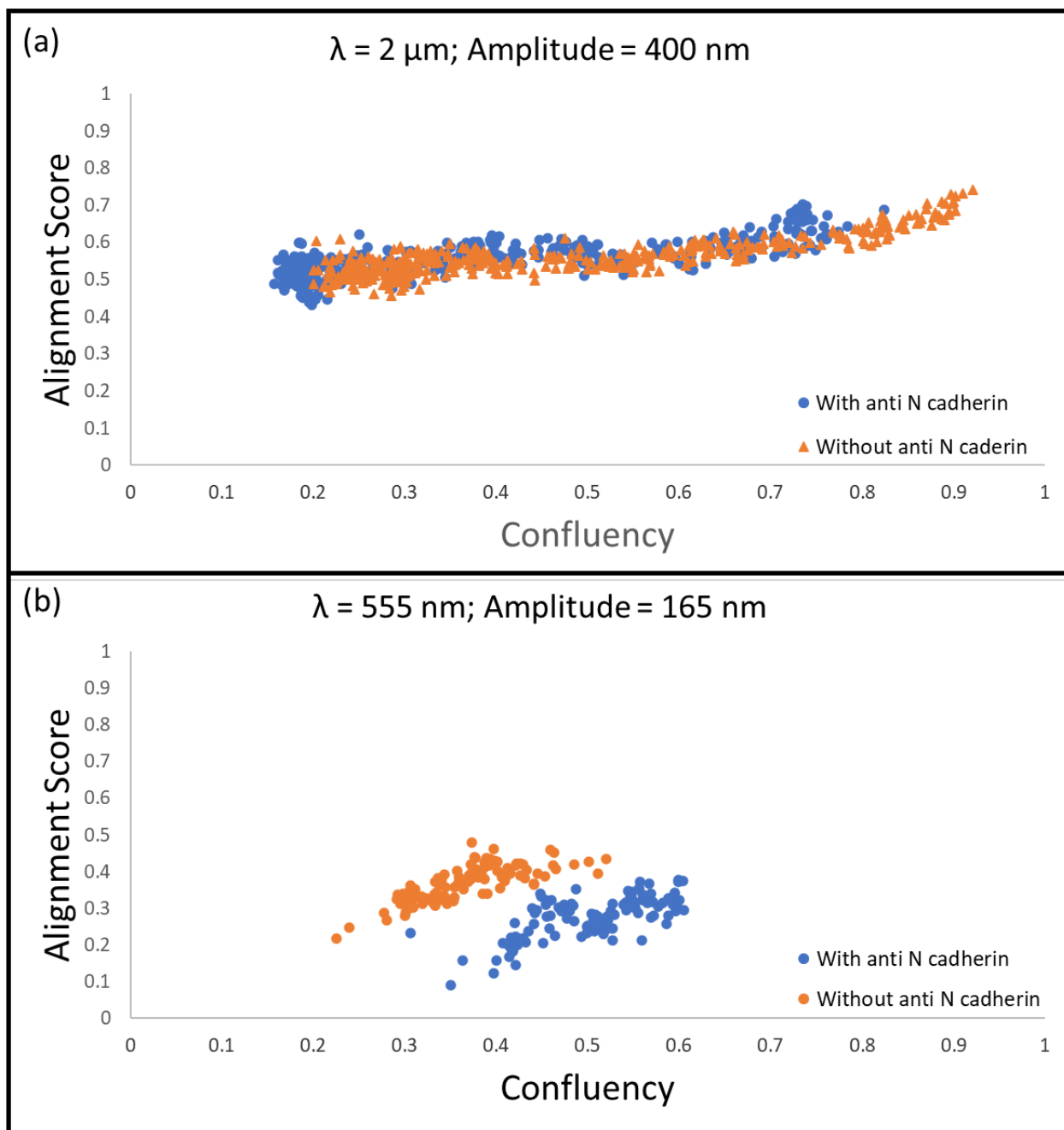
Figure 2.8 Time lapse videos that compared cells cultured with or without anti-N-cadherin on the same surface with a Φ greater than 0.01 (a), had a similar trend in net alignment, regardless of confluency. Cells cultured on the same surface when Φ value was between 0.001 and 0.01 (b), showed a direct relationship between cell alignment and cell confluency. Cells cultured in the presence of anti-N-cadherin required greater confluency to have the same alignment score (b).

Conclusion

Cell-cell interactions play an important role in cell alignment in 2D culture, especially when examining surface topography. We probed how cell confluency and cell-cell interactions impact cell alignment on different surface topographies. We first developed an approach to fabricate wavy topographies for cell culture. Then we captured time lapse videos of cells cultured on wavy topographies to investigate the role of cell-cell interactions and cell alignment. We found that cell-cell interactions can be altered through anti-N-cadherin. On surfaces with sensitivity parameter, Φ, ranging between 0.001 and 0.01, when cells were more confluent, they were better aligned along the channels of the anisotropic sinusoidal wavy patterns. However, cells in the presence of anti-N-cadherin required higher confluency than cells without anti-N-cadherin to be aligned (Figure 2.8b). On surfaces with Φ greater than 0.01, cell alignment was not dependent on confluency and the cells were aligned even at low percentages of confluency. We observed no difference between cell cultures with and without anti-N-cadherin when the value of Φ was greater than 0.01. To our knowledge, our study is the first to show the difference that cell-cell interactions make in promoting cell alignment on wavy topographies to which cells are otherwise not responsive. Further studies that isolate the role of cell-cell and cell-matrix interactions in cellular organization will inform the role of mechanotransduction in developmental biology, especially in 3D culture.

Supplementary Materials
Quantification of cell orientation

Cell alignment during experiments was characterized by imaging processing tools in ImageJ. The protocol to preprocess each image was derived from previous studies that automated quantification of cell alignment [123]. Preprocessed images were converted to a binary image.

Based on circularity, cells are selected and outlined. Individual cells are counted and measured by area, centroid, and center of mass using the analyze particles operation in ImageJ. The operation detected every cell and fitted an ellipse around it to determine their angle (Figure 2.9). The center of the ellipse was the same as the centroid of the cell. Angle (0-180 degrees) of each of every cell calculated is the angle between the primary axis and a line parallel to the x-axis of the image. A histogram of the cell angles calculated after image processing is shown in figure 10.
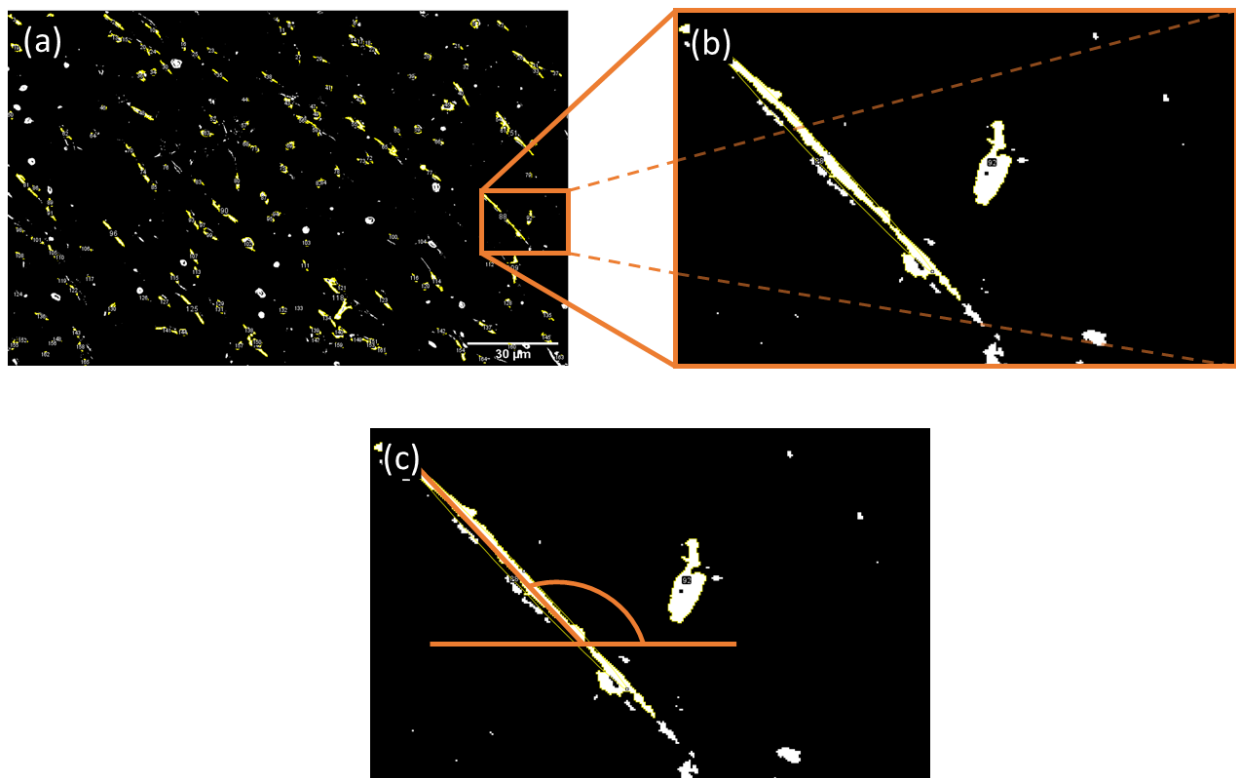
Figure 2.9 Individual cells in (a) post processed images have (b) an ellipse that is fitted around it to determine its angle. (c) The angle (0-180 degrees) of every cell calculated is the angle between the primary axis and a line parallel to the x-axis of the image.
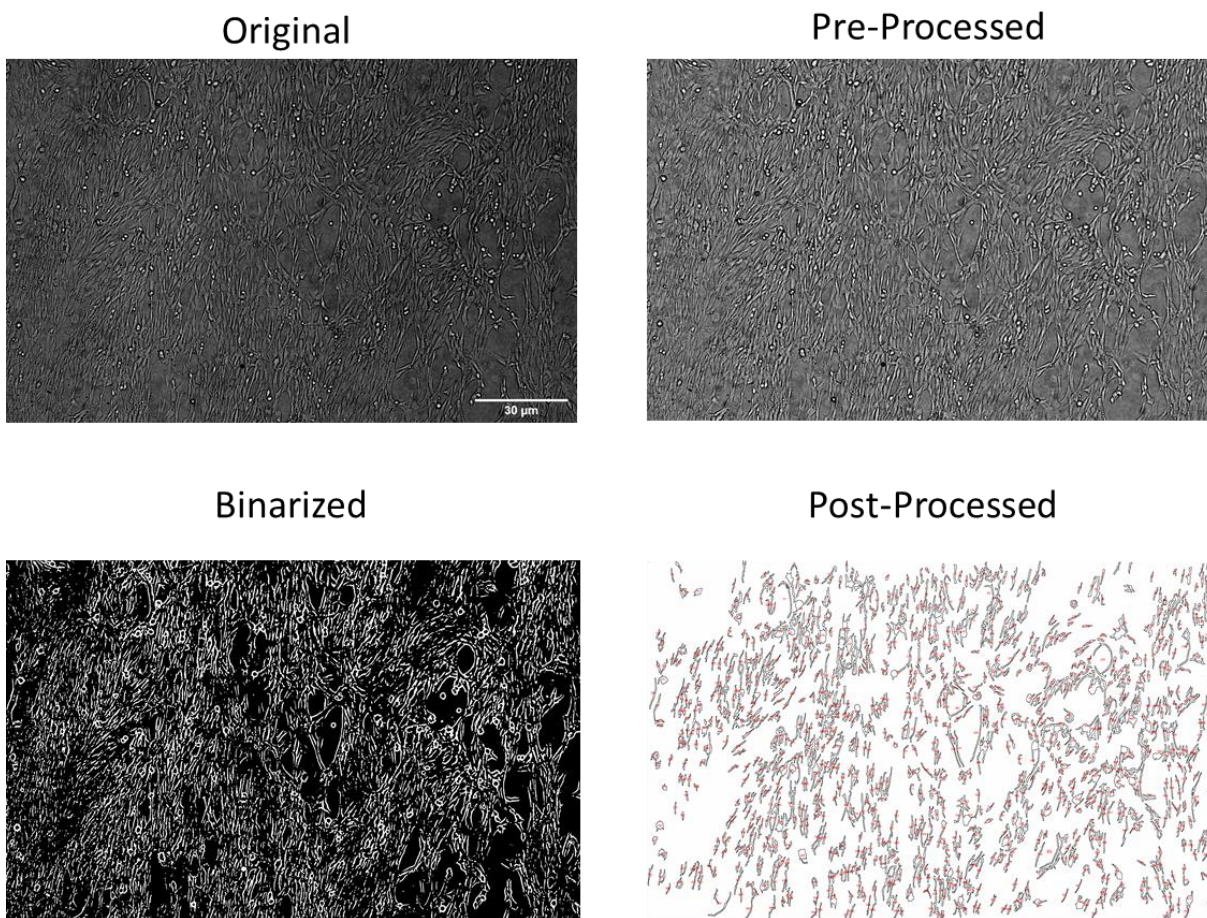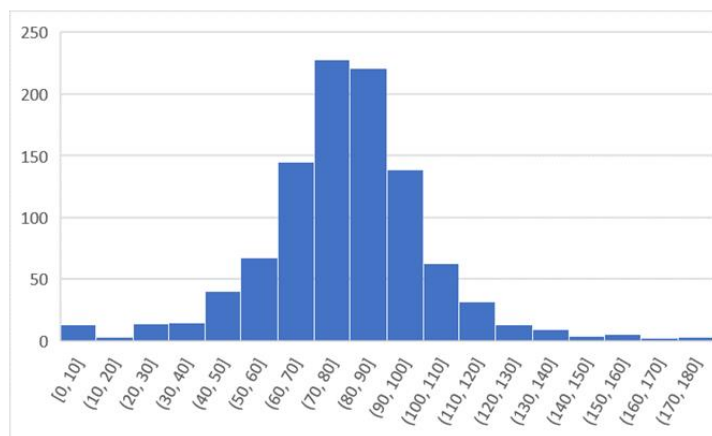
Figure 2.10 Sequence of image processing techniques to determine determined the alignment score by each individual cell properties. An original image was pre-processed to create a binary image the differentiates each cell individually in an image. Post-processing techniques determined several characteristics of each individual cell. The histogram shows the net angle orientation of the 1015 cells in found in the original image.

Cell Length	λ (nm)	Amplitude d(nm)	Effective Curvature(nm^{-1})	ϕ
60000	830	77	1.12E-04	3.67E-03
60000	560	100	3.19E-04	3.75E-03
60000	560	165	5.26E-04	4.91E-03
60000	560	170	5.42E-04	4.99E-03
60000	830	135	1.96E-04	5.14E-03
60000	830	190	2.76E-04	6.24E-03
60000	1000	200	2.00E-04	6.88E-03
60000	1000	210	2.10E-04	7.08E-03
60000	2000	200	5.00E-05	7.91E-03
60000	2000	250	6.25E-05	9.30E-03
60000	2000	400	1.00E-04	1.28E-02
60000	2000	450	1.13E-04	1.38E-02

Table 1 Summary of experimental data for patterned geometries tested in timelapse imaging. Results are listed in ascending order of ϕ.

Cell Alignment Score and Confluency Calculations

An alignment score was assigned for each frame in the time lapse videos. The alignment score was calculated based on the net orientation angle of individual cells in a culture. The angle of each individual cell was calculated using image analysis tools built into ImageJ. For consistency, the orientation of the diffraction pattern that cells were cultured on was 90 degrees (parallel to the vertical axis of the frame). Cells orientated ± 15 degrees of the diffraction pattern were determined to be aligned. Cells outside of this range were not aligned. Cells randomly orientated resulted in a culture that was ≈ 16.6% "aligned". The percentage of cells aligned to the grooves was normalized to create an alignment score on a scale of 0 to 1. The surface that cells were seeded on in figure 2.10, had an alignment sensitivity parameter value, Φ = 0.0093. After 72 hours of cell culture, the calculated alignment score of cells in this frame was 0.706.
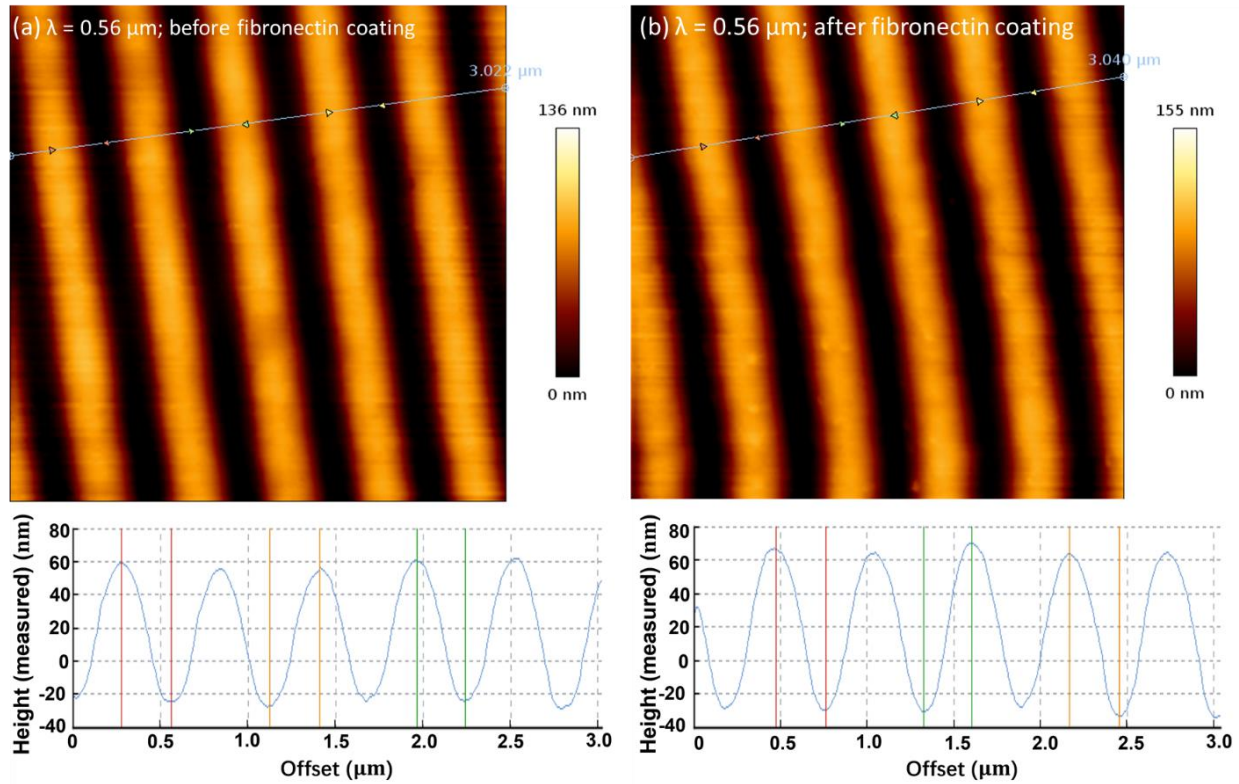
Figure 2.11 Comparison of the profile of a wavy topography before (a) and after (b) it was coated with fibronectin. The wavelength is 0.56 µm.

Characterization of Surface Topography with and without Fibronectin Coating

The topography of substrates was characterized using atomic force microscopy (AFM) before fibronectin was coated on to the surface for cell culture. A non-dimensional parameter Φ, referred to as the alignment sensitivity, was used to characterize the measured topography of AFM images (Table S1). To understand the impact of fibronectin coatings on surface topographies, AFM measurements were taken before and after fibronectin coating in buffer solution (Figure 2.11, 2.12, 2.13). The results confirm that the wavelength of the wavy surfaces is not altered by the fibronectin coating. However, we found that fibronectin coatings slightly increased the amplitude of the sinusoidal pattern on substrate surface (Table S2). The effect of

fibronectin was consistent across the entire surface of each substrate. Fibronectin had no impact

on the curvature of each of the samples.
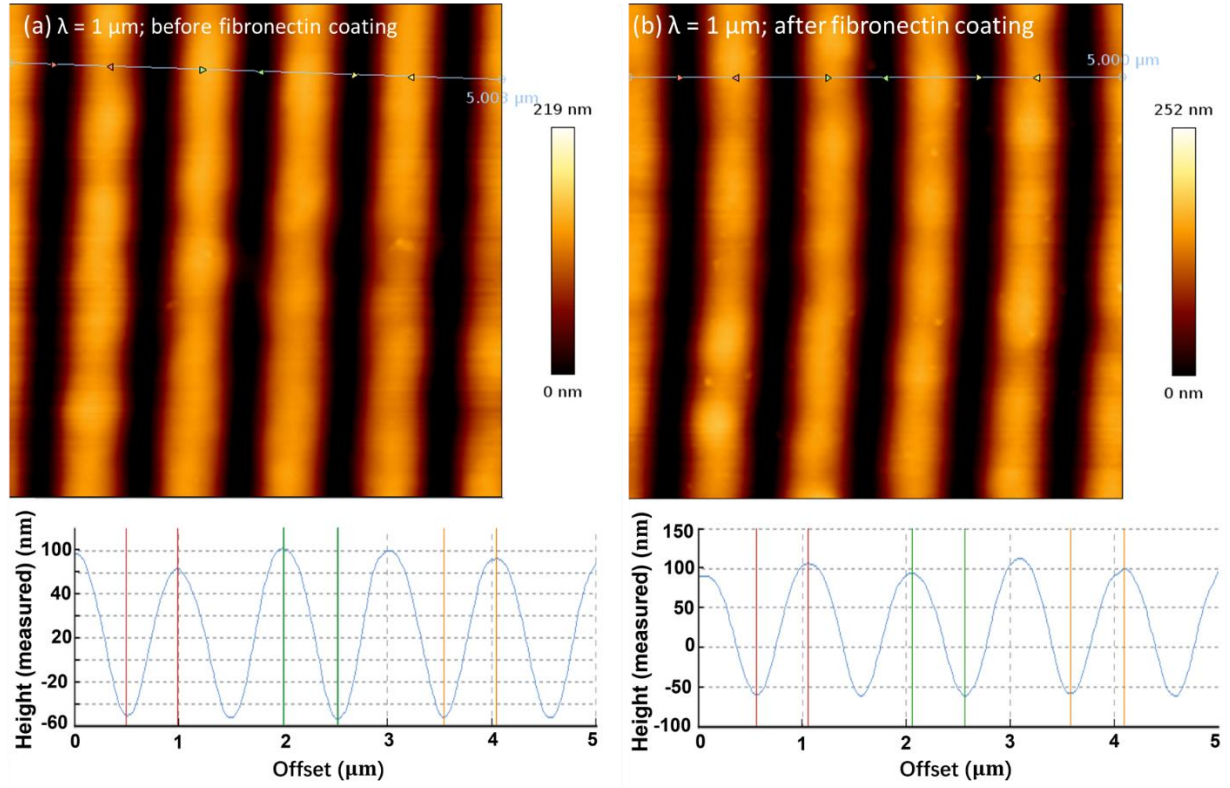
Figure 2.12 Comparison of the profile of a wavy topography before (a) and after (b) it was coated with fibronectin. The wavelength is 1 μm.
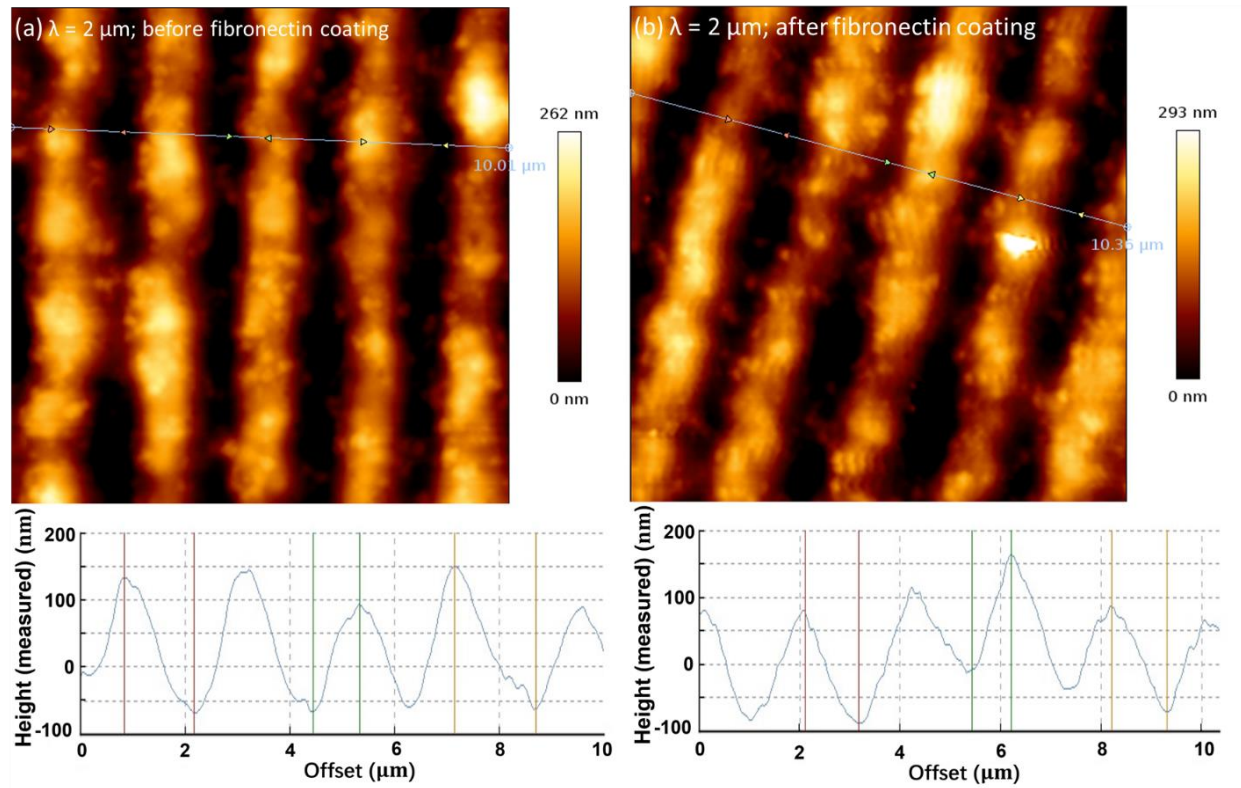
Figure 2.13 Comparison of the profile of a wavy topography before (a) and after (b) it was coated with fibronectin. The wavelength is 2 μm.

λ = 0.56 μm samples before FN coating	λ = 0.56 μm samples after FN coating	λ = 1 μm samples before FN coating	λ = 1 μm samples after FN coating	λ = 2 μm samples before FN coating	λ = 2 μm samples after FN coating
Height (nm)	Height (nm)	Height (nm)	Height (nm)	Height (nm)	Height (nm)
Region1	Region1	Region1	Region1	Region1	Region1
87.1	99.1	145	162	145	144
84.6	95.8	137	153	135	149
89.4	93.7	135	157	215	138
Region2	Region2	Region2	Region2	Region2	Region2
88.2	87.5	142	159	130	150
86.7	93.6	146	159	182	193
84	90.5	153	159	163	181
Region3	Region3	Region3	Region3	Region3	Region3
87.7	93.7	145	158	166	277
82.8	94.6	139	160	128	215
87.7	98.1	143	162	131	195
Region4	Region4	Region4	Region4	Region4	Region4
83.7	92.1	150	169	189	133
82.8	95.2	146	155	145	159
85	85.8	137	161	214	163
Region5	Region5	Region5	Region5	Region5	Region5
84.3	88.7	148	164	159	168
84.6	87	147	164	144	171
84.9	93.9	136	161	135	158
Region6	Region6	Region6	Region6	Region6	Region6
81.9	91.9	138	158	121	191
83.7	90.1	142	153	149	158
82.9	84.8	130	174	183	175

Table 2 Summary of AFM data characterizing surface topographies before and after fibronectin coating

Chapter 3 : Biocompatibility of Liquid Metal Embedded Elastomers

Introduction

All muscles are composed of linear actuators that enable movement through excitation and contraction. Many approaches have been proposed to integrate engineered muscles with scaffolds and soft materials, leading to artificial biohybrid devices that would allow robots to mimic biomechanics the same way living organisms do. To date, biohybrid actuators consist of a muscle tissue cultured on an elastomeric substrate and have demonstrated movements— such as grasping, walking, and swimming—by employing design strategies inspired by locomotion found in nature [3]. Although the degree of structure-function relations may differ with many factors such as the hierarchical architecture of muscles, skeletal and cardiac muscle cell lines have been the most frequent candidates for biohybrid actuators due to their comparatively higher contractile force when external stimuli (electrical, optical, chemical) are applied [124]. The primary difference between these muscle cell types is that skeletal muscle tissues contract precisely with respect to the application of a stimuli, in contrast to the spontaneous and rhythmical actuation of cardiac muscle tissues [124]. However, in either case, there lacks what can provide biocompatible conformal interface with these cells which would provide locally, functional electrical stimulation to the tissue in a more precise, spatial temporal actuation of a biohybrid system.

To facilitate biohybrid actuation, liquid metal (LM) alloy, specifically eutectic gallium-indium (EGaIn; melting point 15.5 °C), is highly conductive ($\sigma = 3.4 \times 10^6$ S/m) and easily processable with many other polymer matrixes to make a composite [125]. EGaIn mixes well into

other matrixes because it is liquid at room temperature, and it forms gallium oxide layers that works as a surfactant. Although it is known that gallium-based alloy has low cytotoxicity because of low vapor-pressure, there was evidence that EGaIn can be toxic to cells after ion releases of Ga^+ and In^+ in an aqueous environment when EGaIn is mechanically agitated or sonicated [126]. Thus, it could become cytotoxic under certain conditions such as incubation time, forms of the EGaIn structure, and environment. However, liquid metals can still be an appropriate candidate as an electrode material for soft electronics if there is a strategy to promote its biocompatibility while maintaining its metal-like conductivity in a stretchable form.

In this study, we investigate methods to improve and optimize the biocompatibility of EGaIn so that the material can be used in biohybrid systems. Since EGaIn can be transformed into either bulk, particulate, or a composite material due to versatility of its fluidic properties, the degree of cytotoxicity maybe modulated by encapsulating EGaIn materials. We present a muscular liquid metal embedded elastomer (LMEE) comprised of mouse skeletal muscle cells (C2C12 cells), cultured directly on surface patterned LMEE so that it could perform as biohybrid actuator via electrical stimulation. It has been a challenge to integrate the skeletal muscle tissue with soft material that is biocompatible and conductive. To overcome this limitation, we have employed LMEE, which has single micron sized droplets of EGaIn confined in polydimethylsiloxane (PDMS) elastomeric matrix, to combine the high electrical conductivity of EGaIn with the mechanical compliance and low cytotoxicity of PDMS. In addition, we also have thoroughly studied the topological and volumetric content dependency of the liquid metal droplets in LMEE by varying processing times of shear mixing conditions. The biocompatibility test with C2C12 cells has revealed that cell viability is highly dependent on the droplet size and

volume contents of liquid metal, both leading to the increased LM are at the surface of the LMEE. Thus, having an appropriate volume content with the smallest droplets is needed for fabricating soft, elastic, conductive, and biocompatible material regardless of external agitation or mechanical stirring in the growth medium. Benefits of this research addresses three major technical problems in biohybrid robotics: (1) it allows stimulation in close contact to the cells which allows the use of lower applied voltages, (2) it incorporates microelectrodes into bio-hybrid actuators without compromising rigidity of system, and (3) it localizes stimulation applied to specific regions of the bio-hybrid actuator [36].

Materials and Methods
Synthesis of Liquid Metal Embedded Elastomer (LMEE)

To synthesize eutectic gallium indium (EGaIn), the bulk gallium and indium (Ga 75 %, In 25 % by weight; Rotometals) were placed and heated in a glass vial for 20 hours at 200 °C. Meanwhile the matrix polymer, polydimethylsiloxane (PDMS, Sylgard 184; Dow Corning) mixed at 10:1 ratio was prepared. EGaIn was added into the uncured prepolymer at the desired volumetric concentration (50%, 60%, or 70%) and mixed using an overhead stirrer (OS20-S, SCILOGEX) at 200 rpm by different time variations. The uncured LMEE composite was then casted in a mold with a thickness of 1 mm throughout the cytotoxicity tests, unless otherwise noted. Ecoflex-LMEEs were fabricated by adding EGaIn into the uncured prepolymer at the desired 60 % volumetric concentration and mixed using an overhead stirrer for 10 minutes (OS20-S, SCILOGEX) at 200 rpm.

Surface Area Measurement

The scanning electron microscope (SEM) image was captured using the desktop SEM (Phenom XL). The SEM images were analyzed using the software, ImageJ, to measure the exposed EGaIn area at the LMEE surface. The data was then plotted in a separate data analytic program.

Mechanical and Electro-Mechanical Characterization

 The LMEE samples were prepared in a dog-bone geometry (ASTM D412) and were tested on a universal testing system (UTS) (5969, Instron) at a strain rate of 5 mm/min[1] for all tensile testing experiment. The samples were prepared in different EGaIn concentrations for the characterization, but consistent with 70 vol % for electro-mechanical and long-term stability tests. For electro-mechanical characterization, they were all electrically activated by undergoing 30 % of strain using a customized stretcher prior to the experiment. The electromechanical tests were done from measuring the resistance versus at given strains using a micro-ohm meter (34420A, HP) with a four-point probe. The external analog data from the materials testing machine and voltage signal from the voltage divider circuit were collected using a USB DAQ (USB-6002, NI) with a sampling rate of 300 Hz through the serial interface (MATLAB, 2019a).

Cell Culture

PDMS, EGaIn-PDMS, EcoFlex, and EGaIn-EcoFlex samples were sterilized in 70% ethanol and rinsed in deionized water for cell culture. After drying, the samples were plasma oxidized for 60 seconds at 18W (PDC-32G) and then coated with 50 μg/mL of fibronectin (SIGMA) from human plasma for 1 hour. Excess fibronectin was aspirated, and then the samples were washed in a PBS bath. Mouse myoblast C2C12 cells (ATCC) were seeded on the patterned side of the PDMS scaffolds at 10,000 cells/cm2. Cells were cultured in growth medium comprised of Dulbecco's

Modified Eagle Medium (DMEM, ThermoFisher 11995065) supplemented with 10% Fetal Bovine Serum (ATCC 30-2020) and 1% Penicillin (ATCC 30-2300). Cell media was replaced every 24 hours until the start of adding cell differentiation media at ~70% confluency. Differentiation of cells was achieved by switching growth medium with differentiation medium at ~70% confluency. The differentiation medium comprised of DMEM (Gibco 11965) supplemented with 2% horse serum (HyClone SH30074.02) and 1% Penicillin (ATCC 30-2300).

Cell Culture Polyurethane Nanofibers

EGaIn polyurethane nanofibers (PU NF) and PU NF samples for cell culture were sterilized in 70% ethanol and rinsed in deionized water. After drying, PDMS samples were plasma oxidized for 60 seconds at 18W (PDC-32G) and then coated with 50 µg/mL of fibronectin from human plasma (SIGMA) for one hour. Excess fibronectin was aspirated, and then the PU NF samples were washed in a PBS bath. Mouse myoblast C2C12 cells (ATCC) were seeded on the patterned side of the PDMS scaffolds at 10,000 cells/cm^2. Cells were cultured in Dulbecco's Modified Eagle Medium (DMEM, ThermoFisher) supplemented with 10% Fetal Bovine Serum (ATCC) and 1% Penicillin (ATCC).

Cell staining

Fluorescent imaging was conducted 1, 3, and 5 days after initiating cell culture using live/dead stains (LIVE/DEAD Viability/Cytotoxicity Kit, Thermofisher). A staining solution of 5 µL calcein AM (Component A) and 20 µL ethidium homodimer-1 (Component B) to 10 mL DPBS was prepared. The culture medium was removed from cells and replaced with staining solution directly to cells. Cells were incubated for 30 minutes. Since the samples were not opaque, they were inverted onto their top surface and fluorescent images taken using the CSU-X1.
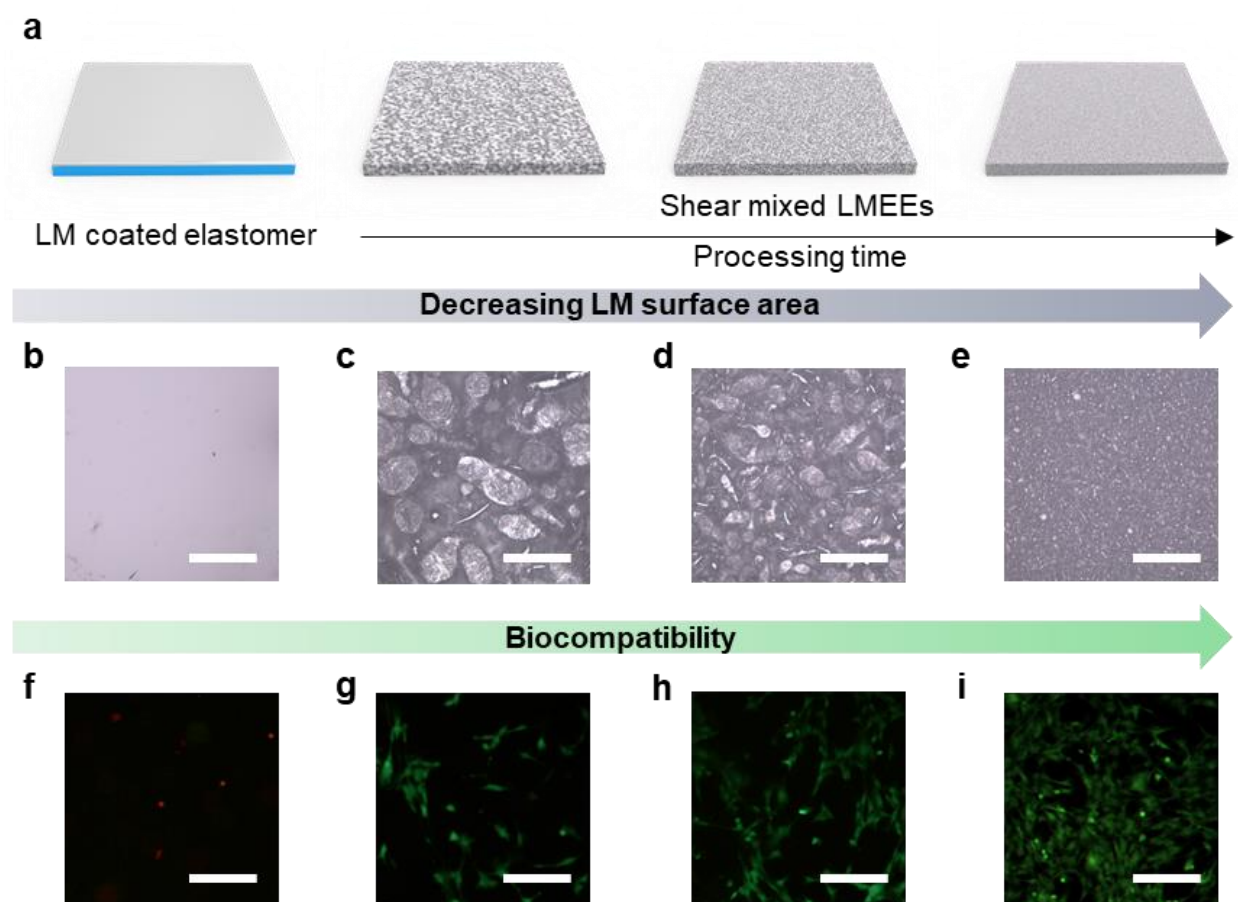
Figure 3.1 a) Illustration of decreasing trends in liquid metal (LM) surface by processing time of shear mixing LMEE, LM coated PDMS and shear mixed LMEEs for 30 s, 1 min and 10 min. b-e) Corresponding optical microscope (OM) images of LM surfaces. g-j) Biocompatibility visualized by florescence microscope images of C2C12 skeletal muscles grown on top the of different LM electrodes. (scale bars are 200 μm)

Results & Discussion

Liquid Metal Surface Area and Cell Viability on LMEE

Liquid metal embedded elastomers (LMEE) were characterized to find the volume ratio and processing time to optimize cell viability of the biohybrid actuator. There is a direct correlation between cell viability and liquid metal (LM) surface area when cells are cultured on a LMEE surface (Figure 3.1). The LM surface area decreases with the integration of EGaIn in to precured polymers which is primarily facilitated by processing (mixing) time. SEM images of the surface of

LMEE shows that as processing time increased, the LM surface area decreased considerably (Figure 3.2 a-d). This is likely because as processing time increases, EGaIn becomes more integrated and diffuse throughout the polymer. Additionally, the release of cytotoxic ions at the surface of LMEE are expected to be lower with smaller EGaIn droplets due to lower liquid metal area at the surface and increased EGaIn confinement with in LMEE architecture. The increase in surface area of the biocompatible polymer and decrease in droplet size is directly corelated to any increase of biocompatibility of the LMEE (Figure 3.1b-j). It was found LM surface area was minimized after at least 10 minutes of mixing. Furthermore, processing times of at least 10 minutes minimalized LM surface area on the outside of the LMEE irrespective of volume ratio differences. Although, there were considerable differences in total EGaIn between 50 %, 60 %, and 70% volume concentrations, LM surface area percentages were all equal after at least 10-minute processing times (Figure 3.2 e-h). LM volume concentrations above 70% were not considered for experiments as there would not be enough PDMS to encapsulate EGaIn droplets and LM. This would comprise the integrity of LMEE structure and increase LM surface area on LMEE surface.
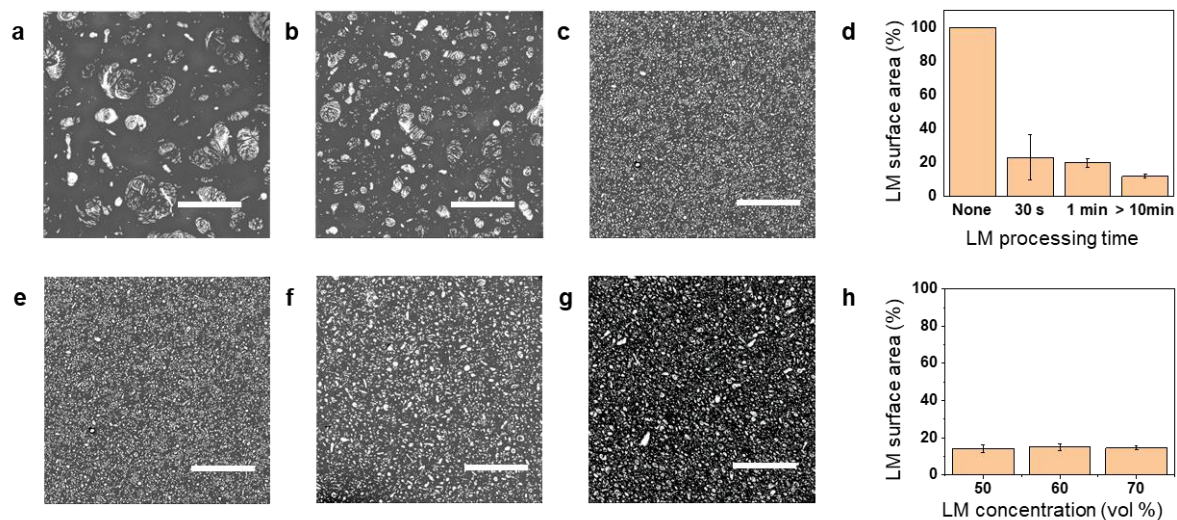
Figure 3.2 Conductive LM surface area measurement. a-c) scanning electron microscope (SEM) images of LM surface with different LM processing time a. 30s, b. 1 min and c. > 10 min. d) LM surface area measurement with different processing time. e-g) SEM images of LM surfaces with different LM volume concentrations. h) LM surface area measurement with different LM volume concentrations.
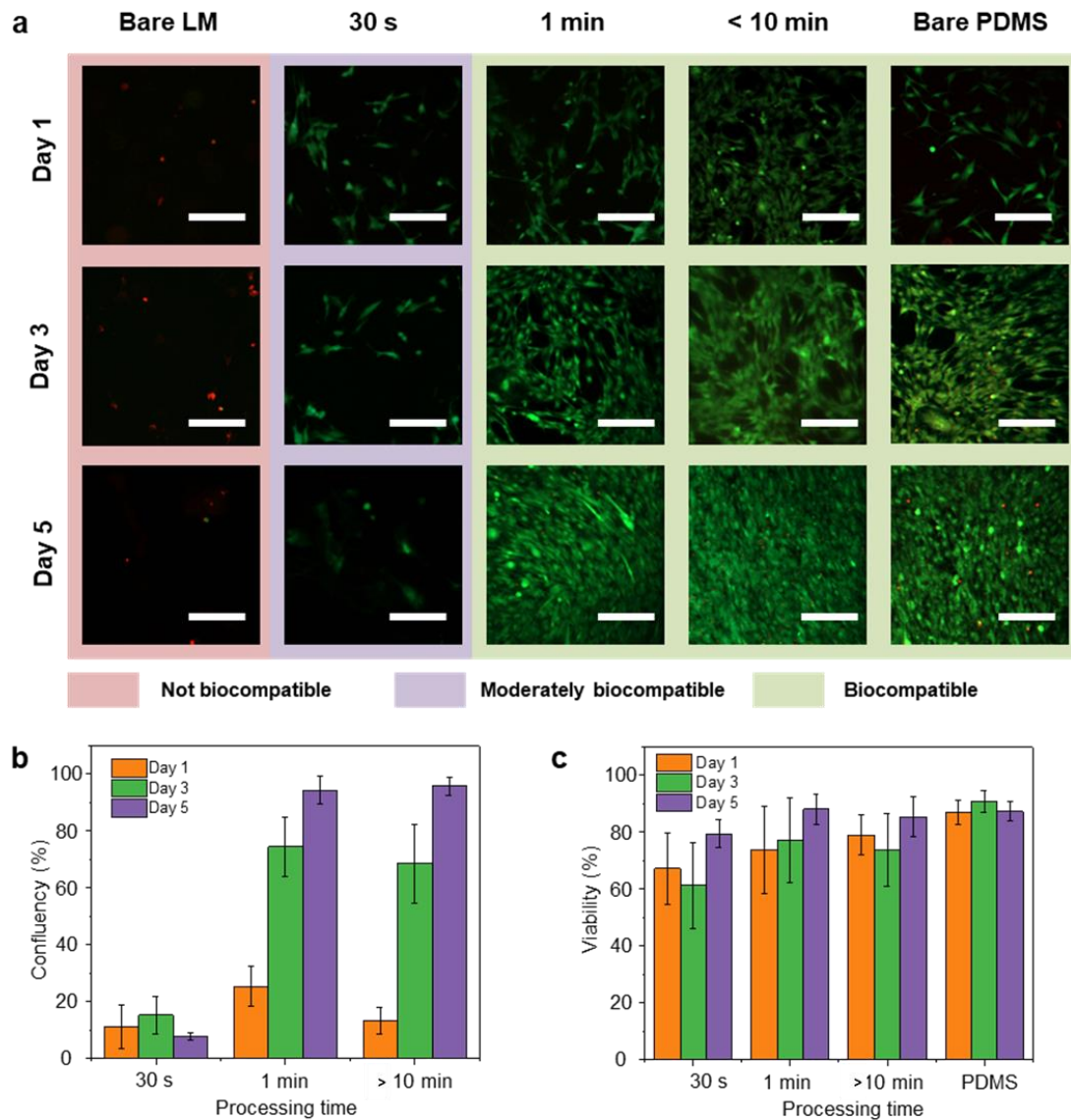
Figure 3.3 Biocompatibility test for LMEE depending on LM processing and integration. a) Fluorescence images on LMEE with different conditions; Bare LM on a PDMS substrate, LMEE with different shear mixing times and a bare PDMS substrate. b) Cell confluency after multi-day growth of C2C12, measured from day 1 to 5 days. c) cell viability on LMEE up to 5 days.
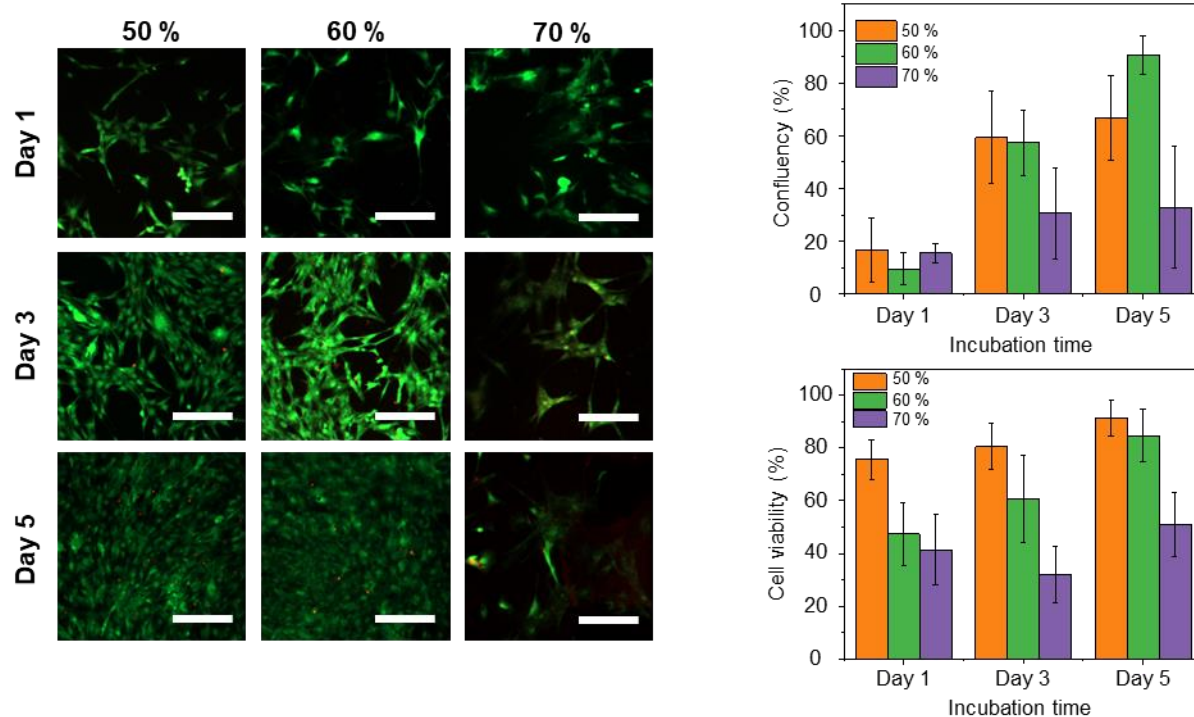
Figure 3.4 Biocompatibility test for LMEE depending on LM concentration (vol %). a) Fluorescence images of cells on LMEE with different conditions: 50%, 60% and 70% volume ratios. b) Cell confluency after multi-day growth of C2C12, measured from day 1 to 5 days. c) cell viability on LMEE up to 5 days. scale bar 200 μm.

Cell Viability and Confluency on LMEE

Cell viability and growth rate are important considerations when determining biocompatibility between cells and the material it is cultured on. When culturing cells on LMEE, it was found that processing times (Figure 3.3) and volume ratio of LMEE (50 %, 60% and 70%; Figure 3.4) were the most important considerations to promoting biocompatibility. It was found that there was substantially improved cell viability and growth rate on surfaces that had a processing time of 1 minute or longer. It was also found that there is an inverse relationship between the volume ratio of EGaIn to PDMS and cell viability and growth. LMEE volume ratio of 60% and process time of 10 minutes was used in biohybrid experiments because viability and growth rate were similar to PDMS. C2C12 cells were cultured for 5 days on EGaIn-PDMS LMEE at different percent volume

ratios (50 %, 60% and 70%) to compare cell confluency and viability. Cell viability improved between each day that cells were cultured. Although cells viability was highest at 50% LMEE volume ratio, conductivity was also lowest, which is not ideal for bio-hybrid actuation.

Cells can be cultured on LMEE surface after stretching (Figure 3.5). LMEE is activated after stretching (30% strain), because after stretching LMEE, EGaIn droplets rupture and connect to each other. After a rupturing, a lattice of connective EGaIn droplets is form activating the LMEE to be conductive. Chengfeng et al., compared the resistance of different volume ratios of LMEE that are activated and found at least 60% volume ratio of LMEE is necessary to achieve low resistances [127]. As a result, the volume ratio of 60% is optimal for biohybrid experiments due to the consistently high confluency achieved after 5 days of cell culture and high conductivity.

Another commonly used biocompatible polymer other than PDMS is ecoflex. Cells were cultured on ecoflex and EGaIn-ecoflex LMEE for 5 days to understand differences in viability and confluency (Figure 3.6). Although viability and confluency of cells cultured on ecoflex was consistently greater than that of EGaIn-ecoflex LMEE, cell viability and confluency were clearly high enough on the LMEE for potential biohybrid applications.
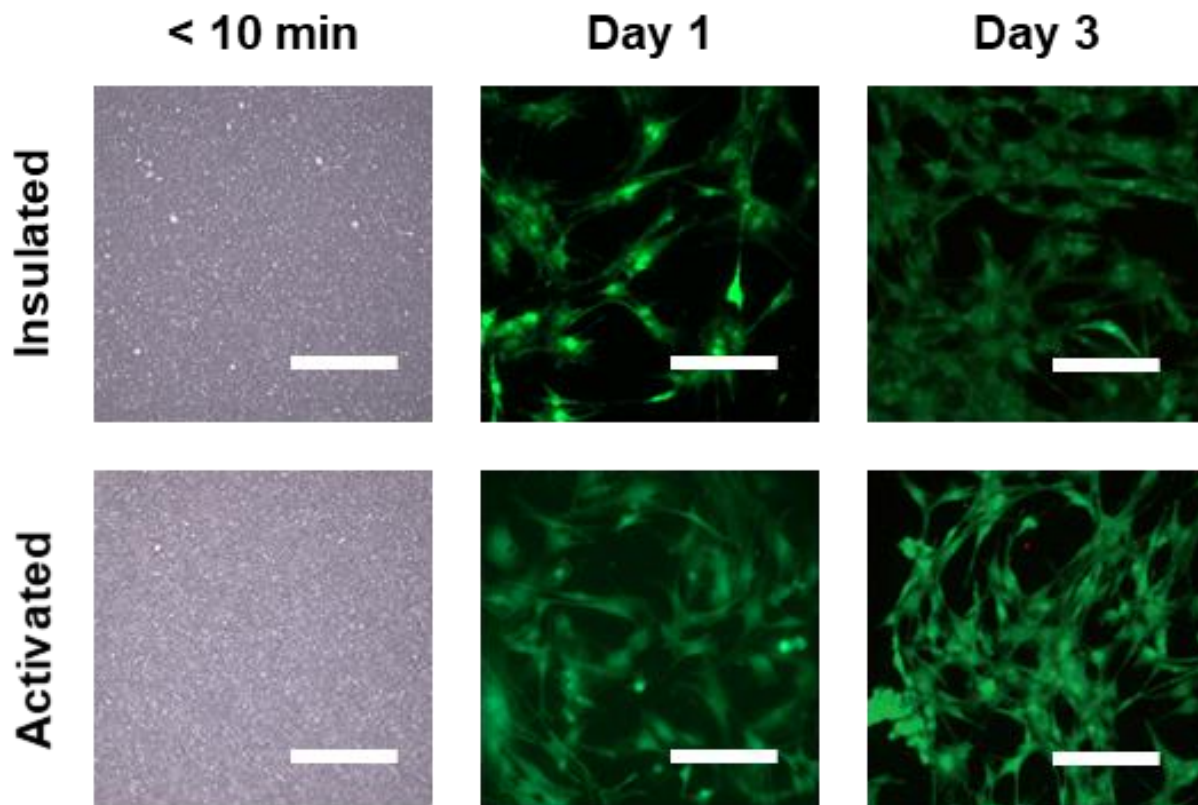
Figure 3.5 Comparison of insulated and activated LMEE for biocompatibility. Scale bar 200 μm.

EGaIn Polyurethane Nanofibers

Polyurethane nanofibers (PU NF) are a biocompatible material that when layered together creates a thin, stretchable, compliant material that is used in epidermal electronics. Instead of copper wires which are stiff, not complaint, and yields under low strain, EGaIn can be used as alternative wiring. Liquid metals due to their conductive and rheological properties, maintain the native elastic properties of PU NF. To understand the cytotoxicity of EGaIn, cells were cultured on the EGaIn PU NF and PU NF surfaces. The PU NF fibers are primarily empty space. When EGaIn is doped into the PU NF, the material primarily consists of EGaIn. Therefore, cells are cultured primarily on EGaIn when on EGaIn PU NF rather than PU NF. The viability of cells on PU NF was 95% and the viability on EGaIn PU NF was 0% (Figure 3.7). Although cells did not survive on the

surface of the EGaIn PU NF, high viability was retained of peripheral cells within the same petri dish that were not in direct contact with EGaIn. EGaIn's inability to support cell adhesion was found to be mitigated by reducing direct contract between the liquid metal and cells.
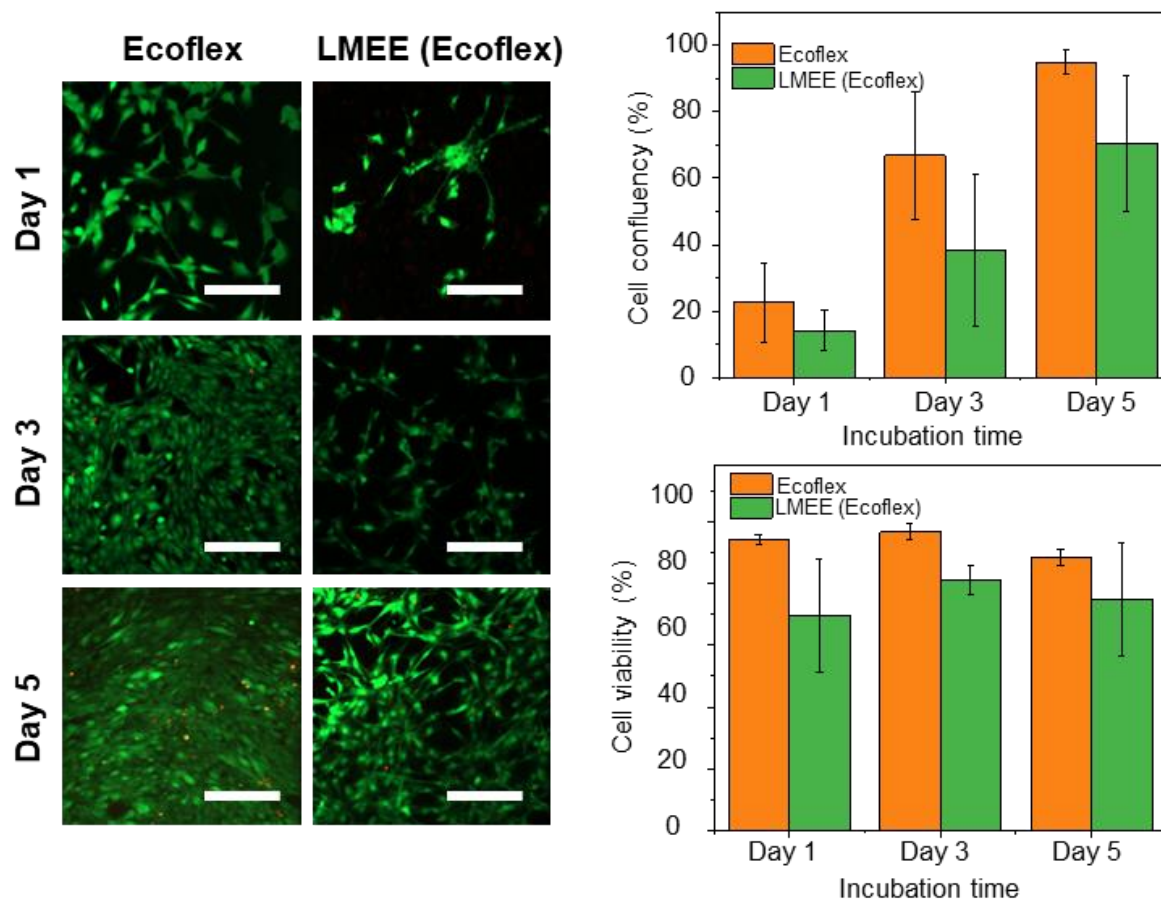
Figure 3.6 Biocompatibility test for ecoflex and EGaIn-ecoflex LMEE. a) Fluorescence images of cells on ecoflex or EGaIn-ecoflex LMEE. b) Cell confluency after multi-day growth of C2C12, measured from day 1 to 5 days. c) cell viability on EGaIn-ecoflex LMEE up to 5 days. scale bar 200 μm.
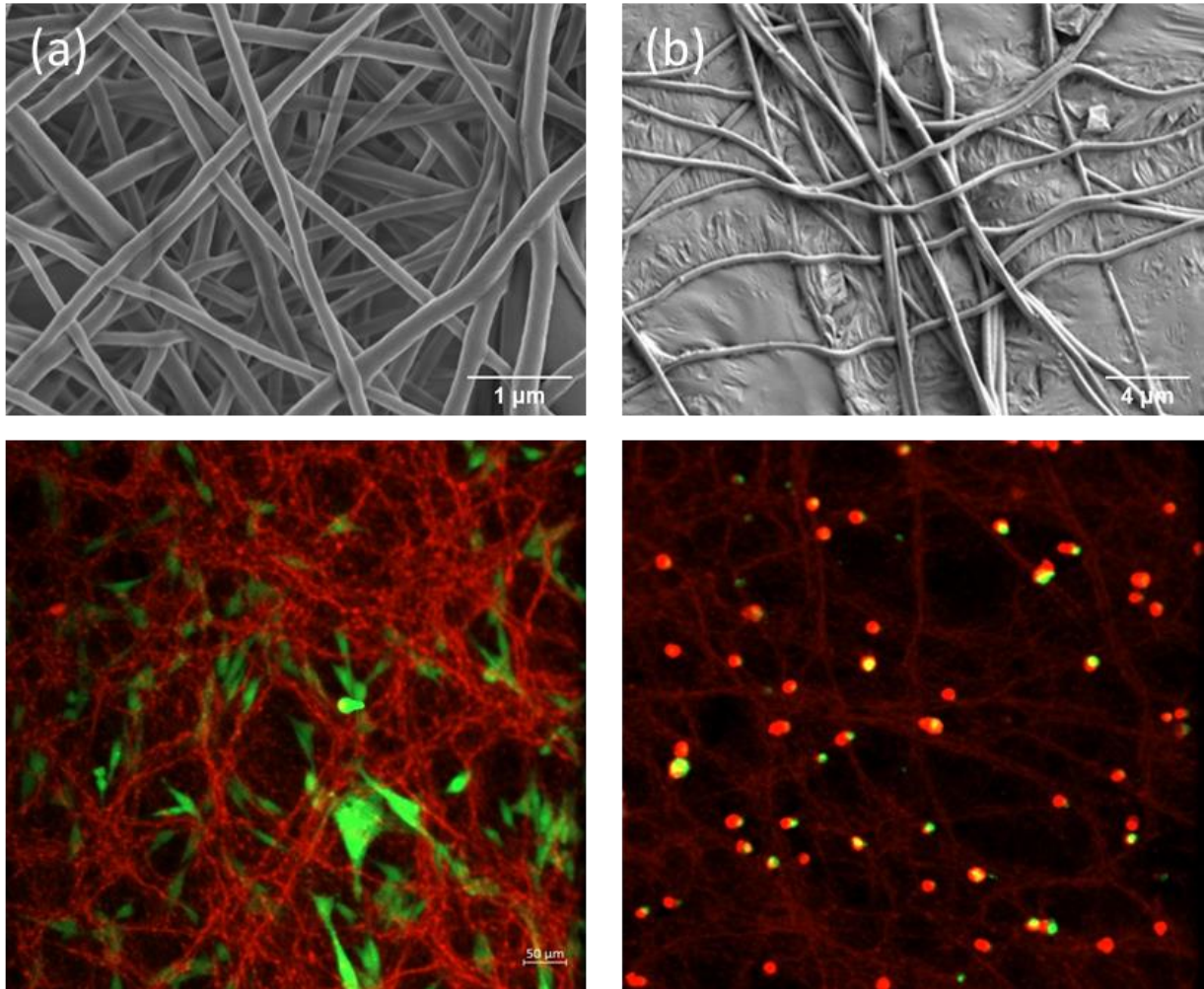
Figure 3.7 SEM images of Polyurethane Nanofibers (PU NF) (top left) and EGaIn PU NF (top right). C2C12 cells viability was on PU NF mesh and were not viable on EGaIn PU NF mesh. The red lines in fluorescent images are stained PU NF.

Characterization of LMEE

The material properties of LMEE at different volume concentrations were compared to understand which properties would be ideal for a biohybrid actuator. It was found that the stretchability of LMEE decreases with higher volumetric contents of LM (Figure 3.8). The moduli of each concentration are consistent within a range of 700 ~ 800 kPa at lower strain region (< 30 %). So for biohybrid experiments, the 60 % volume of LMEE would be utilized for the biohybrid device for its moderate stretchability, electrical conductivity, and biocompatibility.
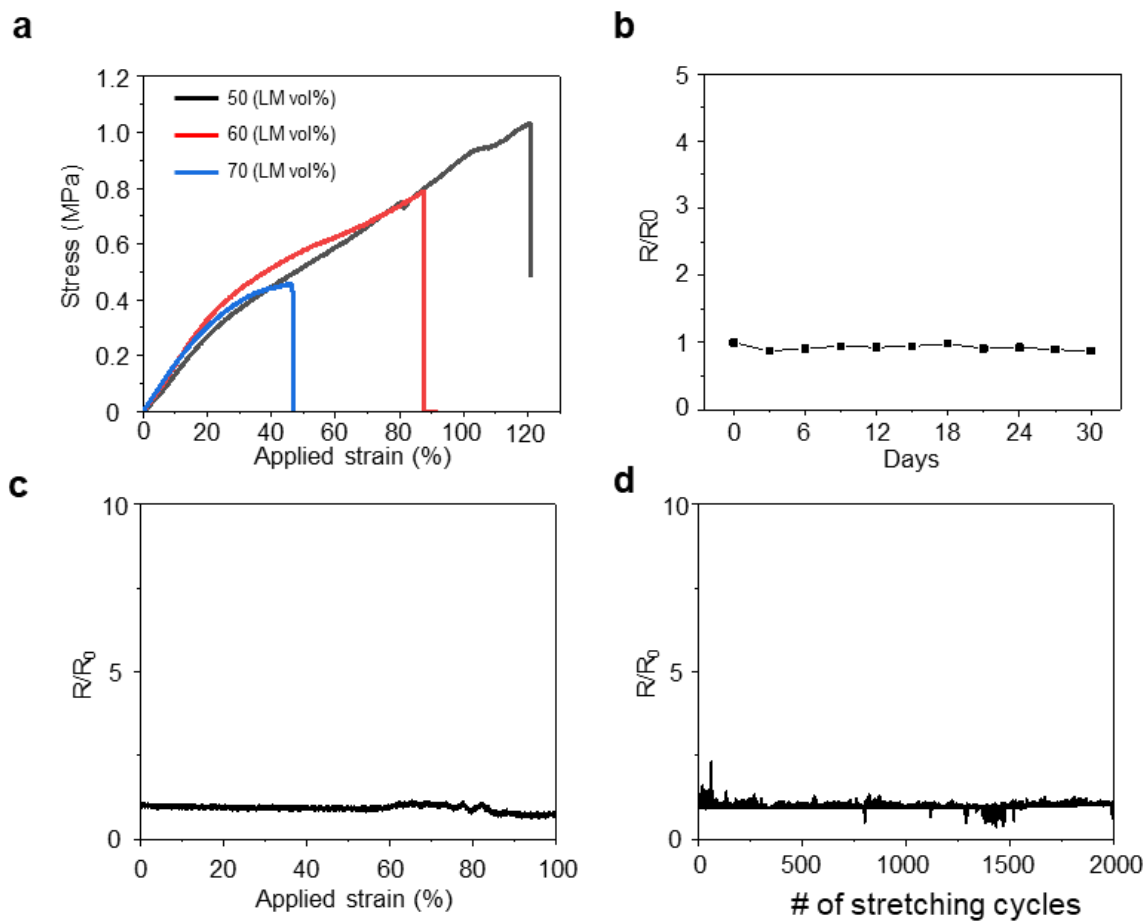
Figure 3.8 Characterization of LMEE electrodes. a) Stress-strain curves of LMEE with different LM concentrations, b) Oxidation stability test with the change in resistance over time in air. c-d) Electrical properties of LMEE under deformations, c) relative resistance under applied strains and d) relative resistance under cyclic stretching (strain of 50 %)(note that LM vol. fixed at 60 % for b-d).
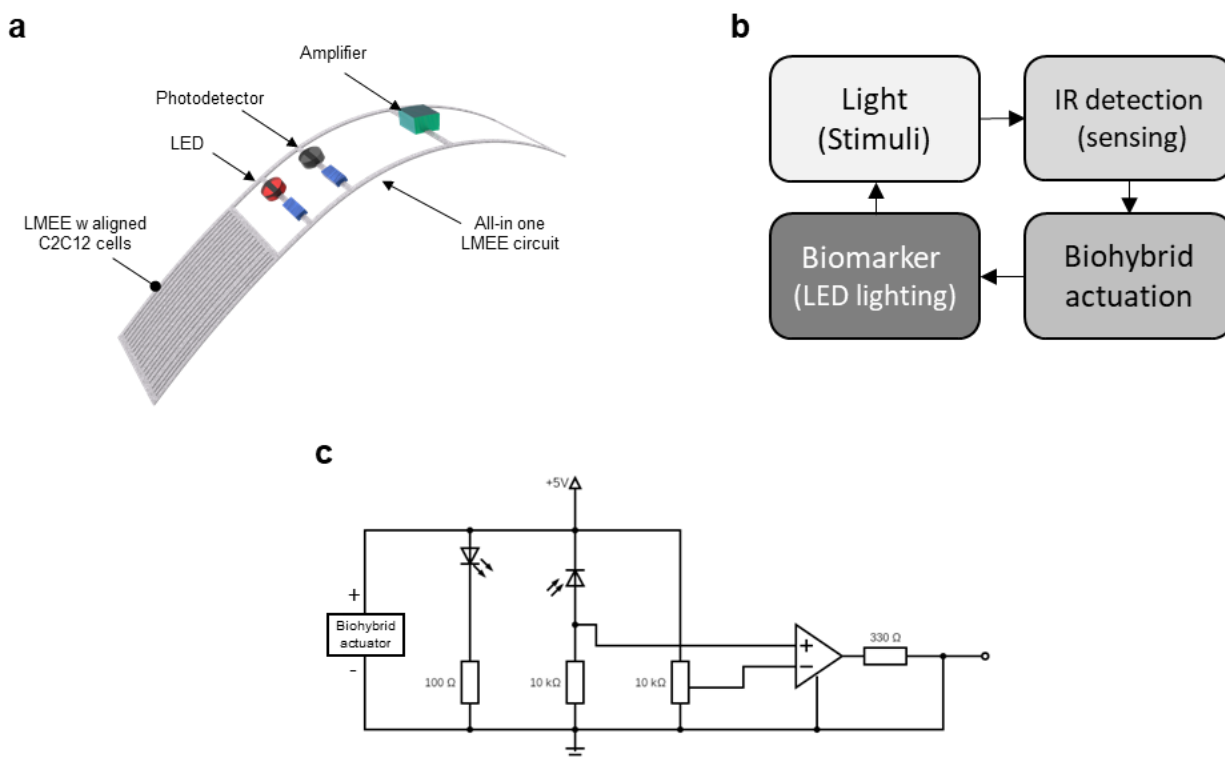
Figure 3.9 Demonstration of light responsive biohybrid actuator with integrated circuits.

Conclusions and Future Work

In this study, we investigated methods to improve the biocompatibility of EGaIn so that the material can be used in biohybrid systems. We conducted live dead assays of cells cultured on PU NF, EGaIn PU NF, PDMS, PDMS LMEE, and ecoflex LMEE. We found that viability of cells on PU NF was 95% and the viability on EGaIn PU NF was 0%. We then compared cell viability when cultured on LMEEs. The liquid metal EGaIn can interface with C2C12 cells when embedded into biocompatible elastomers such as PDMS and ecoflex. We found there is a direct correlation between cell viability and liquid metal (LM) surface area when cells are cultured on a LMEE surface. The LM surface area decreases with the integration of EGaIn in to precured polymers which is primarily facilitated by processing time. The maximum biocompatible volume ratio of

EGaIn to PDMS that can be achieved is 70% EGaIn. A combination of different experimental studies suggest that an LMEE volume ratio of 60% in PDMS-LMEE composite materials may be ideal for many biohybrid applications as this volume ratio yields an optimal balance of material failure strain, electrical conductivity and biocompatibility. With the requisite work done in characterizing the biocompatibility of LMEEs, future work to create a biohybrid actuator can be conducted (Figure 3.9). Due to the material properties of LMEEs, it can be used for both the circuit wires and scaffold material for cell culture.

Chapter 4 Cell Sheet Stacking for Co-Culture Model

Introduction

Within the field of tissue engineering, vascularization of tissues is one of the most critical challenges. Fabricated 3D tissue engineered constructs that most closely emulate *in vivo* tissue consists of a multi-culture of cells that are aligned and vascularized with lumen formation. Without cell alignment, the tissue does not emulate in vivo conditions and without vascularization the tissue will be unable to receive oxygen and nutrients. There have been many promising studies that have investigated techniques to vascularize engineered tissue, but further work is needed to understand the mechanisms that facilitate cell self-organization in 3D engineered constructs [128]. The focus of this study is to develop a cell sheet stacking protocol to develop a co-culture model to investigate the mechanisms that promote self-organization of blood vessels *in vivo* conditions.

Blood vessels can be divided into 3 tissue layers that are primarily composed of two cell types: endothelial and vascular smooth muscle cells (Figure 4.1) [129]. The tunica intima is the innermost layer and is the thinnest, consisting of a monolayer of endothelium supported by a subendothelial layer, called the internal elastic membrane. The tunica media is the middle layer that is much thicker and consisting of elastic fibers, connective tissue, and smooth muscle cells that are organized orthogonally to the monolayer of endothelial cells in the intima layer. The tunica externa is the outermost layer that is thick and entirely composed of connective fibers.

Healthy maintenance of the structure and morphology of each blood vessel layer is mediated via competing mechanical, chemical, and physiological factors. It is well understood

that mechanical interactions via laminar shear forces from blood flow stimulates cellular responses essential for endothelial function and morphology. Endothelial cells exposed to shear stress undergo reorientation, with their longitudinal axis parallel to the direction of blood flow. Exercise, which promotes blood flow and positive shear stress, stimulates endothelial cell responses providing mechanisms by which a healthy structure of blood vessel layers is maintained [130]. Alternatively, a sedentary lifestyle, provides low mean shear stress, inducing inflammation of endothelium and promoting risk factors such as hypertension, diabetes, and hypercholesterolemia [131]. One method the body modulates mean shear stress is by changing the diameter of the blood vessel via vascular tone, which is the degree of constriction or dilation of a blood vessel. Smooth muscle cells, which are organized orthogonally to the direction of blood flow, mediates vascular tone by modulating how much contraction is applied to the blood vessel. The proximity of endothelial and smooth muscle cells makes signaling via secreted or diffusible factors an efficient mechanism of communication in vascular tone. Endothelial-derived factors, such as nitric oxide, prostacyclin, and hyperpolarizing agents diffuse to smooth muscle cells to cause vasodilation. Endothelin and angiotensin II cause vasoconstriction [132]. Mechanotransduction via vessel wall shear stresses and cell signaling pathways between endothelial and smooth muscle cells are essential to the recruitment, survival, and differentiation/maturation of blood vessel layers [132, 133].

To better understand how vascular functions and layer structure is mediated by shear stresses and cell-cell interactions, several co-culture vascular wall models have been developed [134]. There are two major models of *in vivo* conditions between endothelial and vascular smooth muscle cells under hemodynamic conditions: (1) endothelial and smooth muscle cells cultured

on opposite sides of a porous membrane [135, 136] and (2) endothelial cells cultured directly on a confluent layer of smooth muscle cells [137, 138, 139, 140]. The porous membrane in vascular models emulates the elastic membrane between endothelial and smooth muscle cells. This more closely models coronary arteries whose elastic membranes are thicker than other parts of the body. Alternatively, vascular models of endothelial cells cultured on confluent layers better emulate arterioles whose elastic membranes are much thinner than other blood vessels [134, 141]. In this study, we investigate a method to stack monolayers of cells on top of each other in order create biohybrid thickness for potential applications in modeling *in vivo* hemodynamic conditions.

Cell sheet stacking is a technique in tissue engineering that involves culturing 2D sheets of cells, harvesting these sheets, and stacking each sheet of cells to fabricate 3D tissue [142, 143, 144, 145]. Cell sheets are typically cultured on Glass, TCPS, or PDMS grafted with the temperature responsive polymer, poly(N-isopropylacrylamide) (PIPAAm) [146, 147]. PIPAAm is grafted onto these materials using UV or EB radiation [147]. Surfaces grafted with PIPAAm are considered to be intelligent surfaces because they can alter wettability between hydrophilic and hydrophobic properties with changes in temperature from 37 °C to 20 °C (Figure 4.2, 4.3) [148]. The change in temperature from 37 °C to 20 °C modulates, respectively, the attachment to detachment of cells culture on PIPAAm [149, 150]. When cell sheets are detaching from PIPAAm grafted surfaces at 20 °C, the cell sheets are harvested and stacked into 3D tissue using a plunger device (Figure 4.4) [151].

This aim of this study to stack pre-aligned monolayers of cells to develop a co-culture model has three novel advantages. First, cells can be aligned with each cell sheet before stacking

into 3D tissue. This allows for control over the exact orientation of each layer of cells relative to each subsequent layer. Second, different cell lines can be cultured independently before combining into a co-culture. This ensures a homogenous, conformal monolayer of endothelial cultured on top of smooth muscle cells. This is different from typical vascular models where endothelial cells are cultured directly on top of smooth muscle cells. Third, cell sheet stacking is a convenient method for modular control of which layers are pre-aligned and which layers are not. This tests how cells in the co-culture will reorientation under shear stress in varying layer configurations.

Materials and Methods
PIPAAm-PDMS Graft Polymerization

UV-induced graft polymerization onto PDMS was implemented according to previous protocols [152, 153, 154]. PDMS was soaked in benzophenone (20 wt. % in acetone) for 10 minutes (Sigma Aldrich). The PDMS was thoroughly washed in DI water to rinse an unabsorbed benzophenone from the surface. The PDMS was placed in a solution containing NIPAAm (10% in ultrapure water), $NaIO_4$ (0.5mM), and benzyl alcohol (0.5 wt.%) (Sigma Aldrich), which was then irradiated with UV light (IntelliRay 600W Flood Curing) at 210W for 20 minutes. Throughout UV exposure, the PDMS was kept under the LCST of PIPAAm by cooling with ice water. The ice water mitigated heating from UV which would result in the phase transition and aggregation of PIPAAm polymer chains [155]. The PIPAAm-grafted PDMS was thoroughly rinsed in ethanol and water to remove excess monomer. Surface roughness PIPAAm-PDMS of different grafting times was characterized using the Zygo new view 7300 (Figure 4.5).
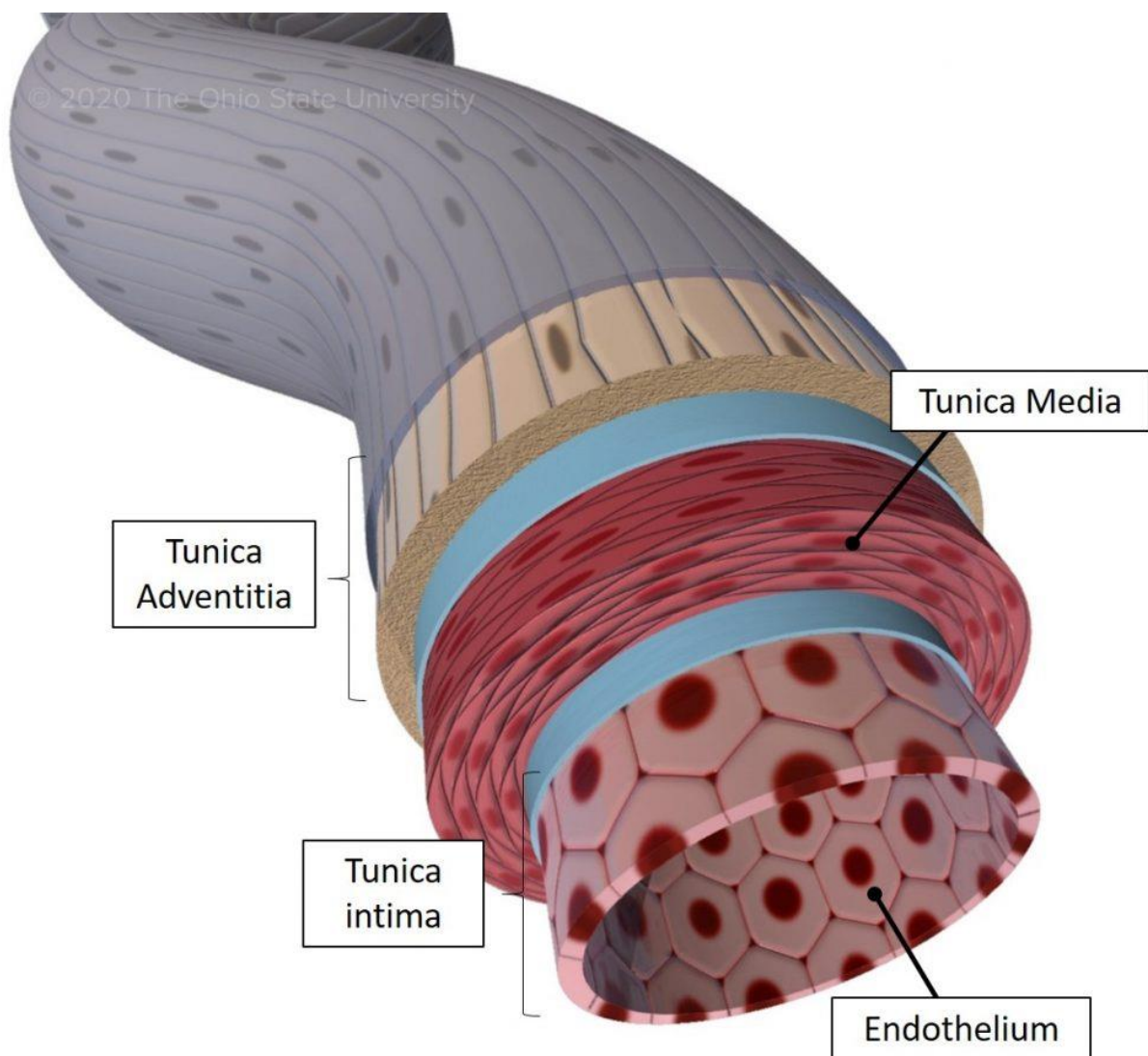
Figure 4.1 Model of vasculature. With the exception of capillaries and sinusoids, all larger vessels have the same three basic structural elements (tunics). These are the tunica intima (inner or luminal layer), tunica media (middle layer), and tunica adventitia (outer layer). Depending on the level of the vasculature, there are marked differences in the tunic width. (Image by Jennings et al. [129])

PIPAAm-co-Acrylamide Grafted onto TCPS

UV-induced graft polymerization onto TCPS was implemented according to previous protocols

[156, 157]. N-Isopropylacrylamide (NIAM), Acrylamide (AM), N,N'-Methylenebisacrylamide

(MBAM) and potassium periodate (KIO$_4$) were all purchased from Sigma-Aldrich. Tissue culture

polystyrene (TCPS) dishes, each 35 × 10 mm^2 (Thermofisher), were used without any further

treatment. The vacuum desiccator used had UV film to protect the samples for long term storage (SP Bel-Art Lab, F42400-2141).

A TCPS dish was submitted to an oxidation process by using a UV lamp (UVGL-58, 6 W, and 254 nm) for 30 min. After oxidation, an aqueous solution of 50 µL containing NIAM (1 mol L^{-1}), AM (1.04 mol L^{-1}), cross-linker MBAM (0.02 mol L^{-1}), and photoinitiator KIO_4 (0.005 mol L^{-1}) were added to each TCPS dish. A spin coater (Laurell Model WS-400-6NPP/LITE) was used to spread the solution uniformly on the surface using a spin speed of 1500 rpm for 5 min. The dishes were immediately exposed to UV for 2 h. The poly(N-isopropylacrylamide)-co-Acrylamide (PIPAAm-co-AM) grafted TCPS dishes were kept at room temperature under vacuum for 24 h to allow for remaining monomers to polymerize. After 24 hours under vacuum the samples were washed with ethanol three times to remove the unreacted monomers. Samples were dried with compressed N_2 gas and stored under vacuum until use. Samples were used within one month of polymerization.
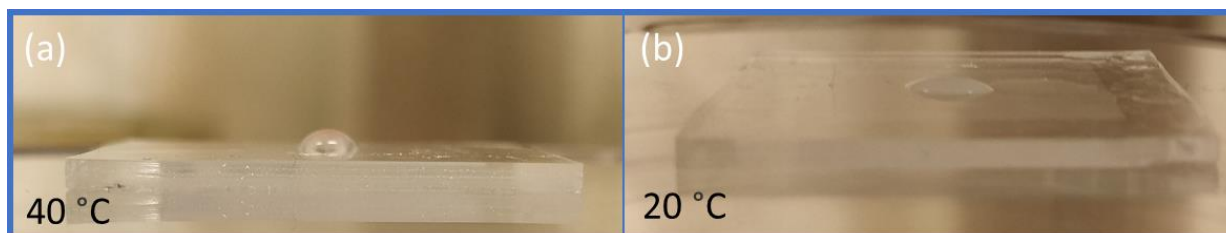
Figure 4.2 Contact angle of 20 µl of water on PIPAAm-grafted PDMS surfaces at 40 °C (a) and 20 °C (b).
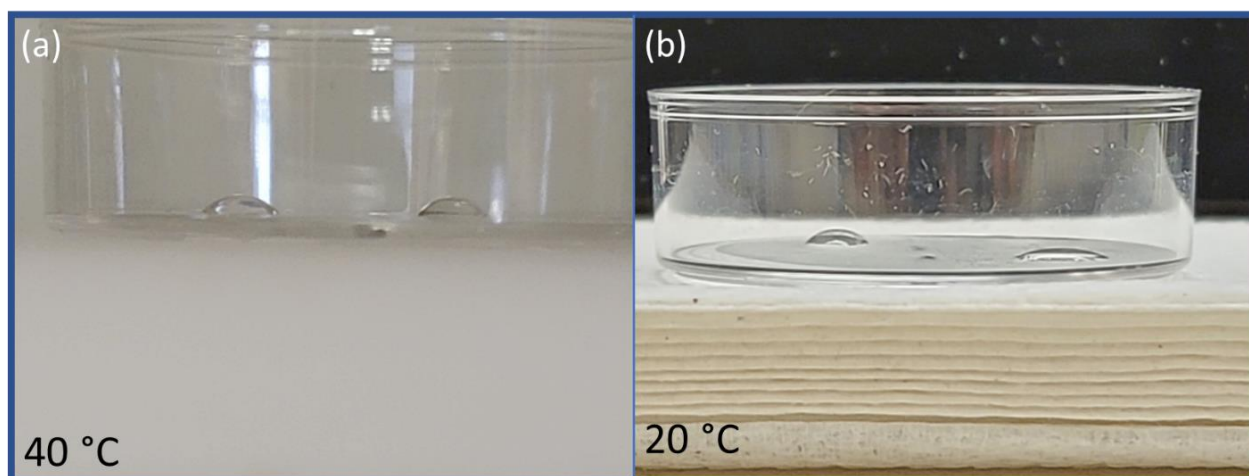
Figure 4.3 One half (right) of the TCPS was grafted with PIPAAm-co-AM. Contact angle of 20 µl of water on grafted verse non grafted side of TCPS surface was compared at 40 °C (a) and 20 °C (b).

Cell Sheet Manipulator

Cell sheets are placed on top of each other using a cell sheet manipulator (Figure 4.3). The cell sheet manipulator has two purposes: (1) to prevent cell monolayers from folding in on itself during cells sheet release and (2) to transport and stack monolayers of cells onto each other. The device is designed according to previous studies [151]. Cell sheet manipulator device consists of 4 components: plunger, plunger guide, hydrogel mold, and a porcine hydrogel layer. The plunger, plunger guide, and hydrogel mold were 3D printed using the FormLabs Form 2 printer. The porcine hydrogel layer (7.5 wt.%) was formed by first mixing porcine gelatin powder and DI water with a spinner at 450 RPM for 15 minutes. Once gelatin was dissolved the mixture was heated at 40 °C for 20 minutes. The gelatin was poured into the hydrogel mold and the plunger was placed on top of the mold and hydrogel. The manipulator was placed into a refrigerator for 12 hours to stiffen the hydrogel. Due to grooves in the base of the plunger, the hydrogel bonded to the plunger device. The thickness of the hydrogel layer used for cell sheet manipulation was 1.5 mm thick. The plunger with hydrogel layer combined with the plunger base was used to manipulate and stack cell sheet layers.

Hydrophobicity Test

Hydrophobicity tests were conducted on PIPAAm grafted on to PDMS and TCPS to evaluate the thermally bistable properties of PIPAAm. For each material they were first heated on a heat pad at 40 °C then 20 µl of water was added to the surface. To test hydrophobicity at lower temperatures, the samples were allowed to cool to room temperature then 20 µl of water was added to the surface. The difference in water droplet curvature was compared at each temperature.
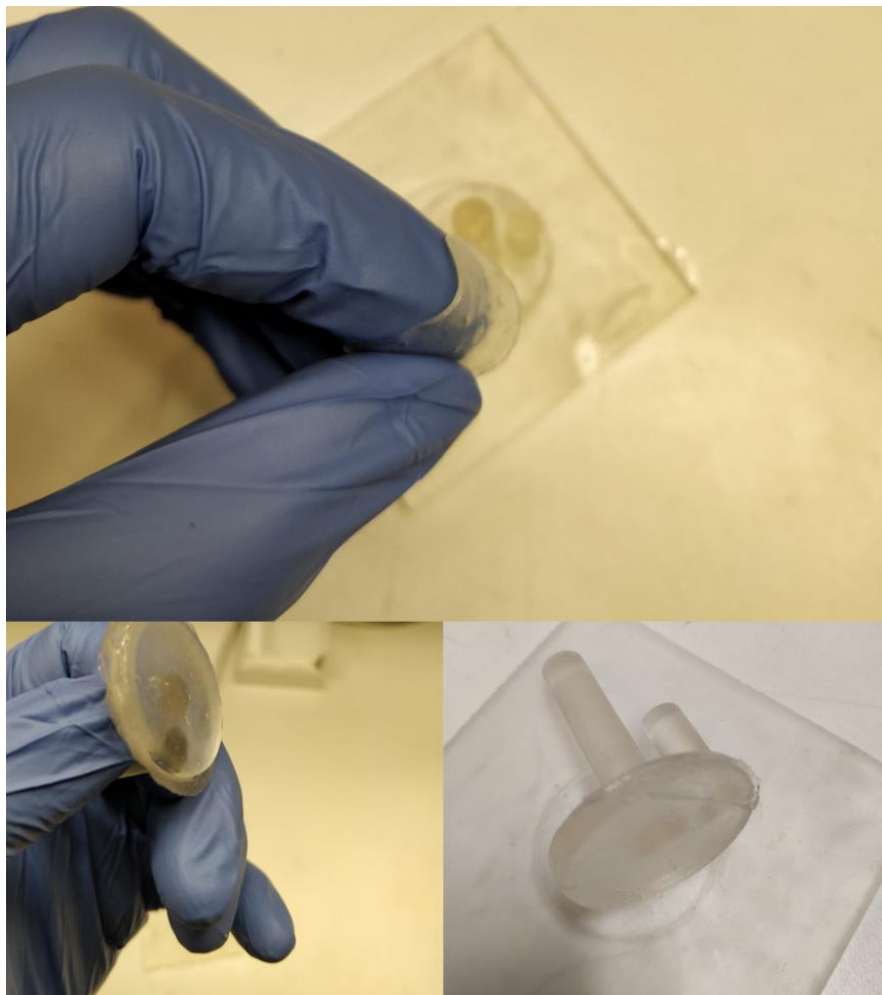
Figure 4.4 Cell sheet manipulator device consists of 4 components: plunger, plunger guide, hydrogel mold, and hydrogel layer.
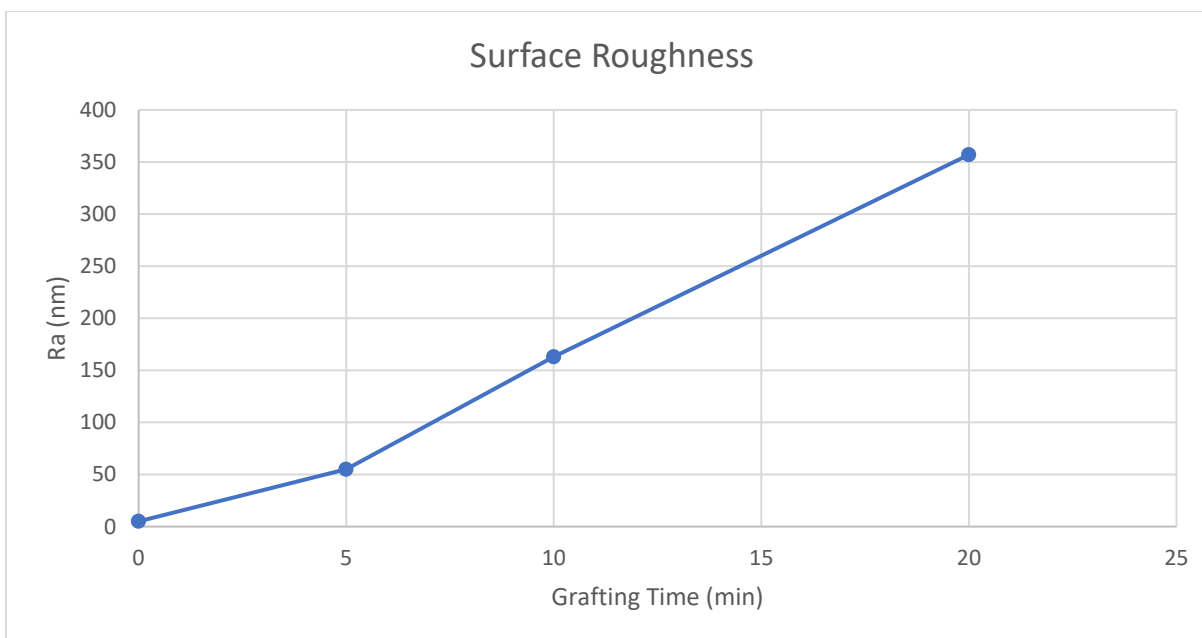
Figure 4.5 Surface roughness of 10 wt % NIPAAm grafted onto PDMS at different times was characterized using the Zygo new view 7300.

Materials and Methods for Future Work

Cell Culture

Vascular smooth muscle cells (VSMC; ATCC HCASMC) were cultured between passage 2 to 7.

VSMC were cultured in Vascular Cell Basal Medium (ATCC® PCS-100-030), 1% Penicillin-Streptomycin-Amphotericin B Solution (ATCC PCS-999-002), 1% Phenol Red (ATCC® PCS-999-001), and Vascular Smooth Muscle Cell Growth Kit (ATCC PCS-100-042). HUVEC cells (ATCC CRL-1730) were grown to confluency in growth media medium of F-12K Medium (ATCC 30-2004), 10% FBS (ATCC 20-2020), 0.1 mg/mL heparin, and 30 µg/mL Endothelial Cell Growth Supplement.

Cell Sheet Stacking

VSMC and endothelial cells were cultured on a fibronectin patterned PIPAAm-co-AM grafted TCPS and incubated until 100% confluency. The hydrogel-coated plunger was placed on the surface of the endothelial cell layer with the plunger-guiding cover, and the cells with the plunger was incubated at 20 °C for harvesting. Then, the endothelial cell layer was harvested with the

hydrogel and transferred onto the confluent VSMC monolayer in another petri dish. After that, the petri dish with the plunger was incubated at 37 °C for 20 min, promoting adhesion between two cell layers. The incubation for promoting stable adhesion between two cell layers at 37 °C causes the hydrogel to melt and release the top cell sheet from the plunger device. When stacking more than one layer of cell sheets, stable adhesion between two cell layers will be performed at 20 °C for 30–50 min to avoid the melting of porcine hydrogel at 37 °C before harvesting. The co-cultured 3D tissue was kept in a mixture of the VSMC and HUVEC medium (5:1 or 1:1).

Cell Alignment

The alignment of muscle tissue microstructure relative to the film shape was critical to optimizing muscle cell contractility (Figure 4.6c, d). There are two potential approaches that will be taken to align cells on PIPAAm grafted surfaces, namely surface topologies or chemical gradients [158, 159, 160, 161]. Initial design considerations involved introducing wavy topologies on PDMS for cell alignment along the direction of pattern (Figure 4.6a, b). Surface topologies on PDMS were fabricated by casting commercially available holographic diffraction gratings from Edmund Optics.

Alternatively, fibronectin patterns on the top of PIPAAm grafted surfaces can induce uniaxial cell alignment. Once cells are seeded onto the fibronectin, the fibronectin pattern determines the future positions of daughter cells and therefore informs self-organization of cell culture. To optimize alignment of VSMC and endothelial cells, several different fibronectin (FN) stamp patterns were fabricated (Figure 4.6e) to imprint FN stamps onto the target thermo-responsive surfaces. The spacing widths of the FN stamps and cell culture on FN-PIPAAm

patterned surfaces were informed by previous studies [162, 163, 164]. Using a PDMS stamp, a

FN pattern is applied to the top surface. For sterilization, PDMS stamps were sonicated in 100%

ethanol for 5 minutes. For patterning, stamp designs were incubated with FN at 50 µg/ml in DI

water for 1 h. The FN-coated PDMS stamps were brought into conformal contact with the target

substrates for 10 min to create the FN micropatterns. Cells are seeded at near-confluent density

onto FN-PIPAAm substrate with serum-free media (complete media without FBS). This allows

cells to attach and align primarily to FN regions overnight. The next day serum free media is

removed and replaced with complete media until cell sheet release. Cells proliferate and fill in

regions without fibronectin while still maintaining cell alignment.
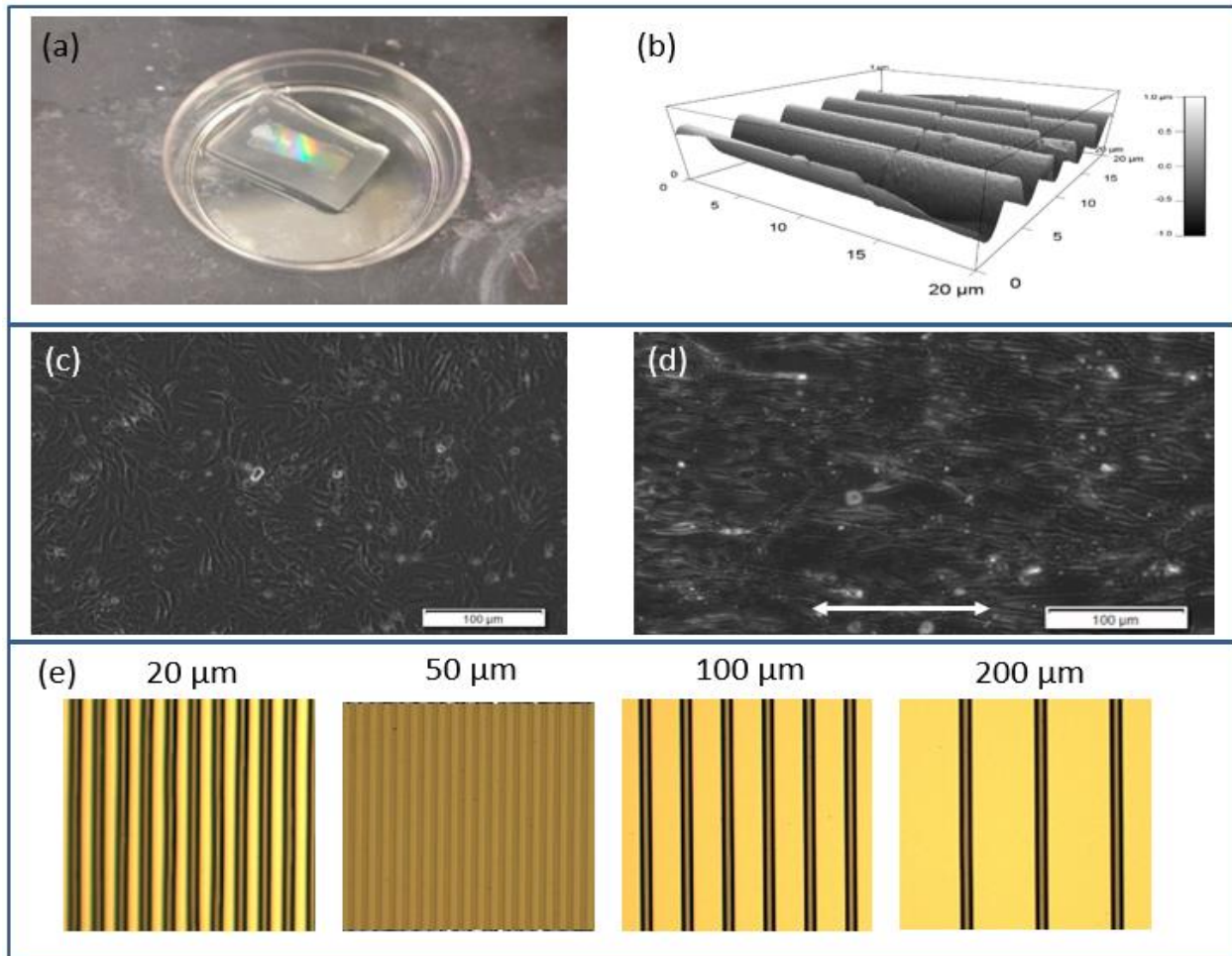
Figure 4.6 (a) PDMS patterned with wavy sinusoidal topology to induce cell alignment, (b) AFM of PDMS surface, (c) Unorganized C2C12 cells seeded on bare PDMS, (d) Well aligned C2C12 cells seeded on wavy, (e) SU-8 mold for PDMS FN stamp. The dark yellow regions are valleys if the SU-8 mold. The FN stamp design has varying widths (20 μm, 50 μm, 100 μm, and 200 μm) each spaced by 20 μm.

Shear Flow System

VSMC-endothelial coculture was subjected to elevated levels of shear stress (0-20 dyne/cm^2).

The design of the system that emulates blood flow was informed from previous studies (Figure

4.7) [165]. Co-culture medium is pumped through a parallel plate flow chamber over a Petri dish

of VSMC-endothelial coculture. Flow rate is monitored using a flow probe. Cell media were

oxygenated in 5% CO_2.
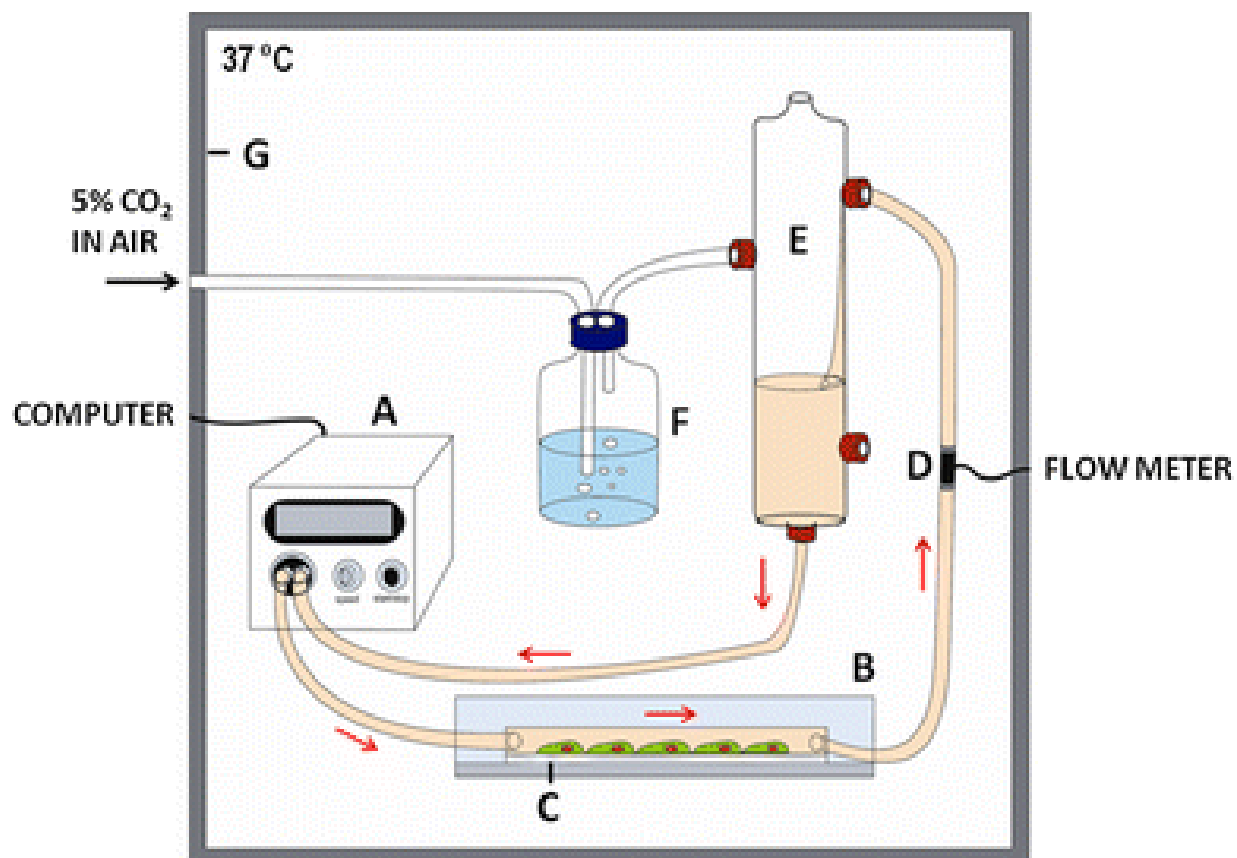
Figure 4.7 Co-culture medium is pumped through though a parallel plate flow chamber over a petri dish of VSMC-endothelial coculture. Flow rate is monitored using a flow probe. Cell media is oxygenated in 5% CO2 in air. (Image by Juffer et al. [165])
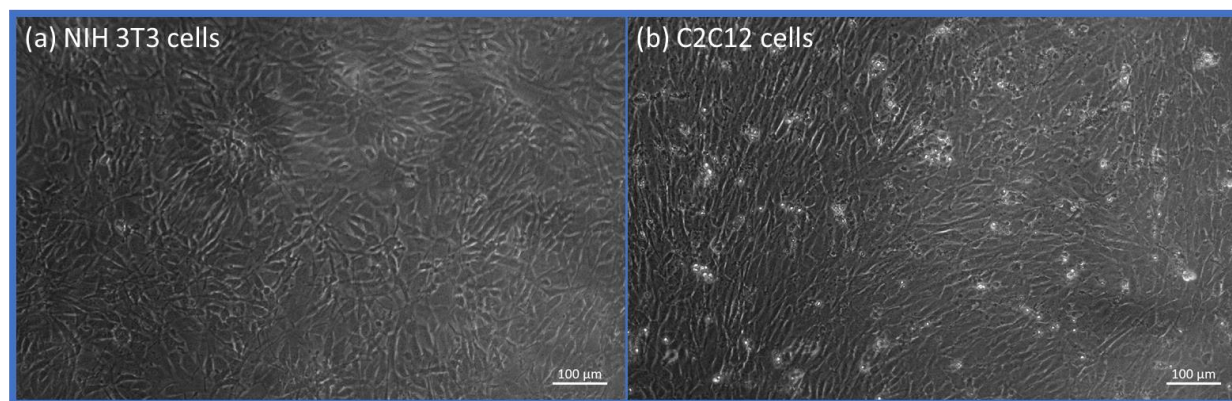
Figure 4.8 Cells cultured on TCPS with PIPAAm-co-AM grafted surface. NIH 3T3 (a) and C2C12 cells (b) are viable on the surface.
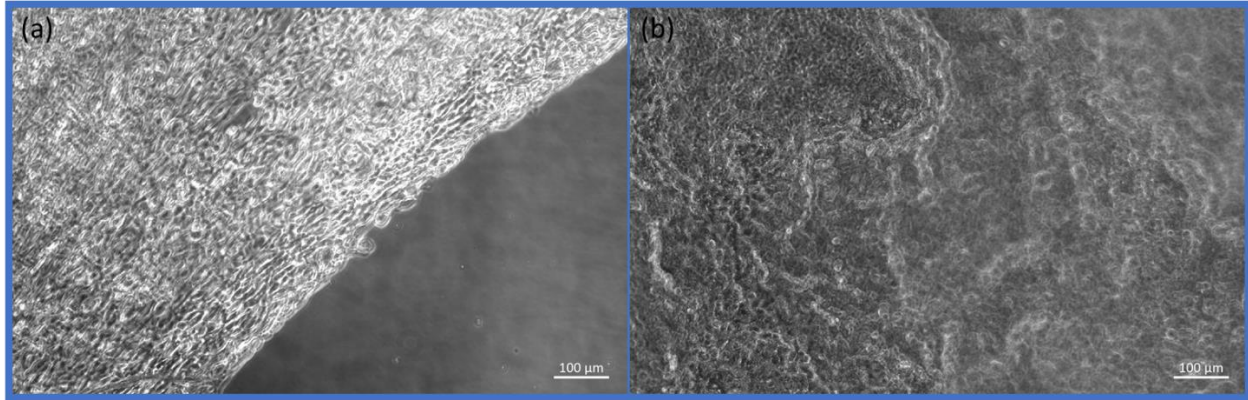
Figure 4.9 NIH 3T3 cells release from PIPAAm-co-AM surface when temperature is lowered to 20 ° C. Cell-cell connections maintain the cell sheet as cells pull away from the surface(a). Cell sheet as it is floating in TCPS dish (b).
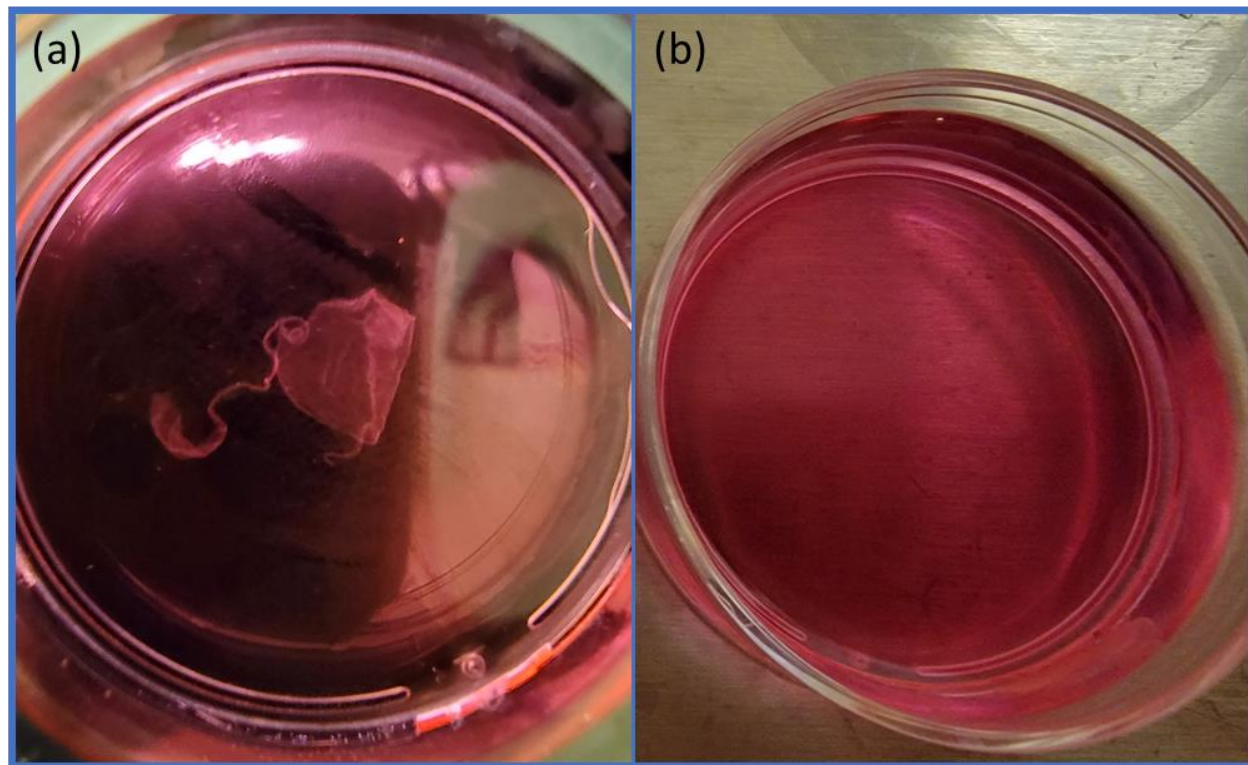
Figure 4.10 Cells sheet release of NIH 3T3 cells (a) and C2C12 cells (b) at 20 ° C. NIH 3T3 cells successfully released from PIPAAm-co-AM grafted surface, while C2C12 cells did not successfully detach from surface.

Results and Discussion

Cell Sheet Detachment

PIPAAm-PDMS was initially considered for a scaffold for cell sheet release. PDMS was an ideal

scaffold material because it can be surface patterned to promote cell alignment. In addition,

grafting PIPAAm on to the surface can promote cell detachment when the temperature is lowered to 20 °C. Although we were successful in altering PIPAAm-PDMS wettability between hydrophilic and hydrophobic properties with changes in temperature from 20 °C to 37 °C (figure 4.2,4.3), cell viability was not consistent when culturing onto its surface. This is likely due to the cell type not being conducive to cell sheet release or poor grafting on to PDMS. The cell type may have an important role due to the type of ECM that they produce. Between PIPAAm and cultured cells is a thin layer of ECM that the cell produces. When cells detach from PIPAAm grafted surfaces when the temperature is lowered due to a reduction of affinity bonding between cell ECM and PIPAAm polymer chains [142]. This affinity is impacted by the ECM type created by cells and graft density and chain length of PIPAAm. Finding the optimal chain length and graft density is necessary to facilitate cell sheet release [144]. When grafting PIPAAm on to PDMS, there are temperature, oxidation, and irradiation constraints that impact whether graft density and polymer chain length is optimal for both cell attachment and release from its surface. Given these complications, we investigated grafting PIPAAm on to TCPS as an alternative for cell sheet release experiments.

Grafting PIPAAm onto TCPS is ideal as opposed to PDMS because oxidation and temperature are not constraints that need to be considered. This simplification in the grafting processes yielded positive results. We successfully cultured NIH 3T3 and C2C12 cells on PIPAAm-co-AM grafted onto TCPS (figure 4.8). When reducing the temperature to 20 °C, a sheet of NIH 3T3 cells released from the surface (figure 4.9). However, C2C12 cells were not successfully released from the surface (figure 4.10). This is likely due to the difference in bonding of cell ECM to PIPAAm-co-AM chains. NIH 3T3 cells are fibroblast cells that secrete collagen proteins used to

maintain the structure framework of many tissues. C2C12 cells are skeletal myoblasts which can differentiate into myotubes, a prerequisite to forming skeletal muscle tissue. *In vivo*, although fibroblasts make up a small portion of skeletal muscle tissue, they play an important role in maintaining muscle structure. Namely, through its secretion of collagen. This difference in cell role and function could explain why C2C12 cells do not release as well as NIH 3T3 cells. Future work can investigate co-culture methods of myoblast and fibroblast cell lines to improve cell sheet release of cells lines that do not produce ECM conducive to cells sheet release.

Given how well NIH 3T3 cells release from PIPAAm-co-AM surfaces at 20 °C, candidate cell lines for co-culture models such as endothelial and VSMC may release similarly. Endothelial cells and VSMC both contribute to ECM production in the healthy blood vessels [166]. Endothelial cells produce a laminin-rich membrane matrix that provides structural and organizational stability to blood vessels. VSMCs are the primary source of proteoglycans and other ECM components in arteries [167]. Both of these cell types would likely produce the ECM membrane necessary to facilitate cell sheet release, unlike that of observed of C2C12 cells.

Conclusion and Future Work

The goal of this study is to develop a novel co-culture model of aligned cell sheets for modular control of tissue thickness, cell orientation, and mechanical stimuli. Current results have shown successful grafting of NIPAAm onto PDMS. Wettability tests observing the contact angle of water on PIPAAm-grafted PDMS surfaces have exhibited hydrophilic and hydrophobic properties, respectively, at 20 °C and 40 °C. Characterization of surface roughness has shown a direct relationship between surface roughness and grafting time on PDMS. The surface roughness at 5 minutes and 10 minutes grafting time is low enough not to cover wavy topologies of patterned

PDMS. In addition, we have grafted PIPAAm-co-AM on to TCPS for cell sheet release experiments. We have successfully cultured NIH 3T3 and C2C12 cells on to PIPAAm-co-AM grafted TCPS dishes. We have successfully released a cell sheet of NIH 3T3 cells from PIPAAm grafted surfaces. Furthermore, we have developed a cell sheet manipulator device for the stacking of cell layers. Porcine hydrogel was successfully bound to the bottom of plunger device and is now capable of releasing stacks of cells as the hydrogel melts at 37 °C.

With the requisite work done in grafting PIPAAm-co-AM onto TCPS and the development of a cell sheet manipulator, future work to create Endothelial-VSMC co-culture model can be divided into 3 parts: (1) optimizing cell sheet stacking protocol, (2) endothelial-VSMC coculture optimization, and (3) design and implementation of the shear flow system (Figure 4.6). The first part includes seeding cells on fibronectin patterned PIPAAm-co-AM grafted TCPS to observe cell alignment and cell detachment from the surface. Afterwards, a cell sheet manipulator will be used to stack cell sheets on top of each other to fabricate thick 3D tissue. Second, cell sheet stacking experiments of endothelial-VSMC co-culture will be conducted. Work will include fixing stained cells to understand cell-cell interactions and imaging the changes in cell morphology due to co-culture. Before starting shear flow experiments, we will investigate the optimal culture conditions that promote cell viability. Lastly, a shear flow system will need to be developed and implemented to incur cell alignment. The fabrication of the shear flow system can be informed by microfluidic or machining techniques. In either system the constitutive parts will be a pump connected to a computer, a flow meter, a heater to warm culture media, and a chamber to house the endothelial-VSMC co-culture.

Future results, using the endothelial-VSMC co-culture system, investigates the phenotypic reaction of cells under hemodynamic conditions. We will observe how cells self-organize between cell layers. Monolayers of endothelial and VSMC cells, respectively, will reorientate parallel and orthogonally to the direction of shear flow. The implementation of endothelial cells sheet stacking onto VSMC should inhibit VSMC exposure to shear stress. Under these conditions, we will investigate whether VSMC will align perpendicular to the direction of shear flow or will reorientate along the same axis of endothelial cells. We will also investigate the optimal shear stress (dyn/cm^2) to incur cell alignment. Other investigations will involve understanding any differences in cell reorganization if cells are pre-aligned before cell stacking and if the co-culture is on patterned or flat surfaces.

Chapter 5 Conclusion

The following articles were published as a result of my PhD program (in chronological order):

- **S. Coyle**, S. Majidi, P. LeDuc, K.J. Hsia, "Bio-inspired soft robotics: Material selection, actuation, and design", *Extreme Mechanics Letters*. Vol 22 (2018), 51-59.
- U. Sonmez, **S. Coyle**, R. Taylor, P. LeDuc, "Polycarbonate Heat Molding for Soft Lithography", *Small*. Vol 16 (2020), Issue 16.
- **S. Coyle**, B. Doss, Y. Huo, H. Singh, D. Quinn, K.J. Hsia and P. Leduc, "Cell Alignment Modulated by Surface Nano-Topography – Roles of Cell-Matrix and Cell-Cell Interactions," *Acta Biomaterialia*, Vol 146 (2022), 149-159.

In addition, at the time of submission of this disseration, another manuscript is in preparation:

- P. Won*, **S. Coyle***, K.J. Hsia, D. Quinn, P. LeDuc, C. Majidi, "Muscular Liquid Metal Embedded Elastomer for Cyber Biohybrid System" (*these authors contributed equally to this work)

This thesis aims to leverage cell material interactions for better understanding of cell culture within 2D and 3D systems. The findings in this thesis contribute to the advancement of tissue engineering, biohybrid robotics, and co-culture models. In chapter 2, we investigated how cell confluency and cell-cell interactions impact cell alignment on different surface topographies. In chapter 3, we investigated methods to interface EGaIn with cell culture as well as methods to improve EGaIn biocompatibility by doping the material in known biocompatible materials. After optimizing the fabrication of a material that allows cells to interface with EGaIn, we leveraged EGaIn's electrical properties to create a biohybrid actuator. In chapter 4, we graft PIPAAm-co-AM onto TCPS to promote cell adhesion and detachment by a hydrophobic-to-hydrophilic transition triggered by temperature change. The purpose of the thermally bistable PIPAAm-co-AM was to initial cell sheet release that can be used to for co-culture models. We successfully

grafted NIH 3T3 and C2C12 cells on to PNIAM-co-AM grafted surfaces. We were able to release a monolayer of NIH 3T3 cells on PNIAM-co-AM at 20 °C. Based on the work presented in this thesis, the following conclusions are listed:

- Both cell confluency and cell-cell interactions impact cell alignment on different surface topographies. The effect of confluency and cell-cell interactions in facilitating cell alignment is impacted by the geometry of cell-matrix adhesion which cells are cultured on.

- Immunostaining of actin fiber and focal adhesion alignment between cells cultured on patterned verse flat PDMS helped illuminate the role of cell-matrix adhesion and cell alignment. On sinusoidal topographies, at low cell culture densities, there is a slight bias in actin fiber alignment along the direction of the grooves (λ = 0.56 µm). At high cell culture densities, the actin alignment along the groove direction was significantly enhanced. At both low and high culture densities cell alignment was enhanced on the longest wavelength substrate (λ = 2 µm).

- The use of anti-N-cadherin to perturb cell-cell interactions can inhibit cell polarization on surface geometries that have enhanced cell polarization only at higher cell densities. Anti-N-cadherin will not inhibit cell polarization on substrates that promote cell alignment regardless of cell density.

- The analysis of cell motility showed a direct correlation between preferential movement along the microgroove channels and polarity of actin filaments. It was found that cells cultured on surface topologies with shorter wavelengths (λ = 0.56 µm) not in the

presence of anti-N-cadherin exhibited greater preferential movement along the microgroove channels.

- Cells cannot be cultured directly onto liquid metal EGaIn. However, EGaIn can interface with C2C12 cells when embedded into biocompatible elastomers such as PDMS and ecoflex.

- We found there is a direct correlation between cell viability and liquid metal (LM) surface area when cells are cultured on a liquid metal embedded elastomer (LMEE) surface. The LM surface area decreases with the integration of EGaIn into precured polymers which is primarily facilitated by processing time.

- The maximum biocompatible volume ratio of eGaIn to PDMS that can be achieved is 70% EGaIn.

- A combination of different experimental studies suggest that an LMEE volume ratio of 60% in PDMS-LMEE composite materials may be ideal for many biohybrid applications as this volume ratio yields an optimal balance of material failure strain, electrical conductivity and biocompatibility.

- We successfully cultured myoblast (C2C12) and fibroblast (NIH 3T3) cells on to PNIAM-co-AM grafted surfaces. We were successful in releasing NIH 3T3 cells from PIPAAm grafted surfaces. We found that the cell type is important to facilitating cell sheet release from grafted surfaces.

- We successfully developed a cell plunger device that can be used for transferring and stacking cell sheets on top of each other.

References

[1] A. Albu-schaffer, O. Eiberger, M. Gerbenstein, S. Hassadin, C. Ott, T. Wimbock, S. Wolf and G. Hirzinger, "Soft Robotics," *IEEE Robtoics & Automation Magazine,* pp. 20-30, 2008.

[2] M. Manti, V. Cacucciolo and M. Cianchetti, "Stiffening in Soft Robotics," *IEEE Robotics & Automation Magazine,* pp. 93-106, 2016.

[3] S. Coyle, C. Majidi, P. R. LeDuc and K. J. Hsia, "Bio-inspired soft robotics: Material selection, actuation, and design," *Extreme Mechanics Letters,* vol. 22, pp. 51-59, 2018.

[4] C. Majidi, "Soft Robotics: A Perspective-Current Trends and Prospects for the Future," *Soft Robotics,* vol. 1, no. 1, pp. 5-11, 2014.

[5] L. Wang, S. G. Nurzaman and F. Iida, "Soft-Material Robotics," *Foundations and Trends in Tobotics,* vol. 5, no. 3, pp. 191-259, 2017.

[6] N. Elango and A. Faudzi, "A review article: investigations on soft materials for soft robot manipulations," *International Journal of Advanced Manufacturing Technology,* vol. 80, pp. 1027-1037, 2015.

[7] J. D. W. Madden, N. A. Vandesteeg, P. A. Anquetil, P. G. Madden, A. Takshi, R. Z. Pytel, S. R. Lafontaine, P. A. Wieringa and i. W. Hunter, "Artificial Muscle Technology: Physical Principles and Naval Prospects," *IEEE Journal of Oceanic Engineering,* vol. 29, no. 3, pp. 706-727, 2004.

[8] J. M. Nassar, J. P. Rojas, A. M. Hussain and M. M. Hussain, "From Stretchable to reconfigurable inorganic electronics," *Extreme Mechanics Letters,* vol. 9, pp. 245-268, 2016.

[9] J. C. Case, E. L. White and R. K. Kramer, "Soft Material Characterization for Robotic Applications," *Soft Robotics,* vol. 2, no. 2, pp. 80-87, 2015.

[10] A. O'Halloran, F. O'Malley and P. McHugh, "A review on dielectric elastomer actuators, technology, applications, and challenges," *Journal of Applied Physics,* vol. 104, no. 071101, 2008.

[11] M. T. Petralia and J. R. Wood, "Fabrication and Analysis of Dielectric-Elastomer Minimum-Energy Structures for Highly-Deformable Soft Robotic Systems," in *IEEE/RSJ International Conference on Intelligent Robots and Systems*, Taipei, Taiwan, 2010.

[12] M. T. Tolley, R. F. Shepard, B. Mosadegh, K. C. Galloway, M. Wehner, M. Karpelson, R. J. Wood and G. M. Whitesides, "A resilient, untethered soft robot," *Soft Robotics,* vol. 1, no. 3, pp. 213-223, 2014.

[13] H. Yuk, T. Zhang, G. A. Parada, X. Liu and X. Zhao, "Skin-inspired hydrogel–elastomer hybrids with robust interfaces and functional microstructures," *Nature Communications,* vol. 7, no. 12028, pp. 1-11, 2016.

[14] J.-Y. Sun, X. Zhao, W. Illeperuma, O. Chaudhuri, K. H. Oh, D. J. Mooney, J. J. Vlassak and Z. Suo, "Highly Stretchable and Tough Hydrogels," *Nature,* vol. 489, pp. 133-136, 2012.

[15] A. Miriyev, K. Stack and H. Lipson, "Soft material for soft actuators," *Nature Communications,* vol. 8, no. 1, p. 596, 2017.

[16] J. Huber, N. A. Fleck and M. F. Ashby, "The selection of mechanical actuators based on performance indices," *The Royal Society,* vol. 453, pp. 2185-2205, 1997.

[17] R. F. Shepherd, F. Illievski, W. Choi, S. A. Morin, A. A. Stokes, a. D. Mazzeo, X. Chen, M. Wang and G. M. Whitesides, "Multigait Soft Robot," *PNAS,* vol. 108, no. 51, pp. 20400-20403, 2011.

[18] B. Mosadegh, P. Polygerinos, C. Keplinger, S. Wennstedt, R. F. Shepherd, U. Gupta, J. Shim, K. bertoldi, C. Walsh and G. M. Whitesides, "Pneumatic Networks for Soft Robotics that Actuate Rapidly," *Advanced Functional Materials,* vol. 24, pp. 2163-2170, 2014.

[19] K. Suzumori, S. Iikura and H. Tanakaa, "Development of Flexible Microactuator and its Applications to Robotic Mechanisms," in *IEEE*, Sacramento, 1991.

[20] C. Laschi, M. Cianchetti, B. Mazzolai, L. Margheri, M. Follador and P. Dario, "Soft Robot Arm Inspired by the Octopus," *Advanced Robotics,* vol. 26, pp. 709-727, 2012.

[21] H.-T. Lin, G. G. Leisk and B. Trimmer, "GoQBot: A Caterpillar-Inspired Soft-Bodied Rolling Robot," *Bioinspiration & Biomimetics,* vol. 6, no. 026007, 2011.

[22] E. Epstein, J. Yoon, A. Madhukar, K. J. Hsia and P. V. Braun, "Colloidal Particles that Rapidly Change Shape via Elastic Instabilities," *Small,* 2015.

[23] M. Wehner, R. L. Truby, D. J. Fitzgerald, B. Mosadegh, G. M. Whitesides, J. A. Lewis and R. J. Wood, "An Integrated Design and Fabrication Strategy for Entirely Soft, Autonomous Robots," *Nature,* vol. 536, pp. 451-455, 2016.

[24] L. Wang, Y. Yang, Y. Chen, C. Majidi, F. Lida, E. Askounis and Q. Pei, "Controllable and reversible tuning of material rigidity for robotic applications," *Materials Today,* pp. 1-14, 2017.

[25] P. Egan, R. Sinko, P. R. LeDuc and S. Keten, "The Role of Mechanics in Biological and Bio-Inspired Systems," *Nature Communications,* vol. 6, no. 7418, pp. 1-11, 2015.

[26] N. G. Cheng, M. B. Lobovsky, S. J. Keating, A. M. Setapen, K. I. Gero, A. E. Hosoi and K. D. Iagnemma, "Design and Analysis of a Robust, Low-cost, Highly Articulated Manipulator Enabled by Jamming of Granular Media," in *Robotics and Automation (ICRA)*, Saint Paul, MN, USA, 2012.

[27] E. Brown, N. Rodenberg, J. Amend, A. Mozeika, E. Steltz, M. R. Zakin, H. Lipson and H. M. Jaeger, "Universal robotic gripper based on the jamming of granular material," *PNAS,* vol. 107, no. 44, pp. 11809-18814, 2010.

[28] E. Steltz, A. Mozeika, N. Rodenberg, N. Brown and H. M. Jaeger, "JSEL: Jamming Skin Enabled Locomotion," in *Intelligent Robots and Systems*, St. Louis, 2009.

[29] X. Li, "Strain induced semiconductor nanotubes: from formation process to device applications," *Journal of Physics D: Applied Physics,* vol. 41, no. 19, pp. 3001-30012, 2008.

[30] P. Froeter, X. Yu, W. Huang, F. Du, M. Li, I. Chun, S. H. Kim, K. J. Hsia, J. A. Rogers and X. Li, "3D hierarchical architectures based on self-rolled-up silicon nitride membranes," *Nanotechnology,* vol. 24, no. 47, pp. 1-9, 2013.

[31] V. Ramachandran, M. D. Bartlett , J. Wissman and C. Majidi, "Elastic instabilities of a ferroelastomer beam for soft reconfigurable electronics," *Extreme Mechanics Letters,* vol. 9, pp. 282-290, 2016.

[32] G. G. Stoney, "The Tension of Metallic Films Deposited by Electrolysis," *Proceedings of the Royal Society of London,* vol. 82, no. 553, pp. 172-175, 1909.

[33] M. Shahinpoor, Y. Bar-Coheen, J. O. Simpson and J. Smith, "Ionic Polymer-Metal Composites (IPMCs) as Biomimetic Sensors, Actuators, and Artifical Muscles- A Review," *Smart Materials and Structures,* vol. 7, no. 6, pp. R15-R30, 1998.

[34] L. Ricotti and A. Menciassi, "Bio-Hybrid Muscle Cell-Based Actuators," *Biomed Microdevices,* vol. 14, pp. 987-998, 2012.

[35] L. Ricotti, B. Trimmer, A. F. Feinberg, R. Raman, K. Parker, R. Bashir, M. Sitti, S. Martel, P. Dario and A. Menciassi, "Biohybrid actuators for robotics: A review of devices actuated by living cells," *Science Robotics,* vol. 2, pp. 1-17, 2017.

[36] R. W. Carlsen and M. Sitti, "Bio-Hybrid Cell-Based Actuators for Microsystems," *Small,* vol. 10, no. 19, pp. 3831-3851, 2014.

[37] L. Freund, "Substrate Curvature due to Thin Film Mismatch Strain in the nonlinear deformation Range," *Journal of the Mechanics and Physics of Solids,* vol. 48, pp. 1159-1174, 2000.

[38] I. S. Chun, A. Challa, B. Derickson, K. J. Hsia and X. Li, "Geometry Effect on the Strain-Induced Self-Rolling of Semiconductor Membranes," *Nano Letters,* vol. 10, pp. 3927-3932, 2010.

[39] M. J. Motala, D. Perlitz, C. M. Daly, P. Yuan, R. G. Nuzzo and K. J. Hsia, "Programming Matter Through Strain," *Extreme Mechanics Letters,* vol. 3, pp. 8-16, 2015.

[40] A. M. Abdullah, K. Nan, J. A. Rogers and K. J. Hsia, "Mismatch Strain Programmed Shape Transformation of Curved Bilayer-Flexible Support Assembly," *Extreme Mechanics Letters,* vol. 7, pp. 34-41, 2016.

[41] X. Yu, W. Huang, M. Li, T. M. Comberiate, S. Gong, J. E. Schult-Aine and X. Li, "Ultra-small, High-Frequency, and Substrate-Immune Microtube Inductors Transformed from 2D to 3D," *Scientific Reports,* vol. 5, p. 9661, 2015.

[42] T.-G. La and G.-K. Lau, "Very high dielectric strength for dielectric elastomer actuators in liquid dielectric immersion," *Applied Physics Letters,* vol. 102, no. 192905, 2013.

[43] F. Carpi, D. D. Rossi, R. Kornbluh, R. E. Pelrine and P. Sommer-Larsen, Dielectric Elastomers as Electromechanical Transducers: fundamentals, materials, devices, models and applications of an emerging electroactive polymer technology., Elsevier, 2011.

[44] A. W. Feinberg, A. Feigel, S. S. Shevkoplyas, S. Sheechy, G. M. Whitesides and K. K. Parker, "Muscular Thin Films for Building Actuators and Powering Devices," *Science,* vol. 317, pp. 1366-1370, 2007.

[45] F. A. Bayley, J. L. Liao, P. N. Stavrinou, A. Chiche and J. T. Cabral, "Wavefront kinetics of plasma oxidation of polydimethylsiloxane: limits for sub- μm wrinkling," *Soft Matter,* vol. 10, pp. 1155-1166, 2014.

[46] J. Kim, J. A. Hanna, M. Byun, C. D. Santangelo and R. C. Hayward, "Designing Responsive Buckled Surfaces by Halftone Gel Lithography," *Science,* vol. 335, pp. 1201-1205, 2012.

[47] A. Pandey, D. E. Moulton, D. Vella and D. P. Holmes, "Dynamics of snapping beams and jumping poppers," *Europhysics Letters,* vol. 105, no. 24001, 2014.

[48] Y. Forterre, J. M. Skotheim, J. Dumais and L. Mahadevan, "How the Venus flytrap snaps," *Nature,* vol. 433, pp. 421-425, 2005.

[49] N. P. Bende, A. A. Evans, S. Innes-Gold, L. A. Marin, I. Cohen, R. C. Hayward and C. D. Santangelo, "Geometrically Controlled snapping transitions in shells with curved creases," *PNAS,* vol. 112, no. 80, pp. 11175-11180, 2015.

[50] D. P. Holmes, B. Travakol, G. Froehlicher and H. A. Stone, "Control and manipulation of microfluidic flow via elastic deformations," *Soft Matter,* vol. 9, pp. 7049-7053, 2013.

[51] D. Trivedi, C. D. Rahn, W. M. Kier and I. D. Walker, "Soft robotics: Biological inspiration, state of the art, and future research Deepak," *Applied Bionics and Biomechanics,* vol. 5, no. 3, pp. 99-117, 2008.

[52] S. S. Robinson, K. W. O'Brien, H. Zhao, B. N. Peele, C. M. Larson, B. C. Murray, I. V. Meerbeek, S. N. Nunham and R. F. Shepard, "Integrated soft sensors and elastomeric actuators for tactile machines with kinesthetic sense," *Extreme Mechanics Letters,* vol. 5, pp. 47-53, 2015.

[53] C. Dagdeviren, P. Joe, O. Tuzman, K.-I. Park, K. J. Lee, Y. Shi, Y. Huang and J. A. Ragers, "Recent progress in flexible and stretchable piezoelectric devices for mechanical energy harvesting, sensing and actuation," *Extreme Mechanics,* vol. 9, pp. 269-281, 2016.

[54] A. Fassler and C. Majidi, "Liquid-Phase Metal Inclusions for a Conductive Polymer Composite," *Advanced Materials,* vol. 27, no. 11, pp. 1928-1932, 2015.

[55] J.-S. Noh, "Conductive Elastomers for Stretchable Electronics Sensors and Energy Harvesters," *Polymers,* vol. 8, no. 123, 2016.

[56] D.-H. Kim, N. Lu, R. Ma, Y.-S. Kim, R.-H. Kim, S. Wang, J. Wu, S. M. Won, H. Tao, A. Islam, K. J. Yu, T.-i. Kim, R. Chowdhury, M. Ying, L. Xu, M. Li, H.-J. Chung, H. Heum, M. McCormick, P. Liu, Y.-W. Zhang, F. G. Omenetto, Y. Huang, T. Coleman and J. A. Rogers, "Epidermal Electronics," *Science,* vol. 333, pp. 838-844, 2011.

[57] Kenry, J. C. Yeo and C. T. Lim, "Emerging flexible and wearable physical sensing platforms or healthcare and biomedical applications.," *Microsystems and Nanoengineering,* vol. 2, p. 16043, 2016.

[58] Y. Gutfreund, T. Flash, G. Fiorito and B. Hocher, "Patterns of Arm Muscle Activation Involved in Octopus Reaching Movements".

[59] H. Lipson, "Challenges and opportunities for design, simulation, and fabrication of soft robots," *Soft Robotics,* vol. 1, no. 1, pp. 21-27, 2013.

[60] R. Pfeifer, H. G. Marques and F. Iida, "Soft Robotics: The Next Generation of Intelligent Machines," *AAAi Press,* pp. 5-11, 2013.

[61] T. LI, K. Nakajima, M. Kuba, T. Gutnick, B. Hochner and R. Pfeifer, "From the Octopus to Soft Robots Control: An Octopus Inspired Behavior Control Architecture for Soft Robots," *Life and Environment,* 2011.

[62] Y. Gutfreund, T. Flash, Y. Yarom, G. Fiorito, I. Segev and B. Hochner, "Organization of Octopus Arm Movements: A Model System for Studying the Control of Flexible Arms," *The Journal of Neuroscience,* vol. 16, no. 22, pp. 7297-7307, 1996.

[63] S. V. Anand and T. A. Saif, "Emergent dynamics of cardiomyocyte clusters on deformable polymeric substrates," *Extreme Mechanics,* vol. 8, pp. 1-5, 2015.

[64] V. Chan, K. Park, M. B. Collens, H. Kong, T. A. Saif and R. Bashir, "Development of Miniaturized Walking Biological Machines," *Scientific Reports,* vol. 2, no. 857, pp. 1-8, 2012.

[65] T. H. Kim, C. H. Kwon, C. Lee, J. An, T. T. T. Phoung, S. H. Park, M. D. Lima, R. H. Baughman, T. M. Kang and S. J. Kim, "Bio-inspired Hybrid Carbon Nanotube Muscles," *Scientific Reports,* vol. 6, no. 26687, pp. 1-7, 2015.

[66] J. C. Nawroth, H. Lee, A. W. Feinberg, C. M. Ripplinger, M. McCain, A. Grosberg, J. O. Dabiri and K. K. Parker, "A tissue-engineered jellyfish with biomimetic propulsion," *Nature Biotechnology,* vol. 30, no. 8, pp. 792-797, 2012.

[67] B. J. Williams, S. V. Anand, J. Rajagopalan and M. T. Saif, "A self-propelled biohybrid swimmer at low Reynolds number," *Nature Communications,* vol. 5, no. 3081, pp. 1-8, 2013.

[68] H. Herr and R. G. Dennis, "A swimming robot actuated by living muscle tissue," *Journal of neuroengineering and rehabilitation,* vol. 1, no. 1, 2004.

[69] S.-J. Park, M. Gazzola , K. S. Park, S. Park, V. D. Santo, E. L. Blevins, J. U. Lind, P. H. Cambell, S. Dauth, A. K. Capulli and K. K. Parker, "Phototactic guidance of a tissue-engineered soft-robotic ray," *Science,* vol. 353, no. 6295, pp. 158-162, 2016.

[70] Y. Akiyama, T. Sakuma, K. Funakoshi, T. Hoshino, K. Iwabuchi and K. Morishima, "Atmospheric-operable bioactuator powered by insect muscle packaged with medium," *Lab on a Chip,* vol. 13, no. 24, pp. 4870-5880, 2013.

[71] K. Kuribayashi-Shigetomi, H. Onoe and S. Takeuchi, "Cell Origami: Self-Folding of Three-Dimensional Cell-Laden Microstructures Driven by Cell Traction Force," *PLOS ONE,* vol. 7, no. 12, 2012.

[72] A. W. Feinberg, A. Feigel, S. S. Shevkoplyas, S. Sheehy, G. M. Whitesides and K. K. Parker, "Muscular Thin Films for Building Actuators and Powering Devices," *Science,* vol. 317, pp. 1366-1370, 2007.

[73] S.-J. Park, K. K. Parker, M. Gazzola , S. Park, G. V. Lauder, B. M. Maoz, K. Deisseroth and A. Cho, "Phototactic Guidance of a Tissue-Engineered Soft-Robotic Ray," *Science,* vol. 353, no. 6295, 2016.

[74] Y. Morlmoto, H. Onoe and S. Takeuchi, "Biohybrid robot powered by an antagonistic pair of skeletal muscle tissues," *Science Robotics,* vol. 3, no. 18, 2018.

[75] K. Matsuura, R. Utoh, K. Nagase and T. Okano, "Cell sheet approach for tissue engineering and regenerative medicine," *Journal of Controlled Release,* pp. 228-236, 2014.

[76] X. Liu and P. X. Ma, "Polymeric Scaffolds for Bone Tissue Engineering," *Biomedical Engineering Society,* pp. 477-486, 2004.

[77] Y. Sawa, S. Miyagawa, T. Sakaguchi, T. Fuhita, A. Matsuyama, A. Saito, T. Shimizu and T. Okano, "Tissue engineered myoblast sheets improved cardiac function sufficiently to discontinue LVAS in a patient with DCM: report of a case," *Surg Today,* vol. 42, no. 2, pp. 181-184, 2012.

[78] N. G. Rim, A. Yih, P. Hsi, Y. Wang, Y. Zhang and J. Y. Wong, "Micropatterned cell sheets as structural building blocks for biomimetic vascular patches," *Biomaterials,* vol. 181, no. 126-139, 2018.

[79] S. Chien, "Mechanotransduction and endothelial cell homeostasis: the wisdom of the cell," *Heart and Circulaotry Physiology,* vol. 292, no. 3, 2007.

[80] M. N. Andalib, Y. Dzenis, H. J. Donahue and J. Y. Lim, "Biomimetic substrate control of cellular mechanotransduction," *Biomaterials Research,* vol. 20, no. 11, 2016.

[81] C.-M. Cheng, R. L. Steward Jr. and P. R. LeDuc, "Probing cell structure by controlling the mechanical environment with cell–substrate interactions," *Journal of Biomechanics,* pp. 187-192, 2009.

[82] R. L. Steward, C.-M. Cheng, D. L. Wang and P. R. LeDuc, "Probing Cell Structure Responses Through a Shear and Stretching Mechanical Stimulation Technique," *Cell Biochemistry and Biophysics,* vol. 56, pp. 115-124, 2010.

[83] C. He, M. Liu, D. Jiang, C. Qin, T. Liang, P. Wu, C. Han, L. Huang, K. J. Hsia and P. Wang, "Controlling Cellular Arrangements via Stretched Bioprinting," *bioRxiv,* 2020.

[84] A. L. Berrier and K. M. Yamada, "Cell–Matrix Adhesion," *Journal of Cellular Physiology,* vol. 213, pp. 565-573, 2007.

[85] J. Hu, C. Hardy, C.-M. Chen, S. Yang, A. S. Voloshin and Y. Liu, "Enhanced Cell Adhesion and Alignment on Micro-Wavy Patterned Surfaces Jia," *PLOS One,* 2014.

[86] M. Gupta, B. L. Doss, L. Kocgozlu, M. Pan, R.-M. Mège, A. Callan-Jones, R. Voituriez and B. Ladoux, "Cell shape and substrate stiffness drive actin-based cell polarity," *Physical Review,* vol. 99, no. 1, p. 012412, 2019.

[87] D. Joaquin, M. Grigola, G. Kwon, C. Blasius, Y. Han, D. Perlitz, J. Jiang, Y. Ziegler, A. Nardulli and K. J. Hsia, "Cell migration and organization in three-dimensional in vitro culture driven by stiffness gradient," *Biotechnology and Bioengineering,* vol. 113, no. 11, pp. 2496-2506, 11 2016.

[88] X. Jiang, S. Takayama, X. Qian, E. Ostuni, H. Wu , N. Bowden, P. LeDuc, D. E. Ingber and G. M. Whitesides, "Controlling Mammalian Cell Spreading and Cytoskeletal Arrangement with Conveniently Fabricated Continusous Wavy Features on Poly(dimethylsiloxane)," *American Chemical Society,* pp. 3273-3280, 2002.

[89] M. S. Grigola, C. L. Dyck, D. S. Babacan, D. N. Joaquin and K. J. Hsia, "Myoblast Alignment on 2D Wavy Patterns: Dependence on Feature Characteristics and Cell-Cell Interaction," *Biotechnology and Bioengineering,* pp. 1617-1626, 2014.

[90] M. A. Hill and G. A. Meininger, "Myogenic Tone and Mechanotransduction," *Muscle,* vol. 2, pp. 1243-1257, 2012.

[91] R. Janostiak, A. C. Paraki, J. Brabek and D. Rosel, "Mechanosensors in integrin signaling: The emerging role of p130Cas," *European Journal of Cell Biology,* vol. 93, no. 10-12, pp. 445-454, 2014.

[92] A. w. Orr, B. P. Helmke, B. R. Blackman and M. A. Schwartz, "Mechanisms of Mechanotransduction," *Developmental Cell,* vol. 10, no. 1, pp. 11-20, 2006.

[93] Y. Chen, L. Ju, M. Rushdi, C. Ge and C. Zhu, "Receptor-mediated cell mechanosensing," *Molecular Biology of the Cell,* vol. 28, no. 23, pp. 3134-3155, 2017.

[94] D. Mohammed, M. Versaevel, C. Bruyere, L. Alaimo, M. Luciano, E. Vercruysse, A. Proces and S. Gabriele, "Innovative Tools for Mechanobiology: Unraveling Outside-In and Inside-Out Mechanotransduction," *frontiers in Bioengineering and Biotechnology,* vol. 7, no. 162, 219.

[95] A. Cipitria and M. Salmeron-Sanchez, "Mechanotransduction and Growth Factor Signalling to Engineer Cellular Microenvironments," *Advanced Healthcare Materials,* vol. 6, no. 15, 2017.

[96] S. Yang, K. Khare and P. C. Lin, "Harnessing surface wrinkle patterns in soft matter," *Advanced Functional Materials,* vol. 20, no. 16, pp. 2550-2564, 2010.

[97] F. A. Bayley, J. L. Liao, P. N. Stavrinou, A. Chiche and J. T. Cabral, "Wavefront kinetics of plasma oxidation of polydimethylsiloxane: limits for sub-μm wrinkling," *Soft Matter,* vol. 10, no. 8, p. 1155, 2014.

[98] H. Hu, C. Huang, Xiao Hu Liu and K. J. Hsia, "Thin film wrinkling by strain mismatch on 3D surfaces," *Extreme Mechanics Letters,* pp. 107-113, 2016.

[99] E. Meijering, O. Dzyubachyk and I. Small, "Methods for Cell and Particle Tracking," *Methods in Enzymology,* pp. 183-200, 2012.

[100] N. Jaccard, L. D. Griffin, A. Kesar, R. J. Macown, A. Super, F. S. Versaitech and N. Szita, "Automated method for the rapid and precise estimation of adherent cell culture characteristics from phase contrast microscopy images," *Biotechnology and Bioengineering,* vol. 111, no. 3, pp. 504-517, 2014.

[101] P. A. Agudelo-Garcia, J. K. D. Jesus, S. P. Williams, M. O. Nowicki, E. A. Chiocca, S. Liyanarachchi, P.-K. Li, J. J. Lannutti, J. K. Johnson, S. E. Lawler and M. S. Viapiano, "Glioma Cell Migration on Three-dimensional Nanofiber Scaffolds Is Regulated by Substrate Topography and Abolished by Inhibition of STAT3 Signaling," *Neoplasia,* pp. 831-840, 2011.

[102] H. Wolfenson, B. Yang and M. P. Sheetz, "Steps in Mechanotransduction," *Annual Review of Physiology,* vol. 81, pp. 585-605, 2019.

[103] S. Charrasse, M. Meriane, F. Comunale, A. Blangy and C. Gauthier-Rouvière, "N-cadherin-dependent cell-cell contact regulates Rho GTPases and β-catenin localization in mouse C2C12 myoblasts," *Journal of Cell Biology,* vol. 158, no. 5, pp. 953-965, 2002.

[104] L. D. Derycke and M. E. Bracke, "N-cadherin in the spotlight of cell-cell adhesion, differentiation, embryogenesis, invasion and signalling," *The International Journal of Developmental Biology,* vol. 48, pp. 463-476, 2004.

[105] K. Tamura, W.-S. Shan, W. A. Hendrickson, D. R. Colman and L. Shapiro, "Structure-Function Analysis of Cell Adhesionby Neural (N-) Cadherin," *Neuron,* vol. 20, pp. 1153-1163, 1998.

[106] R. Vaz, G. G. Martins, S. Thorsteinsdottir and G. Rodrigues, "Fibronectin promotes migration, alignment and fusion in an in vitro myoblast cell model," *Cell and Tissue Research,* vol. 358, pp. 569-578, 2012.

[107] E. Clark and J. Brugge, "Integrins and signal transduction pathways: the road taken," *Science,* vol. 268, no. 5208, pp. 233-239, 1995.

[108] K. Huang, R. D. Kamm and R. T. Lee, "Cell mechanics and mechanotransduction: pathways, probes, and physiology," *American Physiological Society,* vol. 287, no. 1, pp. C1-C11, 2004.

[109] S. Johansson, G. Svineng, K. Wennerberg, A. Armulik and L. Lokikangas, "Fibronectin-Integrin Interactions," *Frontiers in Bioscience 2,* pp. 126-146, 1997.

[110] S. Lumetti, S. Mazzotta, S. Ferrillo, M. Piergianni, M. Piemontese, G. Passeri, G. M. Macaluso and C. Galli, "RhoA Controls Wnt Upregulation on Microstructured Titanium Surfaces," *BioMed Research International,* p. 9, 2014.

[111] K. J. Hsia, "Role of mechanics in biological materials research," *McGraw-Hill Education,* pp. 319-326, 2009.

[112] G. Giannone, B. J. Dublin-Thaler, O. Rossier, Y. Freund, G. Borisy and M. P. Sheetz, "Lamellipodial Actin Mechanically Links Myosin Activity with Adhesion-Site Formation," *Cell,* vol. 128, no. 3, pp. 561-575, 2007.

[113] A. D. Doyle and K. M. Yamada, "Mechanosensing via cell-matrix adhesions in 3D microenvironments," *Experimental Cell Research,* vol. 343, no. 1, pp. 60-66, 2016.

[114] M. J. Wheelock and K. R. Johnson, "Cadherin-mediated cellular signaling," *Current Opinion in Cell Biology,* vol. 15, pp. 509-514, 2003.

[115] J. Kucharczak, S. Charrasse, F. Comunale, J. Zappulla, B. Robert, I. Teulon-Navarro, A. Pelegrin and C. Gauthier-Rouviere, "R-Cadherin Expression Inhibits Myogenesis and Induces Myoblast Transformation via Rac1 GTPase," *Cancer Research,* vol. 68, no. 16, pp. 6559-6568, 2008.

[116] M. Ozawa, "E-cadherin cytoplasmic domain inhibits cell surface localization of endogenous cadherins and fusion of C2C12 myoblasts," *The Company of Biologists,* vol. 4, pp. 1427-1435, 2015.

[117] H. Takano, I. Komuro, T. Oka, I. Shiojima, Y. Hiroi, T. Mizuno and Y. Yazaki, "The Rho Family G Proteins Play a Critical Role in Muscle Differentiation," *Molecular and Cellular Biology,* vol. 18, no. 3, pp. 1580-1589, 1998.

[118] F. Comunale, M. Causeret, C. Fravard, J. Cau, N. Taulet, S. Charrasse and C. Gauthier-Rouviere, "Rac1 and RhoA GTPases have antagonistic functions during N-cadherin-dependent cell–cell contact formation in C2C12 myoblasts," *Biology of the Cell,* pp. 503-517, 2007.

[119] L. Becciolini, E. Meacci, C. Donati, F. Cencetti, E. Rapizzi and P. Bruni, "Sphingosine 1-phosphate inhibits cell migration in C2C12 myoblasts," *Biochimica et Biophysica Acta 1761,* pp. 43-51, 2006.

[120] K. Tanaka, K. Sato, T. Yoshida, T. Fukuda, K. Hanamura, N. Kojima, T. Shirao, T. Yanagawa and H. Watanabe, "Evidence for cell density affecting C2C12 myogenesis: possible regulation of myogenesis by cell-cell communication," *Muscle Nerve,* vol. 44, no. 6, pp. 968-977, 2011.

[121] I. Grabowska, A. Sxeliga, J. Maraczewski, I. Czaplicka and E. Brzoska, "Comparison of satellite cell-derived myoblasts and C2C12 differentiation in two- and three-dimensional cultures: changes in adhesion protein expression," *Cell Biology International,* vol. 35, pp. 125-133, 2011.

[122] L. Sun, Y. Yu, Z. Chen, F. Bian, F. Ye, L. Sun and Z. Yuanjin, "Biohybrid robotics with living cell actuation," *Royal Society of Chemistry,* vol. 49, pp. 4043-4069, 2020.

[123] F. Xu, T. Beyazoglu, E. Hefner, U. A. Gurkan and U. Demirci, "Automated and Adaptable Quantification of Cellular Alignment from Microscopic Images for Tissue Engineering Applications," *Tissue Engineering: Part C,* vol. 17, no. 6, pp. 641-649, 2011.

[124] R. W. Carlsen and M. Sitti, "Bio-Hybrid Cell-Based Actuators for Microsystems," *Small,* vol. 10, no. 19, pp. 3821-3851, 2014.

[125] M. D. Dickey, R. C. Chiechi, R. J. Larsen, E. A. Weiss, D. A. Weitz and G. M. Whitsides, "Eutectic Gallium-Indium (EGaIn): A Liquid Metal Alloy forthe Formation of Stable Structures in Microchannelsat Room Temperature," *Advanced Funtional Materials,* vol. 18, pp. 1097-1104, 2008.

[126] J.-H. Kim, S. Kim, J.-H. So, K. Kim and H.-J. Koo, "Cytotoxicity of Gallium−Indium Liquid Metal in an Aqueous," *Applied Materials & Interfaces,* vol. 10, pp. 17448-17454, 2018.

[127] C. Pan, D. Liu, M. J. Ford and C. Majidi, "Ultrastretchable, Wearable Triboelectric Nanogenerator Based on Sedimented Liquid Metal Elastomer Composite," *Advanced Materials Technologies,* vol. 5, no. 11, 2020.

[128] D. Sharma, D. Ross, G. Wang, W. Jia, S. J. Kirkpatrick and F. Zhao, "Upgrading prevascularization in tissue engineering: A review of strategies for promoting highly organized microvascular network formation," *Acta Biomaterialia,* vol. 95, pp. 112-130, 2019.

[129] R. Jennings and C. Premanandan, Veterinary Histology, Ohio State University Libraries, 2017.

[130] S. D. Francescomarino, A. Sciartilli , V. D. Valerio, A. D. Baldassarre and S. Gallina, "The Effect of Physical Exercise on Endothelial Function," *Sports Medicine,* vol. 39, pp. 797-812, 2009.

[131] O. Traub and B. C. Berk, "Mechanisms by Which Endothelial Cells Transduce an Atheroprotective Force," *Arteriosclerosis, Thrombosis, and Vascular Biology,* vol. 18, no. 5, pp. 677-685, 1998.

[132] B. Lilly, "We Have Contact: Endothelial Cell-Smooth Muscle Cell Interactions Blood," *PHYSIOLOGY,* vol. 29, pp. 234-241, 2014.

[133] M. Li, M. Qian, K. Kyler and J. Xu, "Endothelial–Vascular Smooth Muscle Cells Interactions in Atherosclerosis," *frontiers in Cardiovascular Medicine,* vol. 5, 2018.

[134] D. Shav, R. Gotlieb, U. Zaretsky, D. Elad and S. Einav, "Wall Shear Stress Effects on Endothelial-Endothelial and Endothelial-Smooth Muscle Cell Interactions in Tissue Engineered Models of the Vascular Wall," *PLOS ONE,* vol. 9, no. 2, p. 88304, 2014.

[135] N. C. A. v. Engeland, A. M. Pollet, J. M. d. Toonder, C. V. Bouten, O. M. Stassen and C. M. Sahlgren, "A biomimetic microfluidic model to study signalling between endothelial and vascular smooth muscle cells under hemodynamic conditions," *Lab on a Chip,* vol. 18, no. 11, pp. 1607-1620, 2018.

[136] X. Han, N. Sakamoto, N. Tomita, H. Meng, M. Sato and M. Ohta, "Influence of TGF-b1 expression in endothelial cells on smooth muscle cell phenotypes and MMP production

under shear stress in a co-culture model," *Cytotechnology,* vol. 71, no. 2, pp. 489-496, 2019.

[137] C.-N. Chen, S.-F. Chang, P.-L. Lee, K. Chang, L.-J. Chen, S. Usami, S. Chien and J.-J. Chiu, "Neutrophils, lymphocytes, and monocytes exhibit diverse behaviors in transendothelial and subendothelial migrations under coculture with smooth muscle cells in disturbed flow," *Blood,* vol. 107, no. 5, pp. 1933-1942, 2006.

[138] J. Sakai, T. Karino and K. Niwa, "Flow-dependent accumulation of LDL in co-cultures of endothelial and smooth muscle cells in the presence of filtration flow through the cell layer," *Clinical Hemorheology and Microcirculation,* vol. 38, no. 4, pp. 245-56, 2008.

[139] Z. Ding, Y. Fan and X. Deng, "Water filtration rate and infiltration/accumulation of low density lipoproteins in 3 different modes of endothelial/smooth muscle cell co-cultures," *Science in China Series C: Life Sciences,* vol. 52, pp. 1023-1029, 2009.

[140] J. S. Choi and T. S. Seo, "Orthogonal co-cultivation of smooth muscle cell and endothelial cell layers to construct in vivo-like vasculature," *Biomicrofluidics,* vol. 13, p. 014115, 2019.

[141] L. A. Martinez-Lemus, "The Dynamic Structure of Arterioles," *Basic & Clinical Pharmacology & Toxicology,* vol. 110, pp. 5-11, 2011.

[142] J. Kobayashi, A. Kikuchi, T. Aoyagi and T. Okano, "Cell sheet tissue engineering: Cell sheet preparation, harvesting/manipulation, and transplantation," *Journal of Biomedical Materials Research ,* vol. 107, no. 5, pp. 955-967, 2019.

[143] H. Takahashi and T. Okano, "Cell Sheet-Based Tissue Engineering for Organizing Anisotropic Tissue Constructs Produced Using Microfabricated Thermoresponsive Substrates," *Advanced Healthcare Materials,* vol. 4, no. 13, pp. 2388-2407, 2015.

[144] H. Takahashi, T. Shimizu and T. Okano, "Intelligent Surfaces for Cell Sheet Engineering," *Principles of Regenerative Medicine,* pp. 469-484, 2019.

[145] K. Duval, H. Grover, L.-H. han, Y. Mou, A. F. Pegoraro, J. Fredburg and Z. Chen, "Modeling Physiological Events in 2D vs. 3D Cell Culture," *Physiology,* vol. 32, no. 4, pp. 266-277, 2017.

[146] K. Kim, S. Bou-Ghannam and T. Okano, "Cell sheet tissue engineering for scaffold- free three-dimensional (3D) tissue reconstruction," *Methods in Cell Biology,* Vols. 143-167, p. 157, 2020.

[147] Y. Akiyama, M. Matsuyama, M. Yamato, N. Takeda and T. Okano, "Poly(N-isopropylacrylamide)-Grafted Polydimethylsiloxane Substrate for Controlling Cell Adhesion and Detachment by Dual Stimulation of Temperature and Mechanical Stress," *Biomacromolecules,* vol. 19, pp. 4014-4022, 2018.

[148] H. Takahashi, T. Shimizu, M. Nakayama, M. Yamato and T. Okano, "The use of anisotropic cell sheets to control orientation during the self-organization of 3D muscle tissue," *Biomaterials,* vol. 34, no. 30, pp. 7372-7380, 2013.

[149] Y. Akiyama and O. T. , "Temperature-responsive polymers for cell culture and tissue engineering applications," in *Switchable and Responsive Surfaces and Materials for Biomedical Applications*, Elsevier, 2015, pp. 203-233.

[150] H. Takahashi and T. Okano, "Thermally-triggered fabrication of cell sheets for tissue engineering and regenerative medicine," *Advanced Drug Delivery Reviews,* vol. 138, pp. 276-292, 2019.

[151] T. Sasagawa, T. Shimizu, S. Sekiya, Y. Haraguchi, M. Yamato, Y. Sawa and T. Okano, "Design of prevascularized three-dimensional cell-dense tissues using a cell sheet stacking manipulation technology," *Biomaterials,* vol. 31, no. 7, pp. 1646-1654, 2010.

[152] J. B. Lin, B. C. isenberg, Y. Shen, K. Schorsch, O. V. Sazonova and J. Y. Wong, "Thermo-responsive poly(N-isopropylacrylamide) grafted onto microtextured poly(dimethylsiloxane) for aligned cell sheet engineering," *Colloids and Surfaces B: Biointerfaces,* vol. 99, pp. 108-115, 2012.

[153] S. Sugiura, W. Imano, T. Takagi, K. Sakai and T. Kanamori, "Thermoresponsive protein adsorption of poly(N-isopropylacrylamide)-modified streptavidin on polydimethylsiloxane microchannel surfaces," *Biosenors and Bioelectronics,* vol. 24, no. 5, pp. 1135-1140, 2009.

[154] M. Ebara, J. M. Hoffman, P. S. Stayton and A. S. Hoffman, "Surface modification of microfluidic channels by UV-mediated graft polymerization of non-fouling and 'smart' polymers," *Science Direct,* vol. 76, no. 8-9, pp. 1409-1413, 2007.

[155] X. S. Wu, A. S. Hoffman and P. Yager, "Synthesis and Characterization of Thermally Reversible Macroporous Hyrdogels," *Journal of Polymer Science Part A ,* pp. 2121-2129, 1992.

[156] P. Sakulaue, A. Y. Y. Swe, K. Benchaprathanphorn, T. Lertvanithphol, K. Viravaidya-Pasuwat and W. Siriwatwechakul, "Improving Cell Detachment from Temperature-Responsive Poly(N-isopropylacrylamide-co-acrylamide)-Grafted Culture Surfaces by Spin Coating," *ACS Omega,* vol. 3, pp. 18181-18188, 2018.

[157] P. Sakulaue, T. Lertvanithphol, P. Eiamchai and W. Siriwatwechakul, "Quantitative relation between thickness and grafting density of temperature-responsive poly(N-isopropylacrylamide-co- acrylamide) thin film using synchrotron-source ATR-FTIR and spectroscopic ellipsometry," *Surface and Interface Analysis,* vol. 53, pp. 268-276, 2021.

[158] K. Nagase, M. Yamato, H. Kanazawa and T. Okano, "Poly(N-isopropylacrylamide)-based thermoresponsive surfaces provide new types of biomedical applications," *Biomaterials,* vol. 153, pp. 27-48, 2018.

[159] B. C. Isenberg, Y. Tsuda, C. Williams, T. Shimizu, M. Yamato, T. Okano and J. Y. Wong, "A thermoresponsive, microtextured substrate for cell sheet engineering with defined structural organization," *Biomaterials,* vol. 29, pp. 2565-2572, 2008.

[160] N. Matsuzaka, M. Nakayama , H. Takahashi, M. Yamato, A. Kikuchi and T. Okano, "Terminal-Functionality Effect of Poly(N-isopropylacrylamide) Brush Surfaces on Temperature-Controlled Cell Adhesion/Detachment Naoki," *Biomacromolecules,* vol. 14, no. 9, pp. 3164-3171, 2013.

[161] S. Coyle, B. Doss, Y. Huo, H. Singh, D. Quinn, P. Leduc and K. J. Hsia, "Cell Alignment Modulated by Surface Nano-Topography – Roles of Cell-Matrix and Cell-Cell Interactions," *Acta Biomaterialia,* vol. 142, pp. 149-159, 2022.

[162] Y. Sun, R. Duffy, A. Lee and A. W. Feinberg, "Optimizing the structure and contractility of engineered skeletal muscle thin films," *Acta Biomaterialia,* vol. 9, pp. 7885-7894, 2013.

[163] C. Williams, Y. Tsuda, B. C. Isenberg, M. Yamato, T. Shimizu, T. Okano and J. Y. Wong, "Aligned Cell Sheets Grown on Thermo-Responsive Substrates with Microcontact Printed Protein Patterns," *Advanced Materials,* vol. 21, no. 21, pp. 2161-2164, 2009.

[164] K. Nagase, M. Yamato, H. Kanazawa and T. Okano, "Poly(N-isopropylacrylamide)-based thermoresponsive surfaces provide new types of biomedical applications," *Biomaterials,* vol. 153, pp. 27-48, 2018.

[165] P. Juffer, A. D. Bakker, J. Klein-Nulend and R. T. Jaspers, "Mechanical Loading by Fluid Shear Stress of Myotube Glycocalyx Stimulates Growth Factor Expression and Nitric Oxide Production," *Cell Biochemistry and Biophysics ,* vol. 69, pp. 411-419, 2014.

[166] A. C. Doran, N. Meller and C. A. McHamara, "The Role of Smooth Muscle Cells in the Initiation and Early Progression of Atherosclerosis," *Doran, Amanda C et al. "Role of smooth muscle cells in the initiation anArteriosclerosis, thrombosis, and vascular biology,* vol. 28, no. 5, pp. 812-819, 2008.

[167] S. Allahverdian, C. Ortega and G. A. Francis, "Smooth Muscle Cell-Proteoglycan-Lipoprotein Interactions as Drivers of Atherosclerosis," *Prevention and Treatment of Atherosclerosis,* vol. 270, pp. 335-358, 2020.

[168] H. H. W. a. F. Chambon, "Analysis of Linear Viscoelasticity of a Crosslinking Polymer at the Gel Poin," *Journal of Rheology,* vol. 30, no. 367, pp. 367-382, 1986.

[169] S. Nicolle, M. Lounis, R. Willinger and J. Palierne, "Shear linear behavior of brain tissue over a large frequency range," *Biorheology,* vol. 42, pp. 209-223, 2005.

[170] M. McGarry, C. L. Johnson, B. P. Sutton, E. E. W. Houten, J. G. Georgiadis, J. B. Weaver and K. D. Paulsen, "Including Spatial Information in Nonlinear Inversion MR Elastography Using Soft Prior Regularization," *IEEE TRANSACTIONS ON MEDICAL IMAGING,* vol. 32, no. 10, pp. 1901-1909, 2013.

[171] S. E. Premalatha, R. Chockkalingam and M. Mahendran, "Magneto Mechanical Properties of Iron Based MR Fluids," *American Journal of Polymer Science,* vol. 2, no. 4, pp. 50-55, 20112.

[172] L. Yanju, D. Hejun and W. Dianfu, "ER fluid based on inorganic/polymer blend particles and its adaptive viscoelastic properties," *Colloids and Surfaces A: Physicochemical and Engineering Aspects,* vol. 189, pp. 203-210, 2001.

[173] M. A. Green, R. Sinkus, S. C. Gandevia, R. D. Herbert and L. E. Bilston, "Measuring changes in muscle stiffness after eccentric exercise using elastography," *NMR Biomedicine,* vol. 25, pp. 852-858, 2012.

[174] E. Barnhill, P. Kennedy, S. Hammer, E. J. R. Been, C. Brown and N. Roberts, "Statistical mapping of the effect of knee extension on thigh muscle viscoelastic properties using magnetic resonance elastography," *PHYSIOLOGICAL MEASUREMENT,* vol. 34, pp. 1675-1698, 2013.

[175] J. L. Nelissen, L. d. Graaf, W. A. Traa, T. J. L. Schreurs, K. M. Moerman, A. J. Nederveen, R. Sinkus, C. W. J. Oomens, K. Nicolay and G. J. Strijkers, "A MRI-Compatible Combined Mechanical Loading and MR Elastography Setup to Study Deformation-Induced Skeletal Muscle Damage in Rats," *PLOS: one,* vol. 10, no. 1371, pp. 1-22, 2017.

[176] M. Geerligs, G. W. Peters, P. A. Ackermans, C. W. Oomens and F. P. Baaijens, "Linear viscoelastic behavior of subcutaneous adipose tissue," *Biorheology,* vol. 45, pp. 677-688, 2008.

[177] B. Yang, Z. Yaling, X. Zhang, L. Tao, S. Li and Y. Wei, "Facilely prepared inexpensive and biocompatible self-healing hydrogel: a new injectable cell therapy carrier," *Polymer Chemistry,* vol. 3, pp. 3235-3238, 2012.

[178] S. Rammensee, D. Huemmerich, T. Scheibel and A. R. Bausch, "Rheological characterization of hydrogels formed by recombinantly produced spider silk," *Applied Physics A: Materials Science & Processing,* vol. 82, no. 261, 2005.

[179] Y.-F. Tang, Y.-M. Du, X.-W. Hu, S. Xiao-Wen and J. F. Kennedy, "Rheological characterization of a novel thermosensitive chitosan/poly(vinyl alcohol) blend hydrogel," *Carbohydrate Polymers,* vol. 67, pp. 491-499, 2007.

[180] j. Jiang, W. Su, P. T. Mather and T. J. Bunning, "Rheology of highly swollen chitosan/polyacylate hydrogels," *Polymer,* vol. 40, no. 16, pp. 4593-4602, 1999.

[181] S. Niamlang, S. Thongchai, N. Pawananant and A. Sirivat, "The electromechanical properties of crosslinked natural rubber," *Energy Procedia,* vol. 34, pp. 697-704, 2013.

[182] X. Yuan, S. Changgeng, G. Yan and Z. Zhenghong, "Application review of dielectric electroactive polymers (DEAPs) and piezoelectric materials for vibration energy harvesting," *Journal of Physics: Conference Series,* vol. 744, no. 012077, 2016.

Appendix A

Polydimethylsiloxane (PDMS)	[168]	Brain Tissue	[169, 170]	MR Fluids	[171]
ER Fluid based polymers	[172]	Muscle Tissue	[173, 174, 175]	Porcine Fat	[176]
DF-PEG Hydrogels	[177]	Spider Silk Hydrogel	[178]	Chitosan/ polyvinyl hydrogel	[179]
Polyacrylate Hydrogel	[180]	Natural Rubber	[181]		

Table 3 Sources of material properties in Figure 1.1

Appendix B

DEA (VHB)	[7]	Pneumatic	[16]	Ferromagnetic Polymers	[7]
DEA (Silicon)	[7, 182]	Muscle	[7]	Piezoelectric Polymer	[16, 182]
SMA	[7, 16]	IPMC	[7]	Hydraulic	[16]

Table 4 Sources of material properties in Figure 1.2

Stephen Coyle is a PhD candidate co-advised by Prof. Phil LeDuc, Prof. K. Jimmy Hsia, and Dr. David Quinn. His research interests involve studying the mechanics of muscle cell-laden microstructures for applications in biohybrid systems and tissue engineering. He received his B.S. degree in Applied Mathematics from Claflin University and his M.S. degree in Mechanical Engineering from Carnegie Mellon University. He will be working at ZS Associates in Boston, MA after the completion of his PhD program.